UCL Université catholique de Louvain

École polytechnique de Louvain (EPL)

Design and experimental investigation with particle image velocimetry of a minimum induced drag wing.

Dissertation presented by
Jonathan TOUSSAINT

for obtaining the Master's degree in
Mechanical Engineering

Supervisor(s)
Grégoire WINCKELMANS

Reader(s)
Philippe CHATELAIN, Jean-François REMACLE

Academic year 2016-2017

Acknowledgements

This Masters' thesis symbolises the fulfilment of my academic path at the Louvain School of engineering. This achievement would not have been possible without the help of many people, who encouraged and supported me both morally and intellectually.

In the first place, I would like to express my gratitude to Pr. Grégoire Winckelmans for his confidence in my work, but also Denis-Gabriel Caprace, for his kindness and the generosity of his help throughout the whole year.

A huge gratitude to the team of the TFL laboratory : Franck Hesbois, Julien Vervotte and Yan Liu for the help they provided me during the experimental campaign. All the results exposed in this thesis would not exist without them.

Then, I would like to thank Penny, Jean-Jacques and Steven for the time they spent during their holidays to reread this document.

Thanks also to Isabelle Hennau for her benevolence and to Laurent Paul and 3D Side for their amiability and help to manufacture the wing.

Last but not least, I would like to hugely thank all my close friends and my family for their endless support.

Finally, thank you Sophie for supporting me every day during those studies.

Jonathan
August 2017

Table of contents

Nomenclature

A_R	Aspect ratio	$[-]$
A_0	Lift slope of the wing	$[-]$
AKE	Average kinetic energy	$[m^2/s^2]$
a_0	Lift slope of the profile	$[-]$
b	Span	$[m]$
b_0	Spacing between rolled-up trailing vortices	$[m]$
c	Chord	$[m]$
$\overline{c}$	Mean chord	$[m]$
C_L	Lift coefficient	$[-]$
$C_{L_{design}}$	Lift coefficient of design	$[-]$
C_D	Drag coefficient	$[-]$
C_{D_i}	Induced drag coefficient	$[-]$
C_{D_0}	Zero lift drag coefficient of the wing	$[-]$
C_d	Drag coefficient of the profile	$[-]$
D	Drag force	$[N]$
D_i	Induced drag force	$[N]$
dt	Interval of time between two frames capture	$[\mu s]$
e	Oswald's efficiency	$[-]$
f_{max}	Maximum lift/drag ratio	$[-]$
g	Gravitational acceleration	$[m/s^2]$
k	Constant relative to the induced drag coefficient	$[-]$
L	Lift force	$[N]$
l	Lift force of the profile	$[N]$
M	Bending moment	$[Nm]$
P_{dyn}	Dynamic pressure	$[Pa]$
P_0	Ambient pressure	$[Pa]$
Q	Bending moment on the whole wing	$[Nm]$
r	Radius of gyration	$[m]$
Re_r	Reynolds number based on the wingroot	$[-]$
S	Wing area	$[m^2]$

TKE	Turbulent kinetic energy	$[m^2/s^2]$
U_∞	Upstream velocity	$[m/s]$
u, v, w	Velocities components in the three directions	$[m/s]$
x, y, z	Cartesian coordinates	$[-]$
α	Geometric angle of attack	$[deg]$
α_e	Effective angle of attack	$[deg]$
α_v	Twist angle	$[deg]$
β	Constant relative to the induced drag coefficient of the profile	$[-]$
ϵ	Downwash angle	$[deg]$
ρ	Air density	$[kg/m^3]$
Γ	Circulation	$[m^2/s]$
λ	Taper ratio	$[-]$
τ	Non-dimensional time	$[-]$

Introduction

Abstract

In order to fly, an aircraft of a given weight needs to produce an equal but opposite force to this weight: the lift. This lift generation comes along with a drag creation, which can be decomposed in two parts : the profile drag and the induced drag.
The first one can be characterised by the skin drag, directly resulting from the friction between the air and the surfaces of the wing, and the form drag, which is dependent on the geometry of the airfoil.
The induced drag, however, is imputed to the lift creation. In fact, when flying, an aircraft leaves behind itself a pair of counter-rotating vortices, which are intrinsically linked to the induced drag, as we will see later on in this document.

Figure 0.1: Trailing vortices visualisation. *Source : www.airliners.net*

In order to compute those general aerodynamic characteristics, Ludwig Prandtl published in 1922 a model famously known as the "Lifting line theory" [1]. Resulting from this theory, the wing which offered the best performances (the minimum ratio of lift per drag production) had an elliptical spanload. This quickly became the reference in the design of wings but, in 1933 [2], Prandtl himself stated that his former theory was incomplete.
In fact, this concept only took the performances of the wing into consideration, but did not refer to its structural mass.
Prandtl therefore published a (strangely still delittle known) note where he explained that the best new spanload was *bell-shaped*. In addition to the structural mass consideration, this type of wing was likely to offer better performances than the elliptical wing. In fact, for a span 22 percent larger than the elliptical one, this wing would produce 11 percent less induced drag. This is a major statement that NASA wanted to investigate back in 2015, by creating a so called *Prandtl-D Aircraft* [3], designed on the Prandtl's theory.

The purpose of this Masters' thesis was, like NASA did, to design, manufacture and test our own *bell-shaped* wing in order to investigate the expected aerodynamic characteristics presented here above.

Motivation

All the theoretical and mathematical aspects evoked here above rise from a specific biological context... In fact, nature has always been far ahead of humans, and this is unquestionably true

for bird flights.
Everyday, we see birds flying, but we rarely pay attention to the way they do it. In fact, one can easily notice that few birds have vertical tail as the modern airplanes have, and they are nevertheless capable of doing sharp maneuvres, while commercial airplanes' moves are very limited. Also, some birds tend to fly in formation with their wingtips overlapped, while few actual -civilian- planes achieve that.

Figure 0.2: Birds formation flight with wingtips overlapped

Furthermore, the tips of birds' wings are narrow and flexible, incapable of supporting any substantial load, whereas wingtips of modern airplanes are heavy, large and manufactured to support real loads in flight.
Besides the scientific work achieved in that thesis, the understanding of how nature achieve things that human cannot is extraordinarily exciting and interesting.

Thesis outline

The first chapter is dedicated to the theoretical tools needed to understand and analyse the experimental results.
In the first time, some fundamentals about aerodynamics are presented. Secondly, the *Lifting line theory* is presented, followed by the special Prandtl's theory, which is the basement of this thesis. The notable differences between the elliptic and *bell-shaped* wings are there exposed.

The second section concerns all the experimental setup.
Firstly, the design and manufacturing of our *bell-shaped* wing is detailed, going from pure theoretical aspects to mechanical features. Then, the experimental equipment used to test this wing is listed and explained : the wind tunnel, the aerodyanmic balance and the PIV (*Particle Image Velocimetry*) equipment.

Finally, the third and biggest chapter is all about the analysis of obtained results.
First, the general aerodynamic characteristics are presented, followed by the PIV results and the different way to exploit them.

1 Theory

In this section, we will cover all the theory aspects needed to understand how such a "Prandtl wing" works. We will first begin with the two-dimensional concepts, moving further to the tri-dimensional world, where many more considerations have to be taken into account to understand the behaviour of a finite span wing, with the famous Prandtl's lifting line theory [4]. Finally, we will have a look at the special Prandtl's theory [2] which leads to the design of our Prandtl wing, and explains how such a wing has better performances than the elliptic wing (thus far known as the "perfect" wing).

1.1 Infinite span wing

Before exposing further theories, let us recall some fundamentals about aerodynamics [5].

In an inviscid and irrotational flow (no skin friction nor flow separation), an object moving at velocity U_∞ undergoes a force perpendicular to the flow. This force is proportional to the circulation Γ around the object, which is defined as (we will bear this in mind for later on):

$$\Gamma \equiv -\oint_C \vec{V} \cdot \vec{dl} \ , \tag{1.1}$$

$$\Gamma \equiv -\int_A \vec{\omega} \cdot \vec{dA} \ . \tag{1.2}$$

In the case of a thin airfoil, this force is called *lift* and is defined (per unit length) as:

$$l = \rho \, U_\infty \, \Gamma \ . \tag{1.3}$$

Equation (1.3) is well known as the Kutta-Joukowski theorem.
Also, as the airfoil evolves in an inviscid and irrotational flow, it is not subject to drag.

Let us now introduce the concept of vortex sheet.
A vortex sheet is an assembling of an infinite number of vortex lines (also called vortex filaments). Its strength, per unit length along a direction s, is defined perpendicularly to this direction by:

$$\underline{\gamma} = \gamma \underline{\hat{t}} = \gamma(s) \underline{\hat{t}} \ .$$

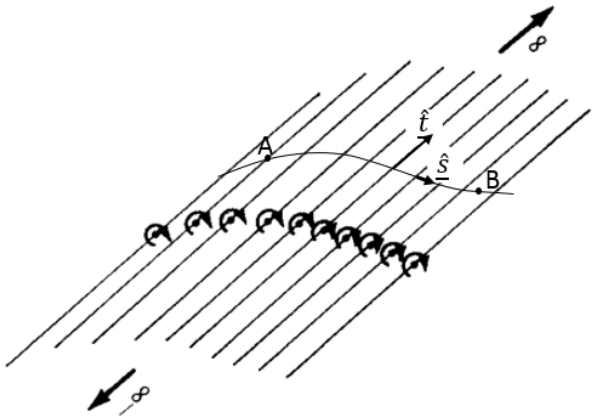

Figure 1.1: Sketch of a vortex sheet. *Source : Fundamentals of aerodynamics, J.D. Anderson [5]*

Also, the circulation of the above vortex sheet from a point A to a point B is given as:

$$\Gamma = \int_A^B \gamma(s)\, ds \ . \tag{1.4}$$

Therefore,

$$\gamma(s) = \frac{d\Gamma}{ds}(s) \tag{1.5}$$

is the circulation per unit length of the shed vortex sheet.

1.2 Finite span wing

In the two-dimensional case, the vorticity was exclusively perpendicular to the direction of the flow. However, in a three-dimensional flow, vorticity components parallel to the flow can appear, influencing the nearby flow velocity. Let us see how this happens.

When a wing passes through a fluid, the pressure on its lower surface is greater than on its upper surface. This net imbalance results in a force called lift. However, approaching the wingtips, this pressure difference implies that the air is forced to go around the tips, from the high to the low pressure region. The air thus rolls-up, creating two counter-rotating vortices, that are spread behind the wing (see Figure 1.2). Those vortices can be modelled as a pair of semi-infinite vortex lines, each emanating from one wingtip.

Figure 1.2: Wingtip vortices. *Source : www.airliners.net*

Concretely, the kinetic energy associated with those vortices must be supplied by the moving wing, in the form of a force: the *induced drag* [6].

1.2.1 Lifting line theory

Reference frame

The reference frame is defined here as the *x-axis* in the flow direction and the *y-axis* spanwise (see Figure 1.3).

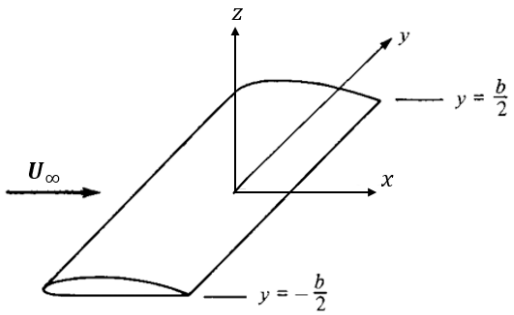

Figure 1.3: Reference frame

The Biot-Savart Law

Before going on to the lifting line theory, we must introduce the Biot-Savart Law, as it explains what we subsequently call the *downwash velocity*.
This law states that a vortex filament induces a flow field in its surrounding space. For example, let us take a portion $\vec{dl}$ of such a vortex line of strength Γ. At a given point P, spaced from the vortex filament by a distance $\vec{r}$, the induced velocity is expressed in 3D as (see Figure 1.4) :

$$d\vec{U} = \frac{\Gamma}{4\pi} \frac{\vec{dl} \times \vec{r}}{|\vec{r}|^3} \ . \tag{1.6}$$

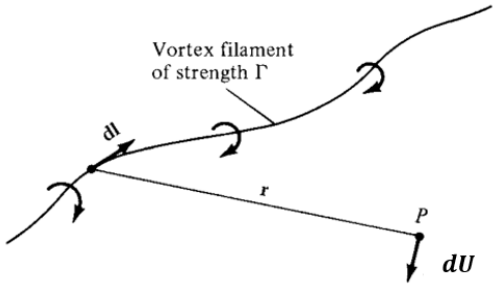

Figure 1.4: Biot-Savart Law representation. *Source : Fundamentals of aerodynamics, J.D. Anderson [5]*

Horseshoe vortex

In the early 20^{th} century, Ludwig Prandtl developed a practical theory for predicting the aerodynamic properties of a finite span wing. We will here below explain his reasoning. As seen in Eq. (1.3), the lift per unit length of span is proportional to the circulation Γ of that section.
In a first modelling step, Prandtl replaced a finite wing of span b (producing a lift L') by a vortex filament of strength Γ', called a "bound vortex", so that

$$L' = \rho \, U_\infty \, \Gamma' \, b \ .$$

However, the Helmholtz's theorem specifies that a vortex filament cannot end in a fluid. Therefore, at each end of the bound vector (at $y = -b/2$ and $y = b/2$), a semi-infinite vortex line (called trailing vortex), corresponding to the wingtip vortices, can be added. He then obtained then the famously known *Horseshoe vortex* (see Figure 1.5).

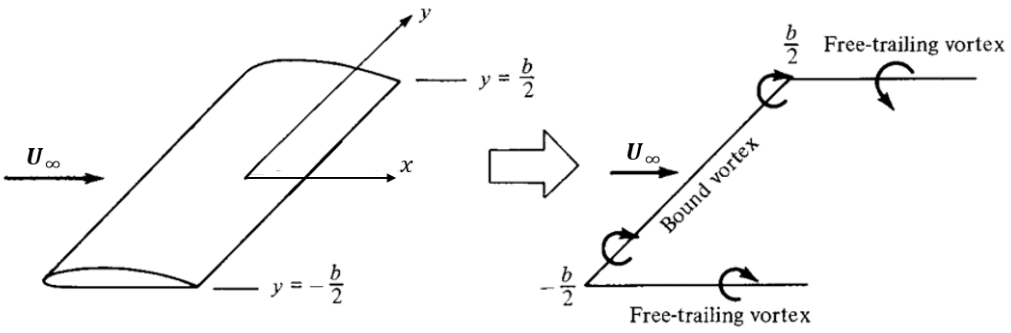

Figure 1.5: Simple horseshoe vortex

Downwash velocity

Using the Biot-Savart Law for such a configuration, we can easily see that the two trailing vortices induce a velocity pointing in the negative z *axis* direction for $y = [-b/2; b/2]$. This "downward motion" is called the *downwash velocity*, denominated w. For the simple horseshoe (Figure 1.5), the downwash can be expressed as :

$$w(y) = -\frac{\Gamma}{4\pi}\frac{b}{(b/2)^2 - y^2} \ . \tag{1.7}$$

In fact, an assumption such as taking a constant value for the bound vortex is not realistic; the value of Γ must vary along the span (from $y = -b/2$ to $y = b/2$), such that each profile of the wing has its own value $\Gamma(y)$.

So, instead of representing a finite wing with a single horseshoe vortex, Prandtl superimpose several horseshoe vortices, with their respective bound vortices aligned on a same line : *the lifting line*. Consequently, we can superimpose an infinite amount of horseshoes, which will give us a continuously defined Γ along the lifting line (see Figure 1.6).

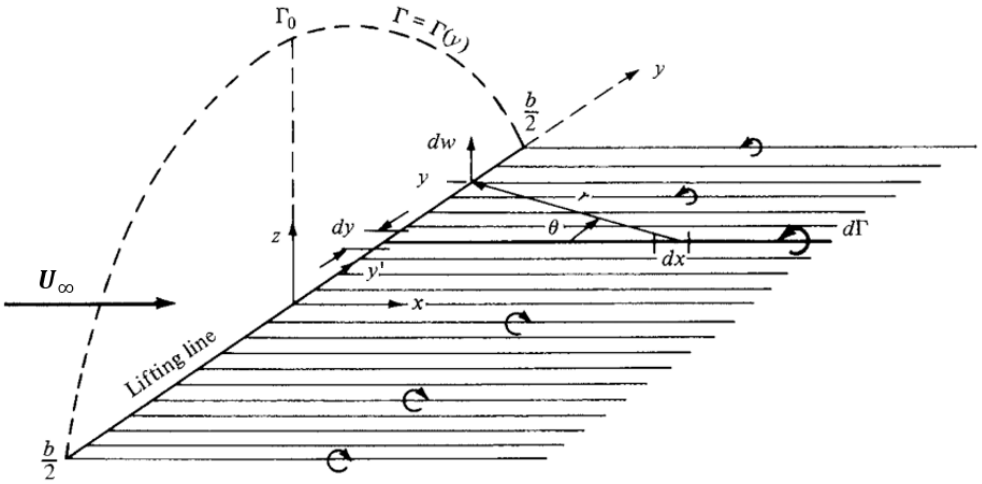

Figure 1.6: Infinite amount of horseshoes. *Source : Fundamentals of aerodynamics, J.D. Anderson [5]*

The wing thus sheds a vortex sheet in its wake and as mentioned above, this vortex sheet will roll up, until the formation of two vortices of opposite signs of vorticity (with corresponding circulation $\pm\Gamma_0$), separated from each other by a distance b_0 (measured from centre to centre) (see Figure 1.7) are formed, such that

$$L = \rho \ U_\infty \ \Gamma_0 \ b_0 \ . \tag{1.8}$$

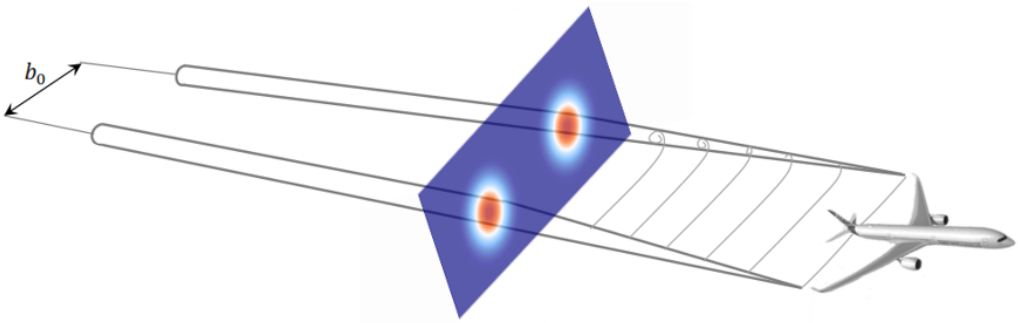

Figure 1.7: Distance b_0 between the two vortices. *Source : LMECA2323 [4]*

Along the lifting line, the circulation at a given location y is $\Gamma(y)$ and any change in the circulation over a segment dy is given by $d\Gamma = \frac{d\Gamma}{dy}(y)dy$: this corresponds to the amount of vorticity that must be shed in the wake to satisfy the Helmoltz's theorem.
Thus, for a given location y along the y-axis, the resulting trailing vortex will induce a velocity which can be expressed using the Biot-Savart's Law, as follows :

$$dw(y) = -\frac{1}{4\pi}\frac{1}{(y-y')}\frac{d\Gamma(y')}{dy'}dy' \ . \tag{1.9}$$

The total induced velocity at y is now simply given by the integral of (1.9) over the span b :

$$w(y) = -\frac{1}{4\pi}\int_{-b/2}^{b/2}\frac{1}{(y-y')}\frac{d\Gamma}{dy'}(y')\,dy' \ . \tag{1.10}$$

This "downwash" velocity is seen by the wing as an induced angle of attack ϵ which is given by :

$$\epsilon(y) = tan^{-1}\left(\frac{-w(y)}{U_\infty}\right) \ . \tag{1.11}$$

But as $w(y) \ll U_\infty$, we can simplify (1.11) with :

$$\epsilon(y) = -\frac{w(y)}{U_\infty} \ . \tag{1.12}$$

Effective angle of attack, without twist

This induced angle of attack decreases the geometric angle of attack (α), as seen in Figure 1.8.

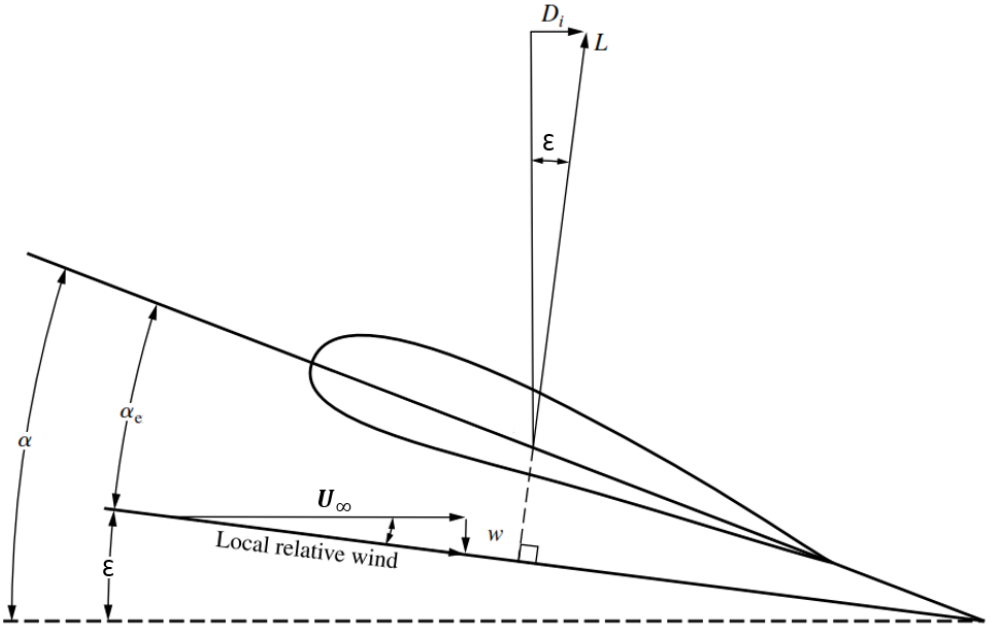

Figure 1.8: Downwash effect and effective angle of attack representation. *Source : Fundamentals of aerodynamics, J.D. Anderson [5]*

In turn, the local angle of attack seen by the wing is called the *effective angle of attack* α_e and is defined by :

$$\alpha_e(y) = \alpha(y) - \epsilon(y) \approx \alpha(y) + \frac{w(y)}{U_\infty} \ . \tag{1.13}$$

The effective velocity vector under the wing is then no longer parallel to the upstream velocity vector, and as the lift force must be perpendicular to the local velocity vector, a drag component appears, as seen in Figure 1.8. This drag component is the previously explained *induced drag* and can be expressed locally as

$$d_i(y) = l(y) sin(\epsilon(y)) \approx l(y)\epsilon(y) \ , \tag{1.14}$$

as $sin(\epsilon(y)) \approx \epsilon(y)$ with $\epsilon(y) \ll 1$.

We finally obtain, for the entire wing :

$$L = \int_{-b/2}^{b/2} l(y)\, dy = \rho U_\infty \int_{-b/2}^{b/2} \Gamma(y)\, dy \ , \tag{1.15}$$

$$D_i = \int_{-b/2}^{b/2} l(y)\epsilon(y)\, dy \ . \tag{1.16}$$

Effective angle of attack, with twist

The twist angle $\alpha_v(y)$ is defined in y as the change in geometric angle of attack relative to the central profile. We define it here as positive when it increases the angle of attack, and negative when it decreases it (see Figure 1.9).

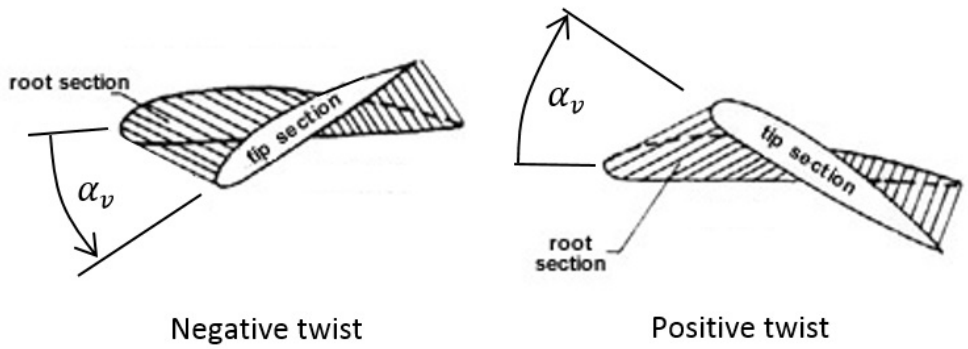

Figure 1.9: Twist definition. *Source : www.pilotfriend.com*

Therefore, the effective angle of attack at a position y is :

$$\alpha_e(y) = \alpha(y) + \alpha_v(y) - \epsilon(y) \ . \tag{1.17}$$

Prandtl's compatibility equation

Before deriving the compatibility relation, it is important to stress that this theory is only valid for wings with an aspect ratio $A_R \gg 1$. The aspect ratio is defined as :

$$A_R \triangleq \frac{b}{\overline{c}} = \frac{b^2}{S} \ ,$$

with S the wing area and $\overline{c}$ the wing mean chord.
The lift (1.18) and drag (1.19) for the whole wing is defined as :

$$L = \frac{1}{2}\rho U_\infty^2 S C_L \ , \tag{1.18}$$

$$D = \frac{1}{2}\rho U_\infty^2 S C_D \ , \tag{1.19}$$

with S the wing area, C_L and C_D the non-dimensional coefficients for lift and drag. However, the lift per unit span at a location y is given by :

$$l(y) = \frac{1}{2}\rho U_\infty^2 c(y) C_l \ , \tag{1.20}$$

with $c(y)$ the local chord of the wing at the location y.
On the basis of the *thin airfoil theory*, we can ascertain that the coefficient of lift for an airfoil :

$$C_l = a_0 \alpha_e \ , \tag{1.21}$$

with a_0 the *lift slope* and (for small angles of attack) defined as :

$$a_0 = \frac{dC_l}{d\alpha} \approx 2\pi \ . \tag{1.22}$$

By combining equations (1.3), (1.20) and (1.21), we can derive the famous *Prandtl's compatibility equation* :

$$\begin{aligned} \Gamma(y) &= \frac{l(y)}{\rho U_\infty} \ , \\ &= \frac{\frac{1}{2}\rho U_\infty^2 c(y) C_l}{\rho U_\infty} \ , \\ &= \frac{1}{2} U_\infty c(y) a_0 \alpha_e \ . \end{aligned} \tag{1.23}$$

Remembering the definitions of the effective angle of attack and the downwash velocity, this becomes :

$$\Gamma(y) = \frac{1}{2} U_\infty c(y) a_0 \left[\alpha(y) + \alpha_v(y) - \epsilon(y)\right] \ ,$$

$$\Big\downarrow (1.11) \textit{ and } (1.10)$$

$$\Gamma(y) = \frac{1}{2} U_\infty c(y) a_0 \left[\alpha(y) + \alpha_v(y) - \frac{1}{U_\infty}\frac{1}{4\pi}\int_{-b/2}^{b/2} \frac{1}{(y-y')}\frac{d\Gamma}{dy'}(y')\, dy'\right] \ . \tag{1.24}$$

Equation (1.24) is *Prandtl's compatibility equation*. This relation is very useful as it allows us to determine the distribution of circulation along the wing span and in term, derive the expression for the lift, drag, ...
Once Prandtl had obtained this relation, he performed a change of variable, such that $y = \frac{b}{2} cos(\theta)$ with $0 \leq \theta \leq \pi$.
We can now write, using the sine decomposition,

$$\Gamma(\theta) = (U_\infty b) \sum_n B_n sin(n\theta) \ . \tag{1.25}$$

It is important at that point to clarify the expressions for the B_n coefficients, as we will need this further on in our calculations. For a wing without twist,

$$B_n = b_n \alpha \ . \tag{1.26}$$

For a wing with twist,

$$B_n = b_n\alpha + d_n \ , \tag{1.27}$$

with b_n the same for both expressions (we will use this property later on).
We can now re-express the relation for the downwash velocity ϵ with the new variable :

$$\begin{aligned}
\epsilon(\theta) = & \ \frac{1}{U_\infty}\frac{1}{4\pi}\int_{-b/2}^{b/2}\frac{1}{(y-y')}\frac{d\Gamma}{dy'}(y')\,dy' \ , \\
= & \ \frac{1}{U_\infty}\frac{1}{4\pi}\int_0^\pi \frac{1}{(-b/2)(cos(\theta)-cos(\theta'))}\frac{d\Gamma}{d\theta'}(\theta')\,d\theta' \ , \\
= & \ \frac{1}{2\pi}\sum_n nB_n\int_0^\pi \frac{cos(n\theta')}{(cos(\theta')-cos(\theta))}\,d\theta' \ , \\
= & \ \frac{1}{2}\sum_n\left(nB_n\frac{sin(n\theta)}{sin(\theta)}\right) \ .
\end{aligned} \tag{1.28}$$

We can now re-write the expression for the compatibility equation with the new variable, putting equations (1.25) and (1.28) into (1.24) :

$$\sum_n\left(B_n sin(n\theta)\right) = \frac{1}{2}a_0\frac{c(\theta)}{b}\left[\alpha(\theta)+\alpha_v(\theta)-\frac{1}{2}\sum_n\left(nB_n\frac{sin(n\theta)}{sin(\theta)}\right)\right] \ . \tag{1.29}$$

This is one of the most fundamentals equations for aerodynamics analysis, as it makes it possible to determine the wing characteristics with simple calculations, based on its geometry.
After some elementary manipulations, we can express the lift and induced drag of the wing as :

$$L = \frac{\rho U_\infty^2}{2}b^2\frac{\pi}{2}B_1 \ , \tag{1.30}$$

$$D_i = \frac{\rho U_\infty^2}{2}\frac{b^2}{2}\frac{\pi}{2}\sum_n\left(nB_n^2\right) \ , \tag{1.31}$$

We can here highlight the fact that the lift only depends on one coefficient B_1 although the induced drag depends on all the B_n coefficients.

We can now non-dimensionnalise (1.30) and (1.31) by dividing them by $\frac{1}{2}\rho U_\infty^2 S$:

$$C_L = \frac{\pi}{2} A_R B_1 \ , \tag{1.32}$$

$$\begin{aligned} C_{D_i} &= \frac{\pi}{4} A_R \left(\sum_n n B_n^2 \right) \ , \\ &= \frac{\pi}{4} A_R B_1^2 \left(\sum_n n \left(\frac{B_n}{B_1} \right)^2 \right) \ , \\ &= \frac{1}{\pi A_R} C_L^2 \left(\sum_n n \left(\frac{B_n}{B_1} \right)^2 \right) \ , \\ &= \frac{1}{\pi A_R \ e} C_L^2 \ , \end{aligned} \tag{1.33}$$

with *Oswald's efficiency* e defined as :

$$e \triangleq \left(\sum_n n \left(\frac{B_n}{B_1} \right)^2 \right)^{-1} \leq 1 \ . \tag{1.34}$$

This efficiency is very useful to analyse two wings of same aspect ratio. It reflects the amount of induced drag a certain wing produces compared to an ideal wing (see next section).

One last consideration is to take a look at the drag coefficient C_D. One can divide the drag into two distinct forms : the (skin) friction drag and the pressure drag. The former may be represented by a constant : C_{D_0}. The latter depends directly on the lift produced by the wing. Therefore, a good way to model the drag at low angles of attack is:

$$C_D = C_{D_0} + k C_L^2 \ , \tag{1.35}$$

with $k = \frac{1}{\pi A_R \ e}$. Relation (1.35) can be plotted as what we call the *polar of a wing.*

1.2.2 The perfect wing

The "perfect" wing is defined as the one which produces the least drag for a given lift [4]. This is characterized by an Oswald's efficiency $e = 1$.
Mathematically, this is expressed as the ratio $\frac{C_{D_i}}{C_L}$ being minimal. Looking at Eq. (1.33), this means that all the B_n coefficients except B_1 must be nil ($B_1 \neq 0, B_3 = B_5 = ... = 0$). Furthermore, we can easily derive the expression for the circulation distribution, the downwash

velocity and the chord distribution :

$$\Gamma(\theta) = U_\infty \; b \; B_1 \; sin(\theta) \; , \tag{1.36}$$

$$\epsilon(\theta) = \frac{1}{2} B_1 \; , \tag{1.37}$$

$$c(\theta) = \frac{4}{\pi} \; \overline{c} \; sin(\theta) \; . \tag{1.38}$$

Several characteristics have to be deduced from the above expressions :

- The downwash velocity is uniform along the span.
- As soon as there is no twist, the effective angle of attack $\alpha_e(\theta)$ is also uniform along the span.
- The chord and circulation distributions are elliptical.

A well known aircraft using those properties was the *Supermarine Spitfire* (see Figure 1.10).

Figure 1.10: A look of the Spitfire's chord distribution. *Source : www.nms.ac.uk*

1.2.3 The Prandtl's wing

The perfect wing depicted above only takes into account the minimal drag for a given lift. However, in 1933, Prandtl wrote a note [2] in which he claimed that the optimal wing calculation should include the "total amount of structural material". The conclusion of his theory was that this new wing design was such that it produced 11 percent less of induced drag than the elliptical wing. As this concept is the major foundation of this thesis, we will detail the analysis carried out by Prandtl.

From the Kutta-Joukowski theorem, we know :

$$L = \rho\, U_\infty \int_{-b/2}^{b/2} \Gamma(y)\, dy \ .$$

In his note, Prandtl also considered the bending moment M of the wing (see Figure 1.11) (which is closely related to the structural mass of the wing) :

$$M(y) = \rho\, U_\infty \int_{y}^{b/2} \Gamma(y')\ (y' - y)\, dy' \ . \tag{1.39}$$

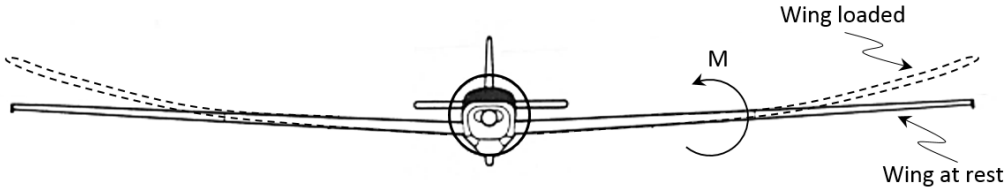

Figure 1.11: Bending moment M over a wing. *Source : www.scalesoaring.co.uk*

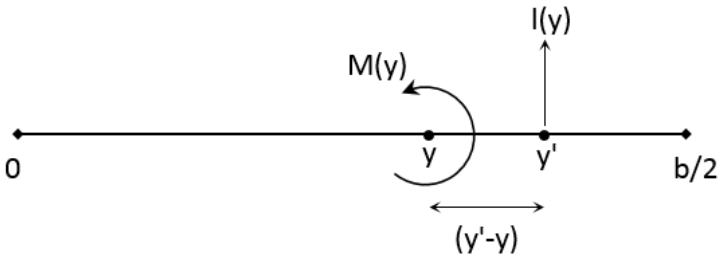

Figure 1.12: Bending moment details for Eq. (1.39)

The bending moment on the whole wing is computed such that:

$$\begin{aligned} Q \triangleq &= \int_0^{b/2} M(y)\, dy \ , \\ &\Big\downarrow \textit{Integration by parts} \\ &= [M(y)y]_0^{b/2} - \int_0^{b/2} \frac{dM}{dy}(y)\ y\, dy \ , \\ &= -\int_0^{b/2} \frac{dM}{dy}(y)\ y\, dy \ . \end{aligned} \tag{1.40}$$

We can prove, with the Leibniz rule, that :

$$\frac{dM}{dy}(y) = -\rho\, U_\infty \int_{y}^{b/2} \Gamma(y')\, dy' \ . \tag{1.41}$$

Substituting (1.41) into (1.40), we get

$$Q = \rho\, U_\infty \int_0^{b/2} \left(\int_y^{b/2} \Gamma(y')\, dy' \right) y\, dy \ ,$$

$$\Big\downarrow \textit{Integration by parts}$$

$$= \rho\, U_\infty \left(\left[\frac{y^2}{2} \int_y^{b/2} \Gamma(y')\, dy' \right]_0^{b/2} + \int_0^{b/2} \frac{y^2}{2} \Gamma(y)\, dy \right) \ .$$

Finally, we obtain

$$Q = \int_0^{b/2} M(y)\, dy = \rho\, U_\infty \int_0^{b/2} \frac{y^2}{2} \Gamma(y)\, dy \ . \tag{1.42}$$

In the end, we have the next equations system for both wings :

$$L = \rho\, U_\infty \int_{-b/2}^{b/2} \Gamma(y) dy \ , \tag{1.43}$$

$$Lr^2 = 2Q = \rho\, U_\infty \int_{-b/2}^{b/2} y^2 \Gamma(y) dy \ , \tag{1.44}$$

r is called the *radius of gyration*. This quantity is useful to characterise the stiffness of a slender object. It can be interpreted as the distance from a given axis where all the mass of the object could be contracted without altering the rotation interia of the body around its axis. It is defined as : $r = \sqrt{\frac{I}{A}}$ with I the quadratic moment and A a section area.
Let us remember the definition of the downwash angle, which we can express as :

$$D_i = \rho \int_{-b/2}^{b/2} \Gamma(y) w(y)\, dy \ . \tag{1.45}$$

The goal of Prandtl was then to minimize (1.45) by keeping L and r (and so Lr^2) fixed, so that the stiffness of the wing would not be altered (nor its structural mass), whatever the circulation distribution could be. He obtained the following results, with $\xi \triangleq \frac{y}{b/2}$:

$$w(y) = C_1 + C_2 \xi^2 \left(\frac{b}{2} \right)^2 \ , \tag{1.46}$$

$$\Gamma(y) = \left(\Gamma_0 + \Gamma_2 \xi^2 \right) \sqrt{1 - \xi^2} \ , \tag{1.47}$$

$$C_1 = \frac{1}{2b} \left(\Gamma_0 - \frac{1}{2} \Gamma_2 \right) \ , \tag{1.48}$$

$$C_2 = \frac{6}{b^3} \Gamma_2 \ . \tag{1.49}$$

By combining (1.46) with (1.48) and (1.49) and defining $\mu \triangleq -\frac{\Gamma_2}{\Gamma_0}$, we get the final result :

$$w(y) = \frac{1}{2b}\Gamma_0 \left(1 + \frac{\mu}{2} - 3\mu\xi^2\right) \ , \tag{1.50}$$

$$\Gamma(y) = \Gamma_0 \left(1 - \mu\xi^2\right)\sqrt{1-\xi^2} \ . \tag{1.51}$$

We can stress here that $\mu = 0$ corresponds to the elliptic wing.
Using those relations, we can now proceed to a variable change in equations (1.43) and (1.44), do the integrals and re-express them as :

$$L = \frac{\pi}{4}\rho \ b \ U_\infty \ \Gamma_0 \left(1 - \frac{\mu}{4}\right) \ , \tag{1.52}$$

$$= \rho \ U_\infty \ \Gamma_0 \ b_0 \ ,$$

$$\longrightarrow b_0 = \frac{\pi}{4}\left(1 - \frac{\mu}{4}\right) b \tag{1.53}$$

$$Lr^2 = \frac{\pi}{64}\rho \ b^3 \ U_\infty \ \Gamma_0 \left(1 - \frac{\mu}{2}\right) \ . \tag{1.54}$$

We can now take a look back at all the work achieved in this section, and remember that Prandtl's main goal (and ours, obviously) was to design a wing producing less induced drag than the so-called "optimal" elliptical wing with the same structural mass. Equations (1.52) and (1.54) provide us with the right tools to do so. In fact, we can divide (1.54) by (1.52) and get the expression for r^2 and in turn, the one for b :

$$r^2 = \frac{1}{16}b^2 \frac{\left(1 - \frac{\mu}{2}\right)}{\left(1 - \frac{\mu}{4}\right)} \ , \tag{1.55}$$

$$b = 4r\sqrt{\frac{\left(1 - \frac{\mu}{4}\right)}{\left(1 - \frac{\mu}{2}\right)}} \ . \tag{1.56}$$

We can now also easily derive the expression for the induced drag (from (1.45)) and Γ_0 :

$$D_i = \frac{L^2}{8\pi \ \rho \ U_\infty^2 \ r^2} \frac{\left(1 - \frac{\mu}{2}\right)\left(1 - \frac{\mu}{2} + \frac{\mu^2}{4}\right)}{\left(1 - \frac{\mu}{4}\right)^3} \ , \tag{1.57}$$

$$\Gamma_0 = \frac{L}{\pi \ \rho \ U_\infty \ r}\sqrt{\frac{\left(1 - \frac{\mu}{2}\right)}{\left(1 - \frac{\mu}{4}\right)^3}} \ . \tag{1.58}$$

We should now choose the value of μ that will characterise the Prandtl's wing. This value should be taken between $\mu = 0$ and $\mu = 1$. In fact, if we take a step back on the situation, we

remember that the purpose of the Prandtl's theory is to take the structural mass of the wing into account in its calculation. Prandtl achieved that by adding virtual spar weights along the span, corresponding to the local bending moment of the wing. Those weights would represent the wing's structural mass necessary to carry out that bending moment. So, as this moment would increase, so would the spar weights.
Now, if we go back to Eq. 1.51, we see that for $\mu > 1$, the circulation around wingtips becomes negative, which in turn, corresponds to negative lift (Figure 1.13).

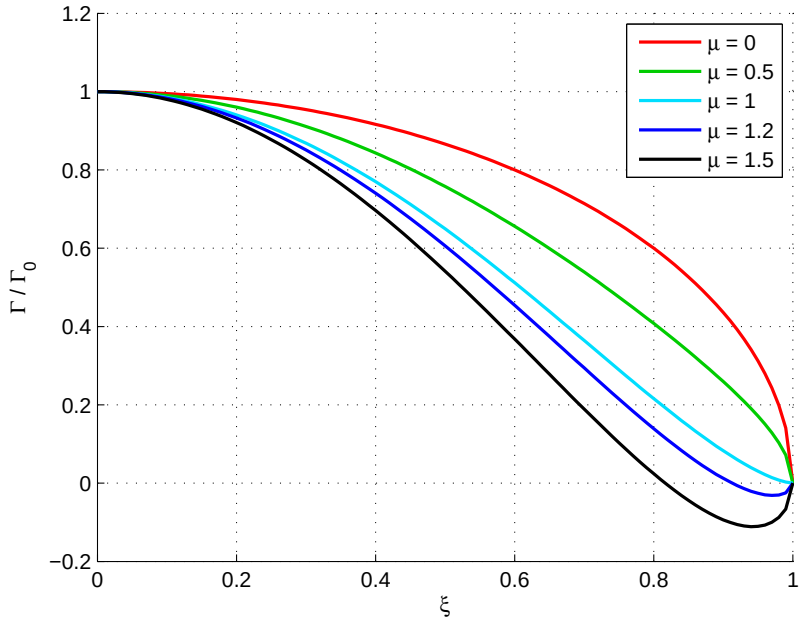

Figure 1.13: Circulation distribution against span for different values of μ

Therefore, negative spar weights should be added but obviously, that would not make any sense and the whole foundation of this theory would no longer be valid. So, the value of μ is then to be taken between 0 and 1.
As we want to minimise the produced induced drag, $\mu = 1$ should be chosen as it corresponds to a minimum of Eq. (1.50).
Remembering that this minimisation was made with a fixed value of r (and thus also r^2), the next steps necessary to obtain the geometrical characteristics will be simple :

1. Compute the value of r for the elliptical wing : r_{ell}, with $\mu = 0$ and $b = b_{ell} = 1$ in the Eq. (1.55).

2. Inject r_{ell} in (1.56) with $\mu = 1$ to compute the span b for the Prandtl wing : $b_{Prandtl}$.

Here below are the results :

We see here that for a given lift and structural mass (r), the Prandtl wing must be 22.47% wider than the elliptic wing. This is a major consequence from the Prandtl's theory. Both wings will not have the same span while having the same wing area (as the lift is fixed and $L = \frac{1}{2}\rho U_\infty S C_L$). Therefore, their aspect ratio will not be equal either :

Planform	μ	b/b_{ell}	r/b_{ell}
Elliptic	0	1	0.25
Prandtl	1	1.2247	0.25

Table 1: Span comparison between the two wings

$$A_{R,Prandtl} = \frac{b^2_{Prandtl}}{S} = \frac{1.2247^2\ b^2_{ell}}{S} = 1.2247^2\ A_{R,ell}\ ,$$

$$\approx 1.5\ A_R, ell\ .$$

Also, Eq. (1.50) changes signs at $\xi = \frac{1}{\sqrt{2}}$. The downwash velocity becomes then upwash velocity past that point.
We can now study the induced drag produced by the two wings, by comparing $D_i / \left(\frac{L^2}{8\pi\ \rho\ U^2_\infty\ r^2}\right)$ (see Eq. (1.57)).

Planform	μ	$\frac{\left(1-\frac{\mu}{2}\right)\left(1-\frac{\mu}{2}+\frac{\mu^2}{4}\right)}{\left(1-\frac{\mu}{4}\right)^3}$
Elliptic	0	1
Prandtl	1	0.8889

Table 2: Induced drag comparison between the two wings

As we see in Table 2, **the Prandtl's wing produces 11% less induced drag than the "optimal" elliptical wing** ! This conclusion is considerable as it shows that a simple extension of the span by 22% and a special circulation distribution can lead to such a reduction in induced drag. The main goal of this thesis is to experimentally prove this statement.

Figure 1.14 is a representation of the circulation distribution for the elliptical and Prandtl's wings. Due to its "bell shape" circulation curve, we will from now on call the Prandtl's wing the *bell wing* or *bell-shaped wing*.

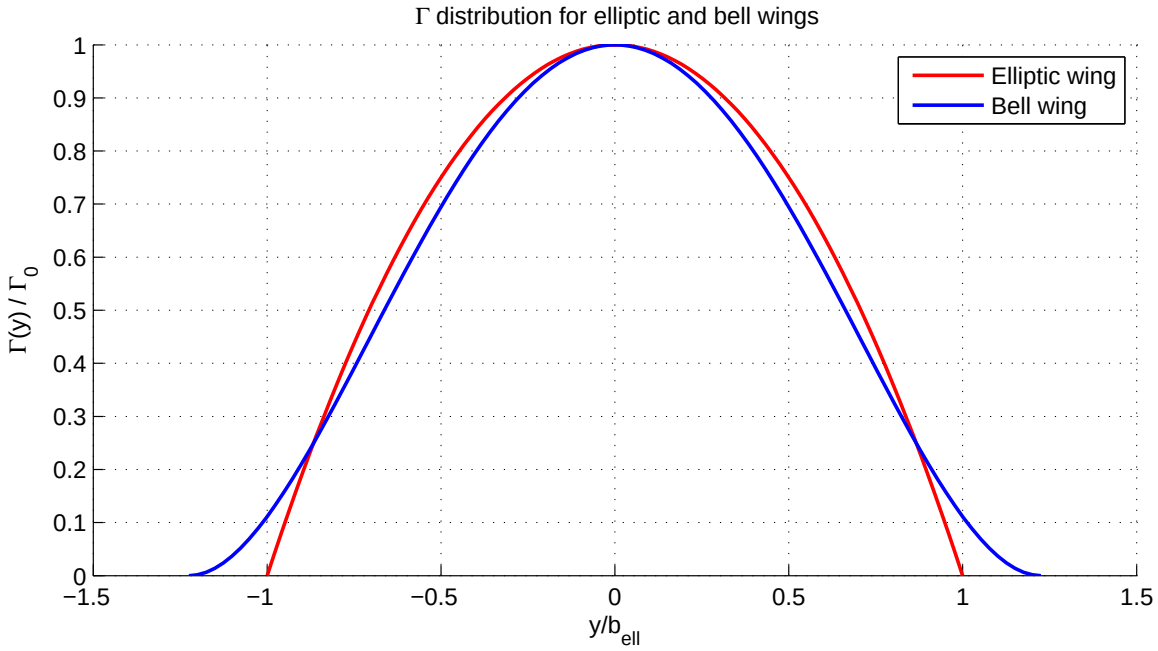

Figure 1.14: Gamma circulation comparison

2 Experimental setup

Back in 2010, *Julien Jansen and Arnaud Wiertz* published their Masters's thesis [7] which was all about comparing an elliptical wing to a rectangular wing. To this end, they manufactured both wings. Fortunately for us, we can still use the elliptical wing in our thesis. It has a span $b = 0.3$ $[m]$, a wing area $S = 0.015$ $[m^2]$, an aspect ratio $A_R = 6$ and a *NACA0012* profile [8]. *NACA* stands for *National Advisory Committee for Aeronautics* and 0012 for a wing without camber and with a thickness-chord ratio equal to 0.12 ($\frac{thickness}{chord} = 0.12$) (Figure 2.1). All we had to do next was to create our bell wing in order to compare it with the elliptical one (a summary of both geometries is shown at the end of this section).

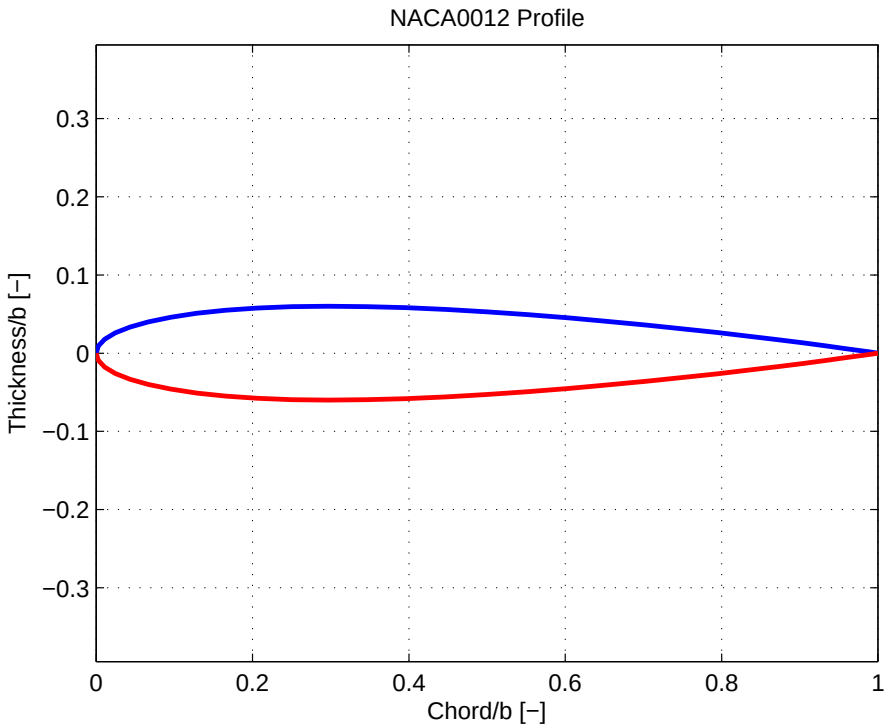

Figure 2.1: NACA0012 Profile

In this section, we will describe all the work done to design and produce our wing. Furthermore, we will explain the experimental setup to analyse that wing, going from the wind tunnel specifications [9] [10], to the *PIV (Particle Image Velocimetry)* system [11].

2.1 *Bell wing* design

We will now detail each step of the design process we followed to obtain our final wing.

2.1.1 Circulation distribution $\Gamma(y)$

In the previous section, we saw that the circulation distribution $\Gamma(y)$ of our wing had to follow the Eq. (1.51) with $\mu = 1$ and $\xi = \frac{y}{b/2}$, such that :

$$\Gamma(y) = \Gamma_0 \left(1 - \xi^2\right)^{3/2} \ . \tag{2.1}$$

The remaining step is thus to define Γ_0. To do so, we proceed to the following variable change : $\xi = -cos(\theta)$. (2.1) then becomes:

$$\begin{aligned}
\Gamma(\theta) &= \Gamma_0 \left(1 - cos^2(\theta)\right)^{3/2} \ , \\
&= \Gamma_0 \ sin^3(\theta) \ , \\
&= \Gamma_0 \left(\frac{3}{4} sin(\theta) - \frac{1}{4} sin(3\theta)\right) \ , \\
&= \frac{3}{4}\Gamma_0 \left(sin(\theta) - \frac{1}{3} sin(3\theta)\right) \ .
\end{aligned}$$

We can now equalize this equation to $\Gamma(\theta) = (U_\infty b) \sum_n B_n sin(n\theta)$ and by identification, we find the following identities :

$$\Gamma_0 = \frac{4}{3} \ U_\infty \ b \ B_1 \ , \tag{2.2}$$

$$\frac{B_3}{B_1} = -\frac{1}{3} \ \Leftrightarrow \ \frac{b_3}{b_1} = -\frac{1}{3} \ . \tag{2.3}$$

Recalling the definition of Oswald's efficiency $e \triangleq \left(\sum_n n \left(\frac{B_n}{B_1}\right)^2\right)^{-1}$, we get, for the bell wing :

$$e_{bell} = \frac{3}{4} \ .$$

Also, we remember that in the previous section, we highlighted the fact that the global coefficient of lift of the wing only depends on the B_1 coefficient (conversely to the drag where all the B_n are involved). We can thus write the wing lift coefficient as $C_L = \frac{\partial C_L}{\partial \alpha}\alpha = A_0\alpha = \frac{\pi}{2} A_R \ b_1 \alpha$ and isolate A_0 :

$$A_0 = \frac{\pi}{2} A_R \ b_1 \ \Leftrightarrow \ b_1 = \frac{2}{\pi} \frac{A_0}{A_R} \ . \tag{2.4}$$

2.1.2 Chord distribution $c(y)$

To determine the chord distribution $c(y)$ of the bell wing (here **without twist**), we can revert to the compatibility equation

$$\sum_n B_n sin(n\theta) = \frac{1}{2} a_0 \frac{c(\theta)}{b} \left[\alpha - \frac{1}{2} \sum_n \left(n B_n \frac{sin(n\theta)}{sin(\theta)}\right)\right] \ .$$

As we do not have any twist, we can divide each member of this equation by α and get :

$$\sum_n b_n sin(n\theta) = \frac{1}{2} a_0 \frac{c(\theta)}{b} \left[1 - \frac{1}{2} \sum_n \left(n b_n \frac{sin(n\theta)}{sin(\theta)} \right) \right] .$$

As we saw earlier, only b_1 and b_3 are taken into account for the circulation distribution. Using the definition of the aspect ratio A_R, the mean chord $\overline{c}$ and the relation (2.4), we can write :

$$\sum_n b_n sin(n\theta) = \frac{1}{2} \frac{a_0}{A_R} \frac{c(\theta)}{\overline{c}} \left[1 - \frac{1}{2} \sum_n \left(n b_n \frac{sin(n\theta)}{sin(\theta)} \right) \right] ,$$

$$\Leftrightarrow \; b_1 \left(sin(\theta) + \frac{b_3}{b_1} sin(3\theta) \right) = \frac{1}{2} \frac{a_0}{A_R} \frac{c(\theta)}{\overline{c}} \left[1 - \frac{1}{2} b_1 \left(1 + 3 \frac{b_3}{b_1} \frac{sin(3\theta)}{sin(\theta)} \right) \right] ,$$

$$\Leftrightarrow \; \frac{2}{\pi} \frac{A_0}{A_R} \left(sin(\theta) - \frac{1}{3} sin(3\theta) \right) = \frac{1}{2} \frac{a_0}{A_R} \frac{c(\theta)}{\overline{c}} \left[1 - \frac{1}{\pi} \frac{A_0}{A_R} \left(1 - \frac{sin(3\theta)}{sin(\theta)} \right) \right] ,$$

$$\Leftrightarrow \; \frac{c(\theta)}{\overline{c}} = \frac{\frac{2}{\pi} \frac{A_0}{A_R} \left(sin(\theta) - \frac{1}{3} sin(3\theta) \right)}{\frac{1}{2} \frac{a_0}{A_R} \left[1 - \frac{1}{\pi} \frac{A_0}{A_R} \left(1 - \frac{sin(3\theta)}{sin(\theta)} \right) \right]} ,$$

$$\Leftrightarrow \; \frac{c(\theta)}{\overline{c}} = \frac{\frac{4}{\pi} \left(sin(\theta) - \frac{1}{3} sin(3\theta) \right)}{\frac{a_0}{A_0} - \frac{a_0}{A_R} \left(1 - \frac{sin(3\theta)}{sin(\theta)} \right)} . \tag{2.5}$$

We have thus expressed the chord distribution as a function of two ratios : $\frac{a_0}{A_R}$, $\frac{a_0}{A_0}$ and with the "bell" circulation distribution. For a_0 and A_R fixed, the only parameter to determine is thus $\frac{a_0}{A_0}$. We fix it by enforcing the constraint :

$$\int_{-b/2}^{b/2} c(y)\, dy = S = \overline{c} b ,$$

$$\Big\downarrow y = -\frac{b}{2} cos(\theta)$$

$$\int_0^{\pi} \frac{c(\theta)}{\overline{c}} \frac{b}{2} sin(\theta)\, d\theta = b ,$$

$$\int_0^{\pi} \frac{c(\theta)}{\overline{c}} sin(\theta) = 2 ,$$

$$\int_0^{\pi/2} \frac{c(\theta)}{\overline{c}} sin(\theta) = 1 . \tag{2.6}$$

Remembering that the wing area of the bell wing must be the same as the elliptical wing ($S = 0.015\ [m^2]$) and its span is 1.225 times bigger than that of the elliptical wing ($b_{bell} = 0.3675\ [m]$), we find the following chord distribution:

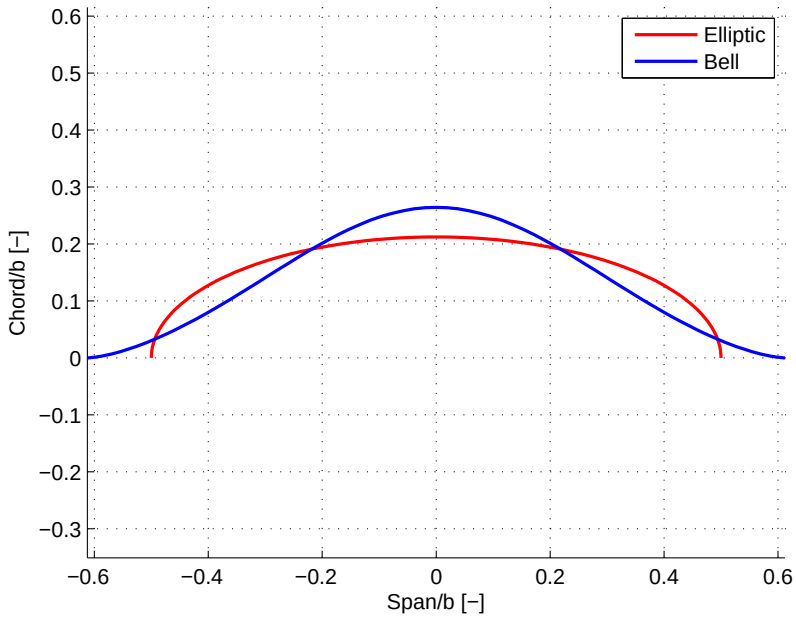

(a) Chord distribution along the span for the bell and elliptic wings.

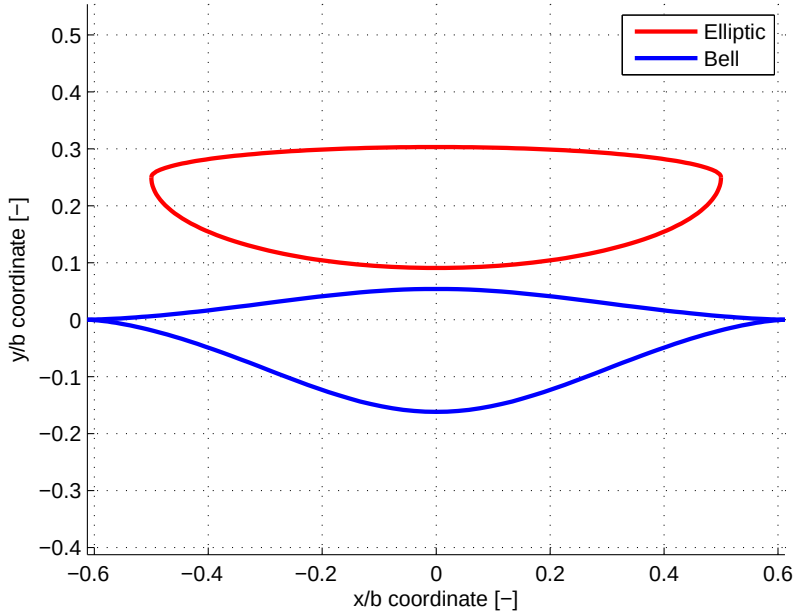

(b) Representation of bell and elliptic wings with one quarter chord on the same line

Figure 2.2: Different chords distributions for the bell and elliptical wings

However, as we see in Figure 2.2, the chord of the bell wing at the wingtips is zero. This is obviously impossible to make. We thus have to choose another chord distribution. Nonetheless, this will induce a change in the $\Gamma(y)$ distribution, but the absolute goal is to keep the bell $\Gamma(y)$ distribution as it offers better performance to the wing. How can that be achieved ?
We would recall that this chord distribution was found with no twist added to the wing. By **adding twist**, we gain one degree of freedom in the compatibility equation, which will allow us to fix a certain geometry and also keep the bell circulation distribution.

2.1.3 Calculation of twist

Before going on into the calculation method, we must define how the twist is represented in the compatibility equation. We recall that for a wing without twist, the B_n coefficients are defined as

$$B_n = b_n \alpha \ , \tag{2.7}$$

α representing the wing geometrical angle of attack. The calculation method to find b_n requires a numerical resolution, which is detailed in Appendix (A) and (B). It is important to note that b_n only depends on the chord distribution and the span of the wing.
For a twisted wing, the B_n coefficients are defined as :

$$B_n = b_n \alpha + d_n \ , \tag{2.8}$$

with, and this is important, the same b_n as in 2.7.
Our main goal here is to compute the twist we will add to our wing in order to conserve the bell circulation distribution. We recall that the $\Gamma(\theta)$ distribution is :

$$\Gamma(\theta) = U_\infty b \sum_n B_n sin(n\theta) \ .$$

If we define $B_{n_{bell}}$ the coefficients of our wing without twist and $B_{n_{new}}$ those for the twisted wing, the $\Gamma(\theta)$ conservation can be expressed as :

$$B_{n_{bell}} = B_{n_{new}} \ . \tag{2.9}$$

We will finally have :

$$b_{n_{new}} \alpha_{new} + d_{n_{new}} = b_{n_{bell}} \alpha_{bell} \ . \tag{2.10}$$

We must here emphasize that 2.9 and 2.10 are only valid for the designed incidence, meaning that those expressions will no longer be true as the wing evolve "off-design" (with C_L different from $C_{L_{design}}$). In fact, **the *bell* circulation distribution will only be obtained for the designed lift coefficient** $C_{L_{design}}$ (see Figure 2.10), and thus for only one angle of attack. To maintain this bell circulation distribution for different lift coefficients, the twist would have to be adapted for each situation (*actually, this is what birds achieve when flying*).
Now that all those definitions have been presented, we can proceed to the twist computation method :
For a given geometry (given A_R, b, S and A_0 (for the bell wing)), we must

1. Fix a $C_{L_{design}}$ for which the twist will be set.

2. Compute the angle of attack for the wing without twist α_{bell} with

$$\alpha_{bell} = \frac{C_{L_{design}}}{A_0} \ . \tag{2.11}$$

3. Obtain the $B_{n_{bell}}$ with (2.4) and (2.3).

4. Obtain the $b_{n_{new}}$ (see Appendix (A) and (B) for full detailed procedure).

5. Obtain the geometric angle of attack of the new wing (in fact, both wings will not have the same geometric angle of attack α_{new}, due to the twist we will add to our new wing). This twist is, by definition, equals to zero at the root ($\theta = \frac{\pi}{2}$) of the wing ($\leftrightarrow \alpha_v(\frac{\pi}{2}) = 0$). Introducing that constraint into the compatibility equation leads to:

$$\sum_n B_{n_{new}} sin\left(n\frac{\pi}{2}\right) = \frac{1}{2}a_0\frac{c(\frac{\pi}{2})}{b}\left[\alpha_{new} - \frac{1}{2}\sum_n B_{n_{new}}\left(\frac{sin\left(n\frac{\pi}{2}\right)}{sin\left(\frac{\pi}{2}\right)}\right)\right] \ ,$$

$$\leftrightarrow \underbrace{\sum_n B_{n_{bell}} sin\left(n\frac{\pi}{2}\right)}_{\text{E1}} = \underbrace{\frac{1}{2}a_0\frac{c(\frac{\pi}{2})}{b}}_{\text{E2}}\left[\alpha_{new} - \underbrace{\frac{1}{2}\sum_n B_{n_{bell}}\left(\frac{sin\left(n\frac{\pi}{2}\right)}{sin\left(\frac{\pi}{2}\right)}\right)}_{\text{E3}}\right] \ ,$$

$$\leftrightarrow \alpha_{new} = \frac{E1}{E2} + E3 \ . \tag{2.12}$$

6. With α_{new} found in (2.12), we can derive $d_{n_{new}}$ with

$$d_{new} = b_{n_{bell}}\alpha_{bell} - b_{n_{new}}\alpha_{new} \ , \tag{2.13}$$

and in turn, deduce $B_{n_{new}}$.

7. Finally, we can now easily derive the twist for $\theta = [0; \pi]$ with the compatibility equation :

$$\underbrace{\sum_n B_{n_{new}} sin(n\theta)}_{\text{D1}} = \underbrace{\frac{1}{2}a_0\frac{c(\theta)}{b}}_{\text{D2}}\left[\alpha_{new} + \alpha_v(\theta) - \underbrace{\frac{1}{2}\sum_n B_{n_{new}}\left(\frac{sin(n\theta)}{sin(\theta)}\right)}_{\text{D3}}\right] \ ,$$

$$\leftrightarrow \alpha_v(\theta) = \frac{D1}{D2} + D3 - \alpha_{new} \ . \tag{2.14}$$

2.1.4 Specific geometry choice

We have seen how to compute twist for a specific geometry. But in our case, which geometry best suits our experimental wing ?
We had the choice between a twisted rectangular or a tapered wing :

- A rectangular wing is the most simple wing to design. Its chord is constant along the span and is equal to the ratio $\frac{Wing\ Surface}{Span}$.
- A tapered wing is characterized by its taper ratio $\lambda = \frac{c_{min}}{c_{max}}$. So, the greater the taper ratio, the less tapered the wing will be (see Figure 2.3).

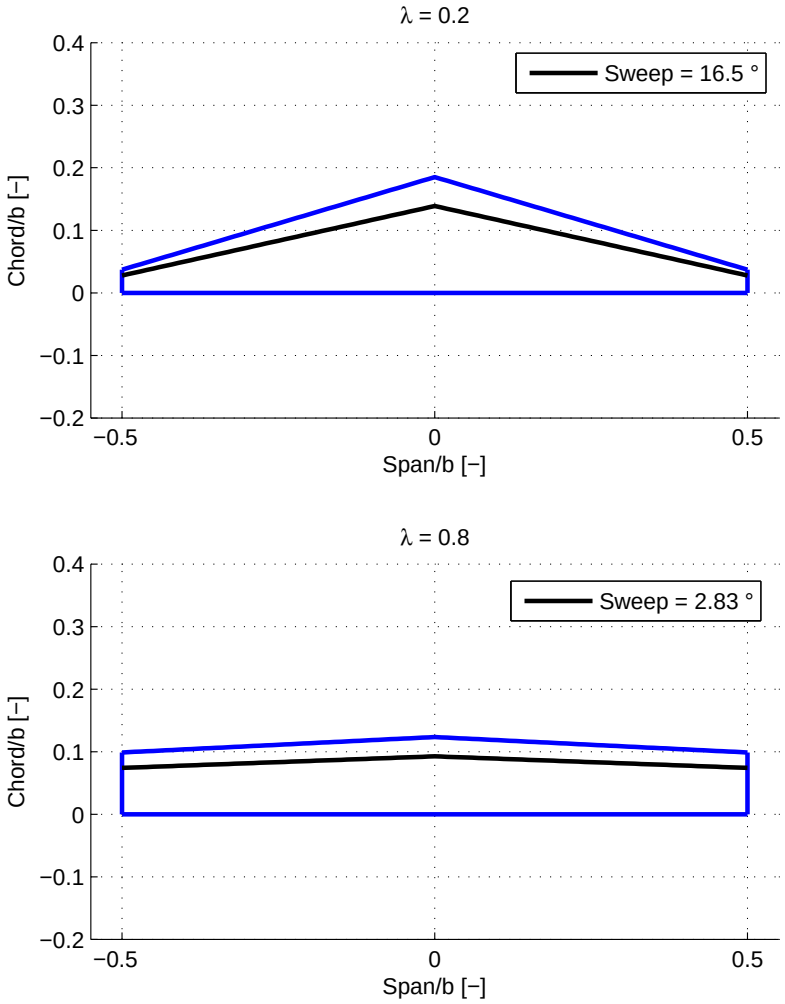

Figure 2.3: Different taper ratios

The sweep angle is by definition the angle of the quarter chord line, along the span (black lines in Figure 2.3). Also, a tapered wing can be shaped so that the sweep angle is zero, so one quarter of the chord is situated ahead of it, and three quarters behind (Figure 2.4).

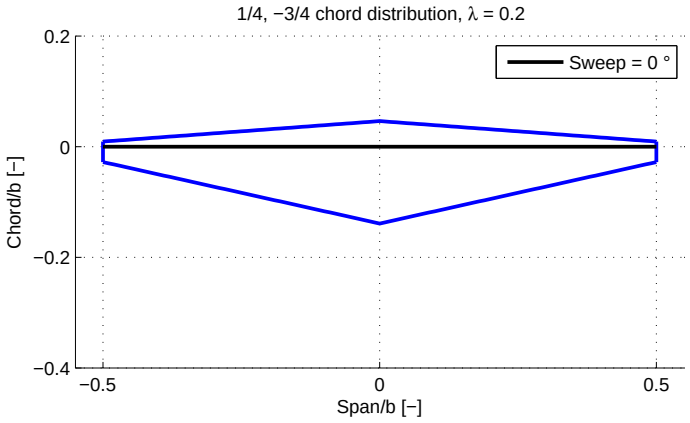

Figure 2.4: No sweep angle, $\lambda = 0.2$

Let us compare the twist computed for a rectangular and a tapered ($\lambda = 0.5$) wing (both with a $C_{L_{design}} = 0.5$, $b = 0.3675$ $[m]$ and $S = 0.015$ $[m^2]$) on Fig. 2.5 :

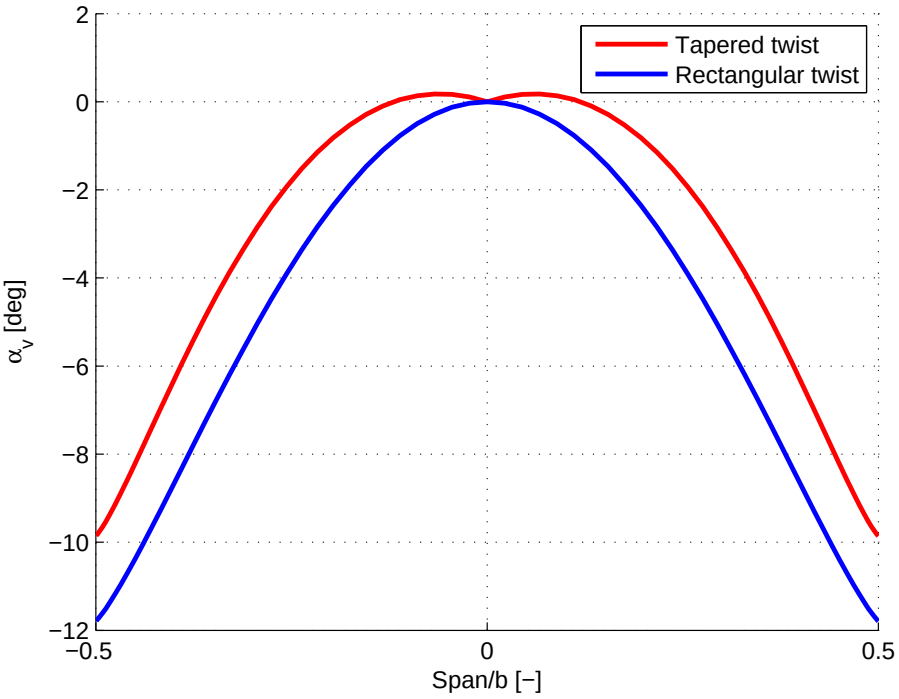

Figure 2.5: Twist computation for rectangular and tapered wings, for $C_{L_{design}} = 0.5$

We immediately see that for the rectangular wing, the twist is almost always 2 degrees greater than for the tapered wing.
However, the parameter which should determine our choice in the geometry is the **distribution of the effective angle of attack** along the span. In fact, the greater this angle will be, the closer to the stall we will get. We thus want to choose the geometry which offers the lowest

effective angle of attack distribution for the given $C_{L_{design}}$. In Figure 2.6, we compare this distribution for the rectangular and tapered wings.

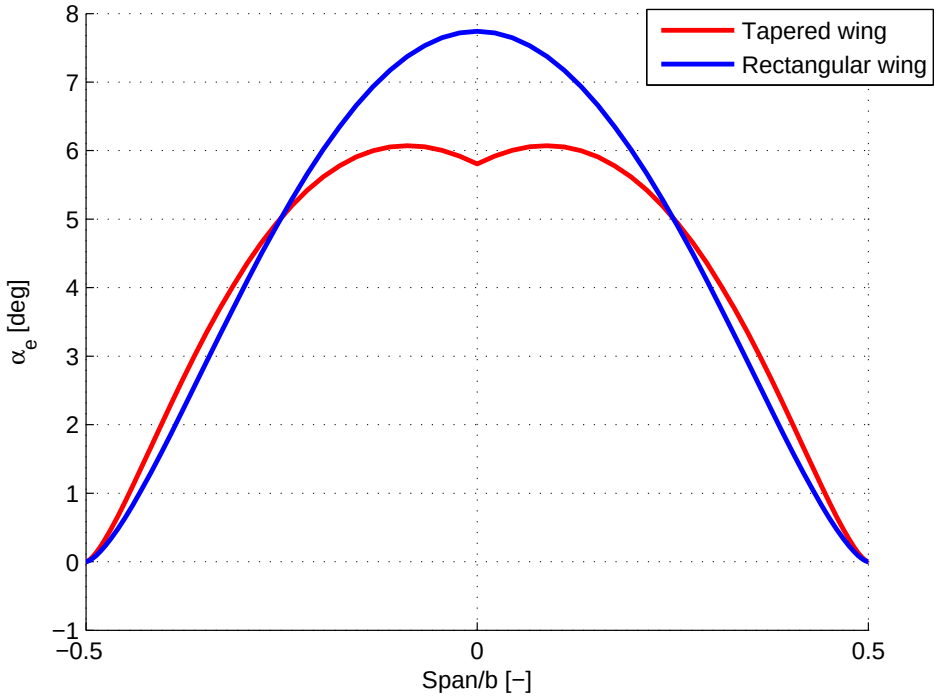

Figure 2.6: Effective angle of attack distributions for different geometry, for $C_{L_{design}} = 0.5$

In Fig. 2.6, we note that for almost half of the wing span, the effective angle of attack distribution of the tapered wing is lower than for the rectangular one. Moreover, at the wing root, this difference is almost of 2 degrees, which is quite significant ! **Our final choice is therefore a wing with a tapered chord distribution.**
Concerning the taper ratio, the value of $\lambda = 0.5$ offers a nice tapered shape (see Figure 2.7), while keeping the wingtips chord not too small. In fact, the lower the chord, the lower the local *Reynold's* number, and the sooner the separation bubble formation occurs, which can lead to drastic reductions in performance [12].
Table 3 contains the principle geometry characteristics :

Taper ratio	λ	0.5 $[-]$
Wing area	S	0.0150 $[m^2]$
Span	b	0.3675 $[m]$
Aspect ratio	A_R	9.0 $[-]$
Mean chord	$\overline{c}$	0.0408 $[m]$
Minimum chord	c_{min}	0.0272 $[m]$
Maximum chord	c_{max}	0.0544 $[m]$

Table 3: Wing's geometry summary

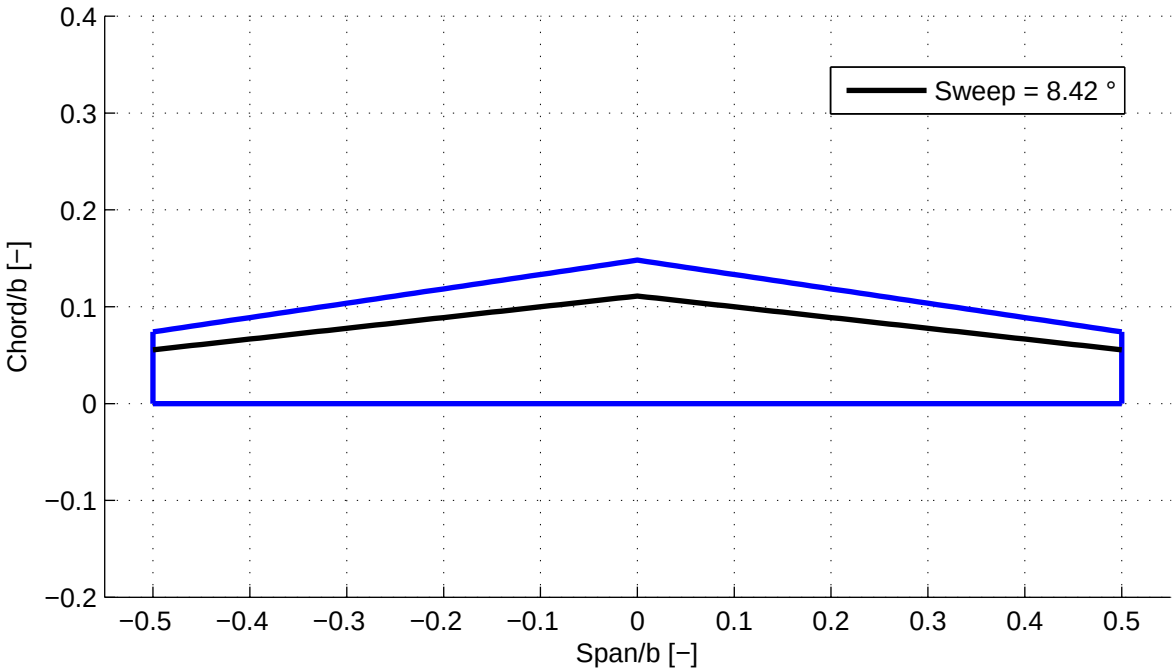

Figure 2.7: Wing final baseline

2.1.5 Specific $C_{L_{design}}$ choice

In the previous paragraphs, we took a $C_{L_{design}}$ equal to 0.5, as this value is often found in common realistic cases. However, during the experimental test campaign, we will not only investigate the "on-design" behaviour of the wing (that means with $C_L = C_{L_{design}}$), but we will also look at the "off-design" situations (with $C_L \neq C_{L_{design}}$). To this end, we do not want the wing to stall when the lift coefficient is just over the designed one (that means : if $C_{L_{design}} = 0.5$, we want the wing still flying at $C_L = 0.6$ and beyond).
Remembering that the profile of the wing will be a *NACA 0012*, we can have a look at the polar of that profile (Figure 2.8) [13]. We see there that for a low *Reynolds number* ($\approx 10^5$), the profile stalls at around 10 degrees.
We can thus fix 10 degrees as the maximum theoretical effective angle of attack until which we will be able to make measurements, before the wing stalls.

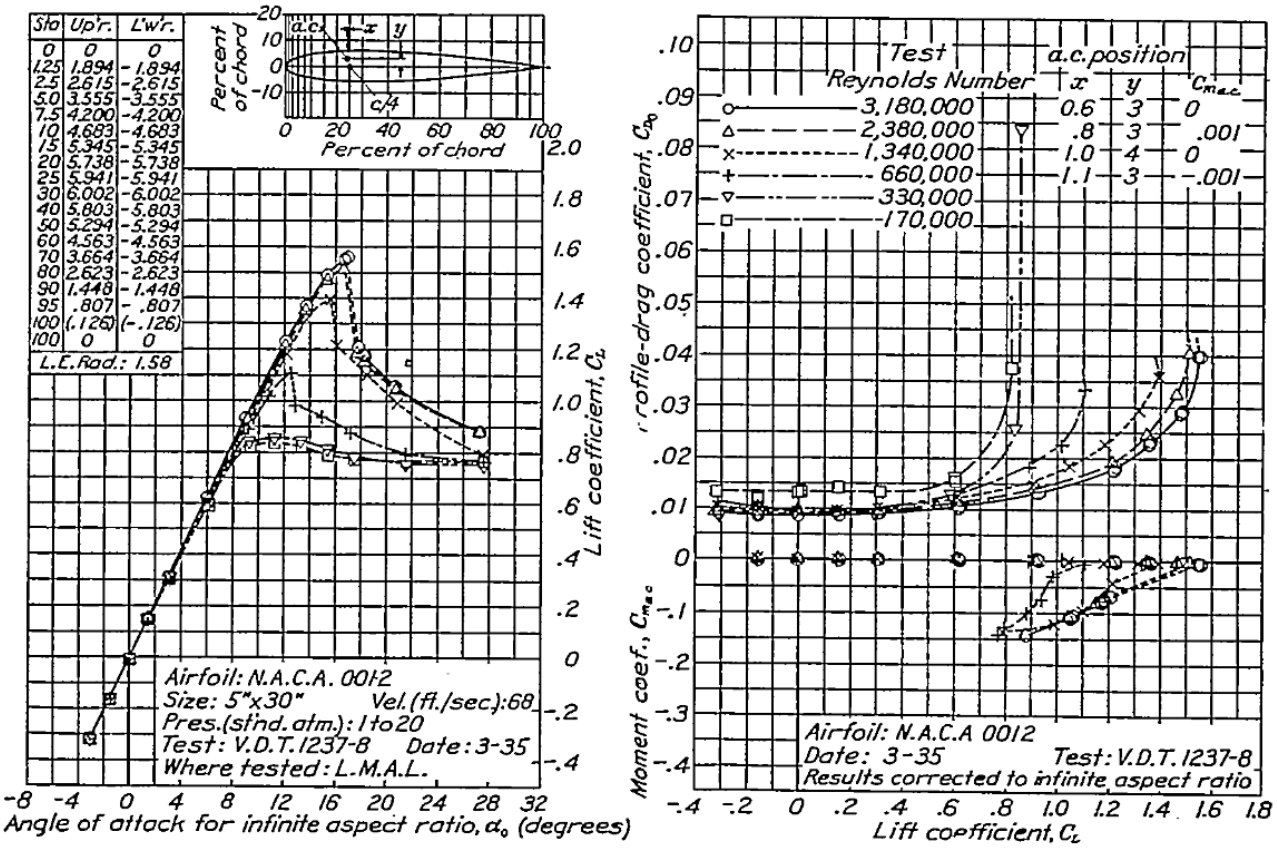

Figure 2.8: *NACA0012* polar. *Source : [13]*

Note : this polar (Figure 2.8) is drawn for an *infinite aspect ratio* wing. Therefore, the geometric angle of attack is the same as the effective angle of attack.

The question is now : which $C_{L_{design}}$ do we have to take ? To answer that question, we can have a look at Fig. 2.9.

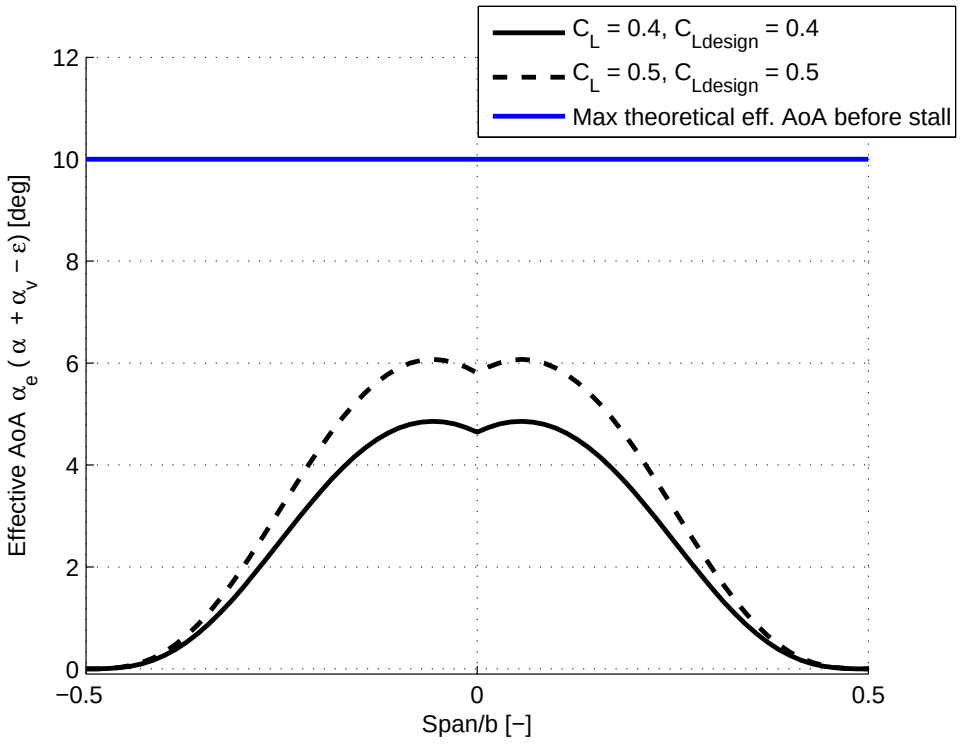

Figure 2.9: Different $C_{L_{design}}$

On this graph, the effective angle of attack distribution is represented by a solid line for the "on-design" case $C_{L_{design}} = 0.4$, and a dashed line for the case $C_{L_{design}} = 0.5$. We can easily observe that with the solid line, we will reach the stall angle (10 degrees) sooner that for the dashed one. Therefore, we would have less data to measure.
Our final choice is then to design a wing with a design lift coefficient $C_{L_{design}} = 0.4$.

2.1.6 *Lift slope* a_0 adjustment

Until now, we took for granted that the lift slope coefficient (a_0) was equal to 2π. Actually, if we take a closer look at the NACA0012 polars (Figure 2.8) [13], we find out that the lift slope of the *NACA 0012* profile is more likely to be $a_0 = 0.92 * (2\pi)$. We will therefore use this value in all our calculations.

2.2 Final baseline

Now that every aspect of the design has been analysed, we can summarise the final characteristics of our *bell wing*, with the different graphs here below.

2.2.1 Theoretical curves

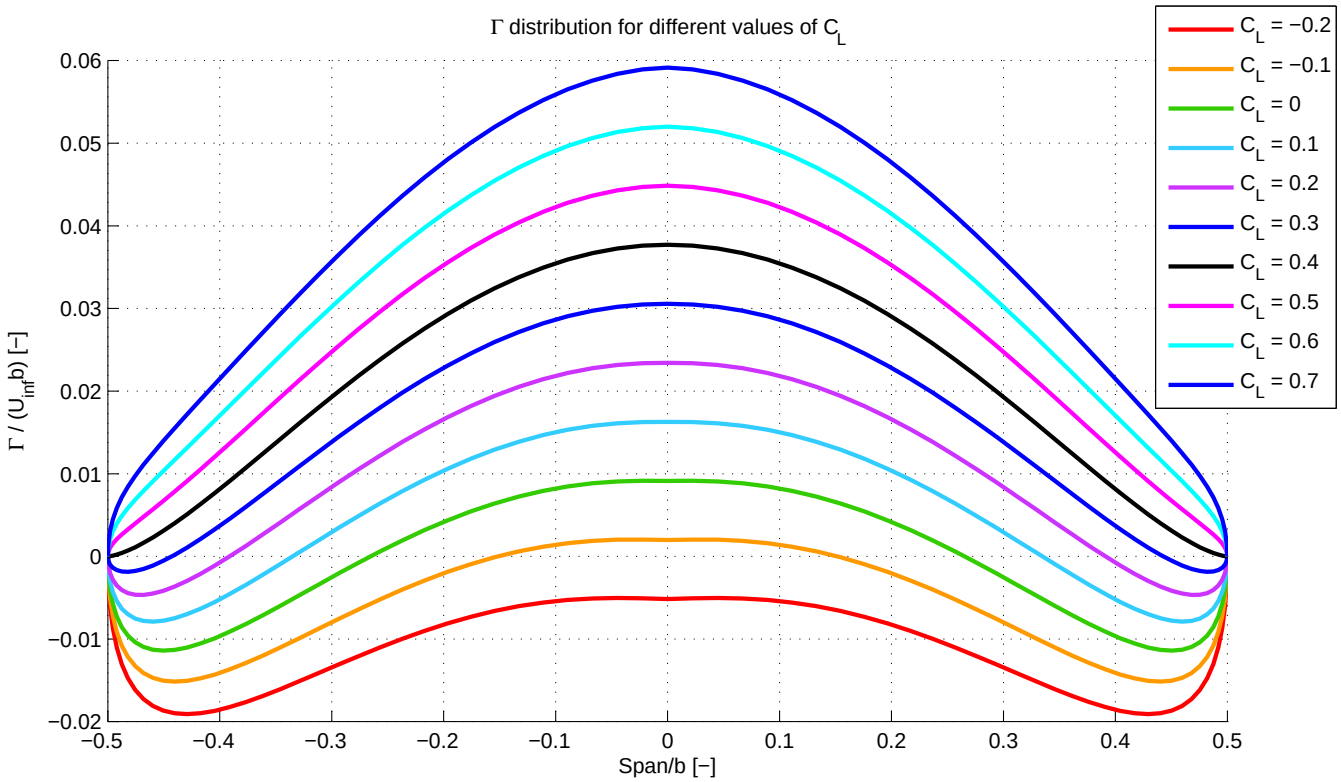

Figure 2.10: Circulation distribution for different lift coefficients

As explained above, the *bell-shaped circulation distribution* is only obtained for the designed lift coefficient (i.e. for $C_{L_{design}} = 0.4$). This is clearly visible in Figure 2.10, as the shape of $\Gamma(y)$ changes significantly with lift coefficients different from the designed one (this is, we recall, because twist was added to the wing: without twist, the bell shape would have been conserved whatever the lift coefficient).

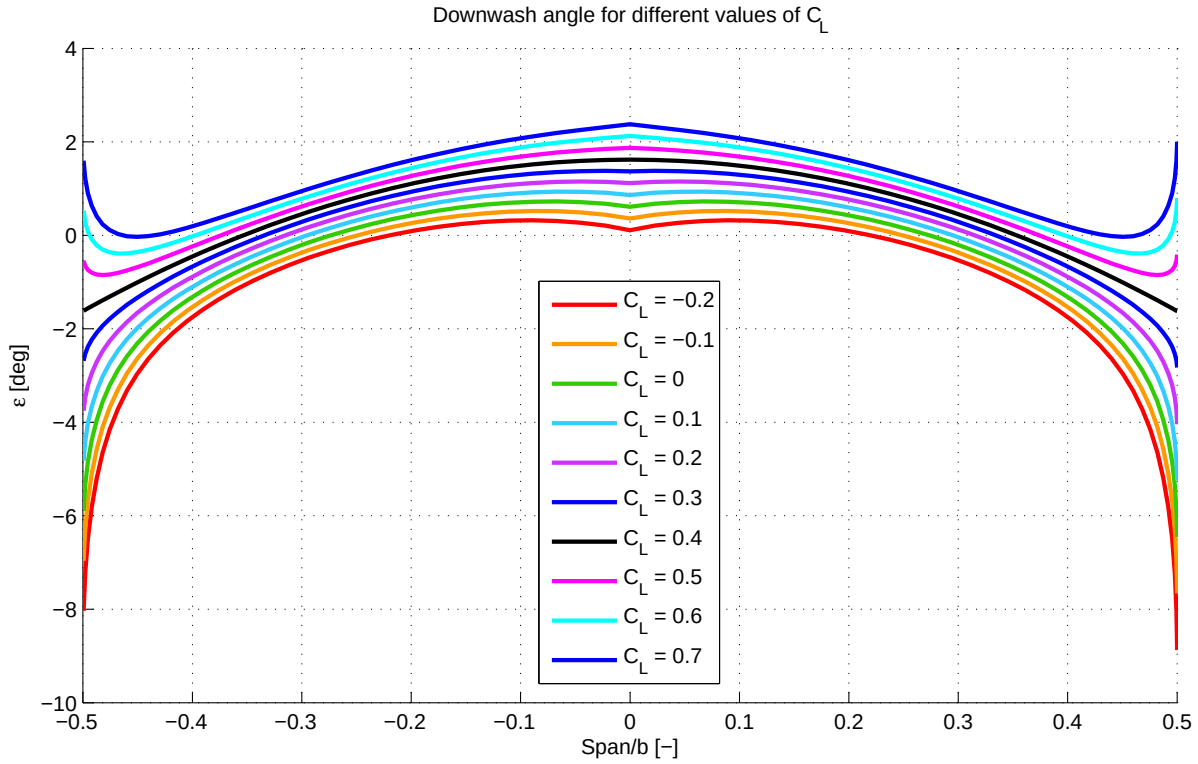

Figure 2.11: Downwash angle distribution for different lift coefficients

For a non-twisted wing, the Prandtl's theory predicts that the downwash velocity would change signs at $y = \frac{b}{2}\frac{1}{\sqrt{2}}$, whatever the lift coefficient. However, as our wing is twisted, this statement is no longer valid and as we see in Figure 2.11, the location where the downwash velocity becomes an upwash velocity moves along the span as C_L changes.
The higher the lift coefficient, the further to the root the sign's change. This will be roughly observed on the PIV results. Before going on to the effective angle of attack distribution, we can take a step back and look at one specific question asked in the introduction section : How do birds achieve sharp turns without a vertical tail ?
To answer that question, we must recall that for an elliptical spanload, the downwash angle is constant along the span and in turn, the local lift is tiled to the back everywhere along the span so that induced drag is omnipresent (see Figure 2.12(a)). Also, recalling its definition, as the lift increases, induced drag also increases. In practice, this can be observed when the ailerons of an aircraft are anti-symmetrically deflected, as the plane will undergo a yawing moment against the intended turn. This phenomenon is called *adverse yaw* [14] and a vertical tail (rudder) is necessary to counteract it [3].
Now, if we look at Figure 2.11, we see that from a certain point on the span, the downwash angle becomes upwash angle. Keeping in mind that the local lift is exerted perpendicularly to the local velocity vector (see section (1.2.1)), it is here tilted into the relative wind, and acts now as a induced thrust (see Figure 2.12(b)). Here, any control surface generating large lift amount would also generate great induced thrust. An aileron would therefore create a yawing moment into the turn, making in turn the vertical tail obsolete (which would result in big drag and weight reductions for modern aircrafts). This phenomenon is called *proverse yaw* [3].
We can now partially answer the asked question, knowing that birds can twist their wings to produce the right amount of proverse yaw, and therefore do not need any vertical tail.

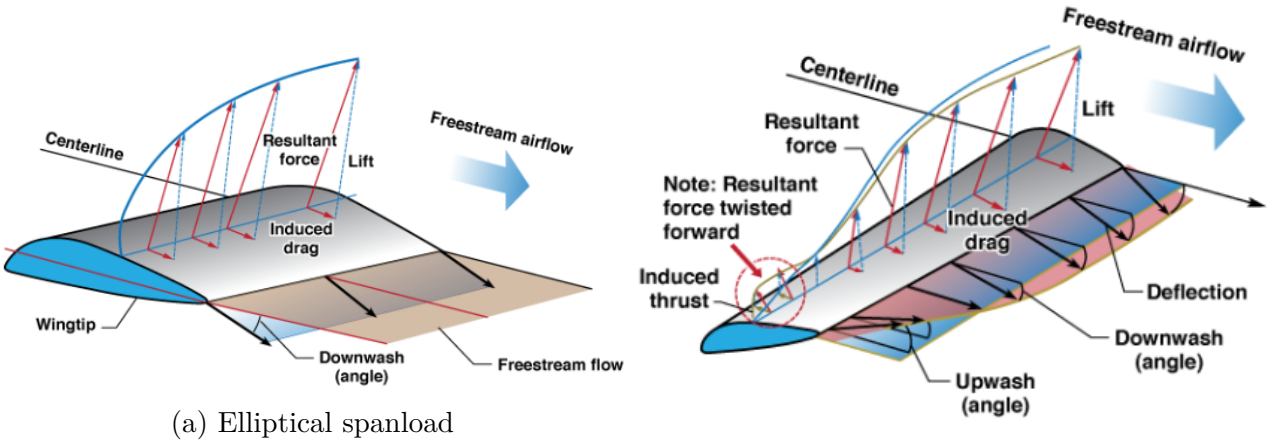

(a) Elliptical spanload

(b) Bell spanload

Figure 2.12: Representation of local forces for different spanloads [3]

Another remark concerning the downwash velocity becoming upwash velocity : the birds benefit from this upwash velocity to optimise their flights, and this is why they can fly in formation with their wingtips overlapped.

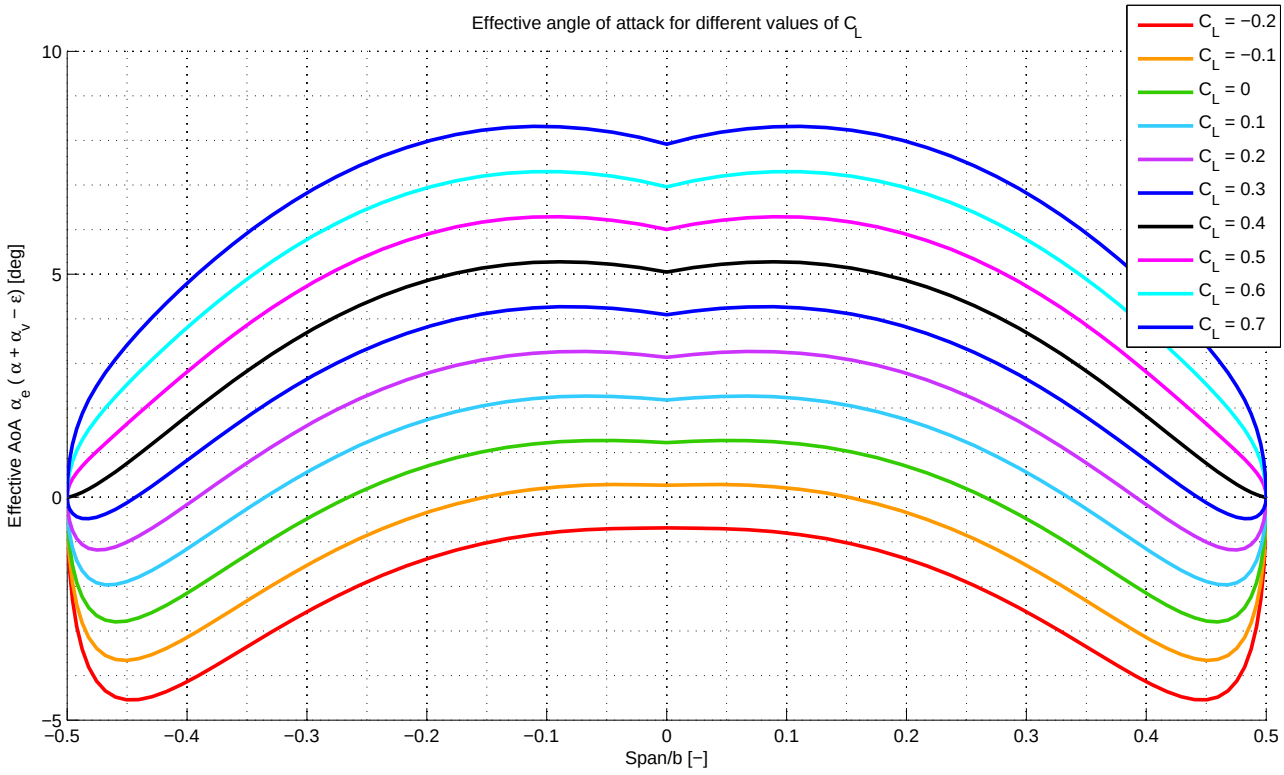

Figure 2.13: Effective angle of attack distribution for different lift coefficients

The effective angle of attack distribution shows a maximum above 8 degrees for $C_L = 0.7$. Considering the viscous effects taking place at low Reynolds numbers (which will be around 10^5 in our case), $C_L = 0.7$ might be the maximum lift coefficient we could study before the

stall of the wing. However, all other lift coefficients shown in Figure 2.13 should be reachable without stalling.

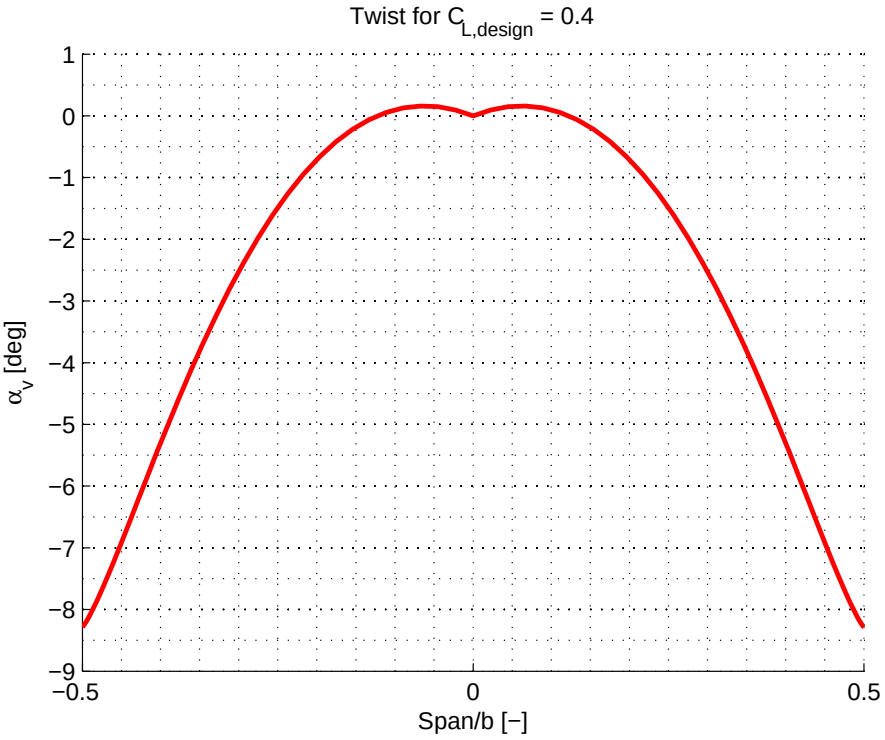

Figure 2.14: Twist distribution for $C_{L_{design}} = 0.4$

2.2.2 Creation of the 3D wing

Having computed the chord distribution (Table 3 and Figure 2.7), the airfoil profile (*NACA 0012*) and the twist distribution (Figure 2.14), the 3D physical wing could be created. We first drew it in *Matlab*, and then exported it into *Solidworks*. As the wing had to be manufactured in two symmetrical pieces, two cylindrical spanwise (*y-axis*) holes were added to embed assembling rods (Figure 2.15).

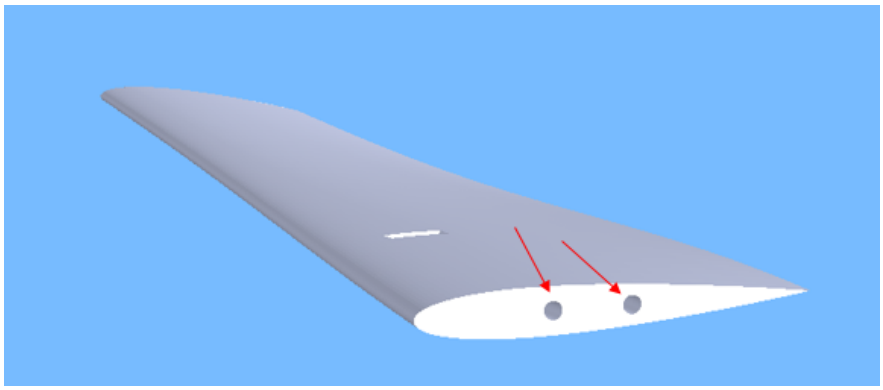

(a) *Solidworks* wing

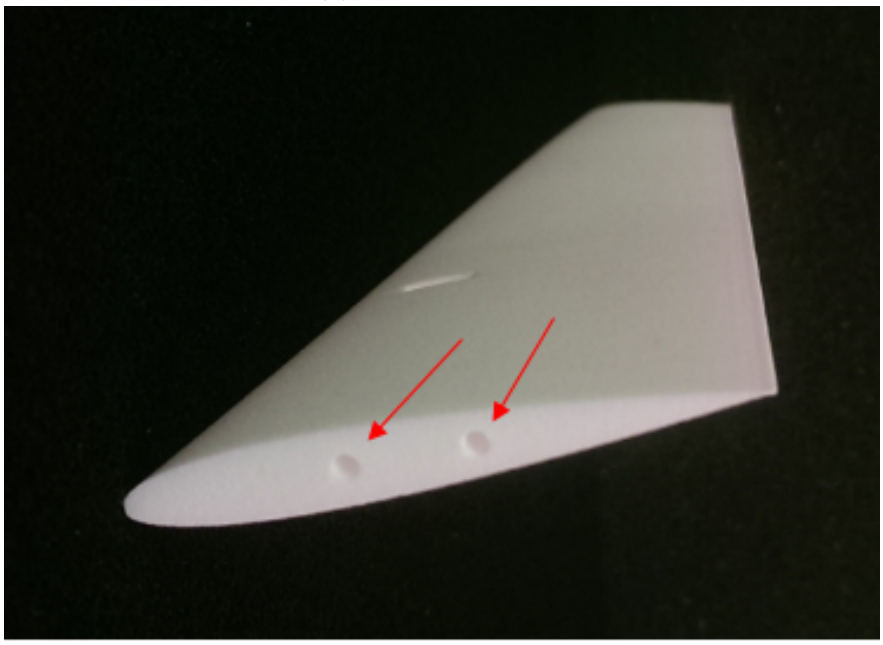

(b) Real wing

Figure 2.15: Holes for assembling rods (half wing)

Two other holes (in the *z-axis*) were made (Figure 2.16) in order to insert the support arms (which will connect the wing to the balance). Those arms were put **on the lower surface of the wing**, so that the air passing on the upper surface remains as laminar as possible, to prevent premature stall.

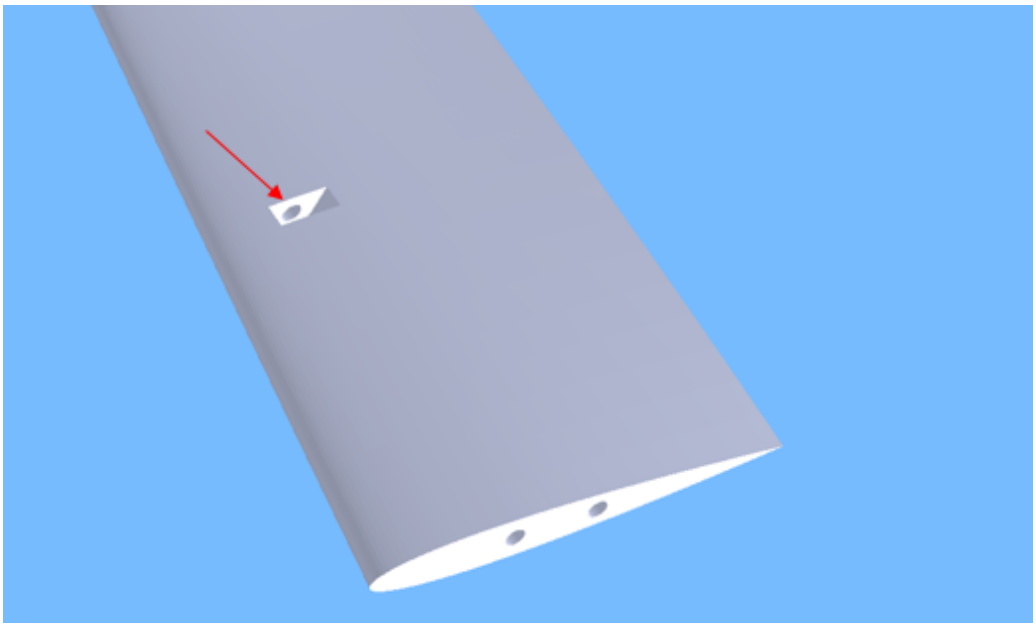

Figure 2.16: Holes for arms (half wing)

Figure 2.17 highlights the twist given to the wing, corresponding to the Figure 2.14.

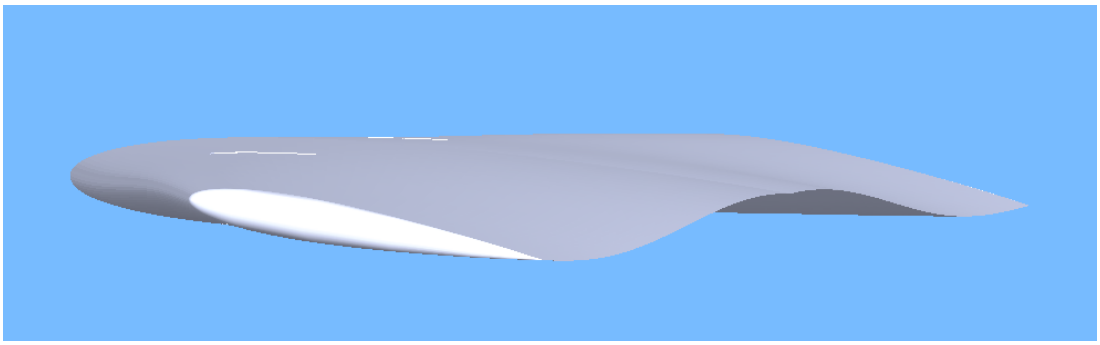

(a) Twist visualisation over the whole *Solidworks* wing

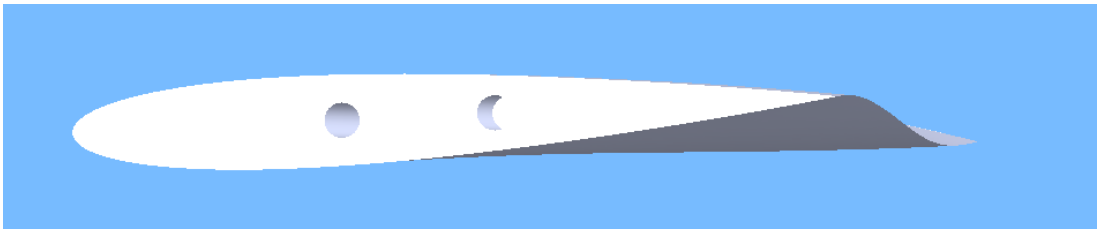

(b) Twist visualisation over half the *Solidworks* wing

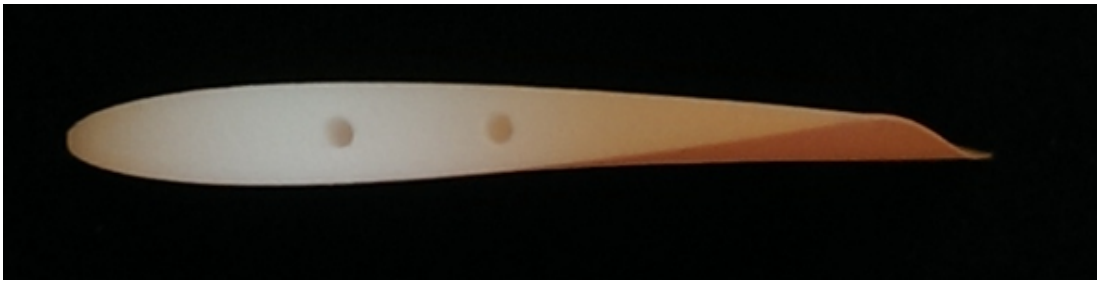

(c) Twist visualisation over half the real wing

Figure 2.17: Twist distribution visualisation

The wingtips were created by rounding the *NACA* profiles situated at $y = -b/2$ and $y = b/2$ around their symmetry axis, as shown in Figure 2.18. This ensures that no shard edge remains at the tips, so that no parasite turbulence (interfering with the wake) is created at the tips.

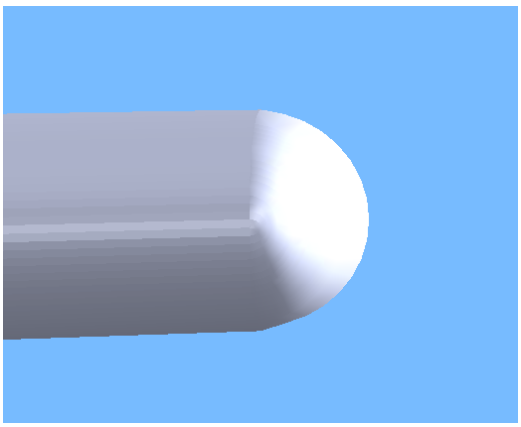

(a) Front view, *Solidworks*

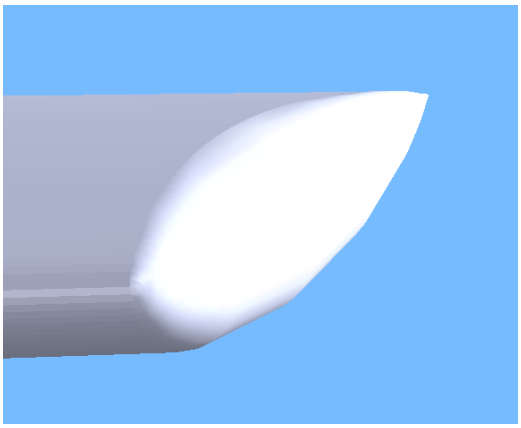

(b) Oblique view, *Solidworks*

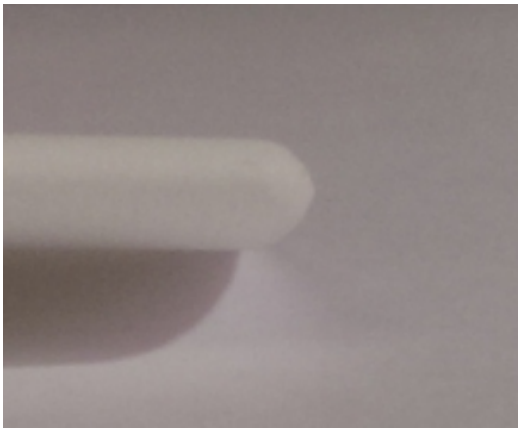

(c) Front view, real wing

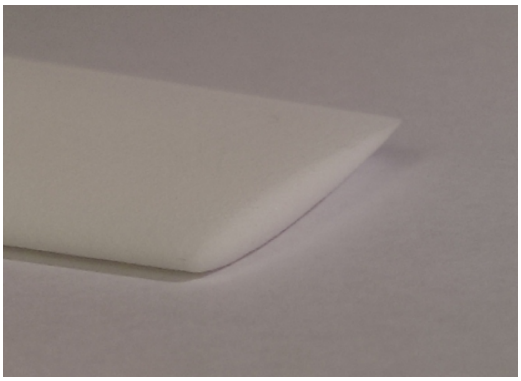

(d) Oblique view, real wing

Figure 2.18: Wingtips visualisation

Finally, Figure 2.19 show the integral wing.

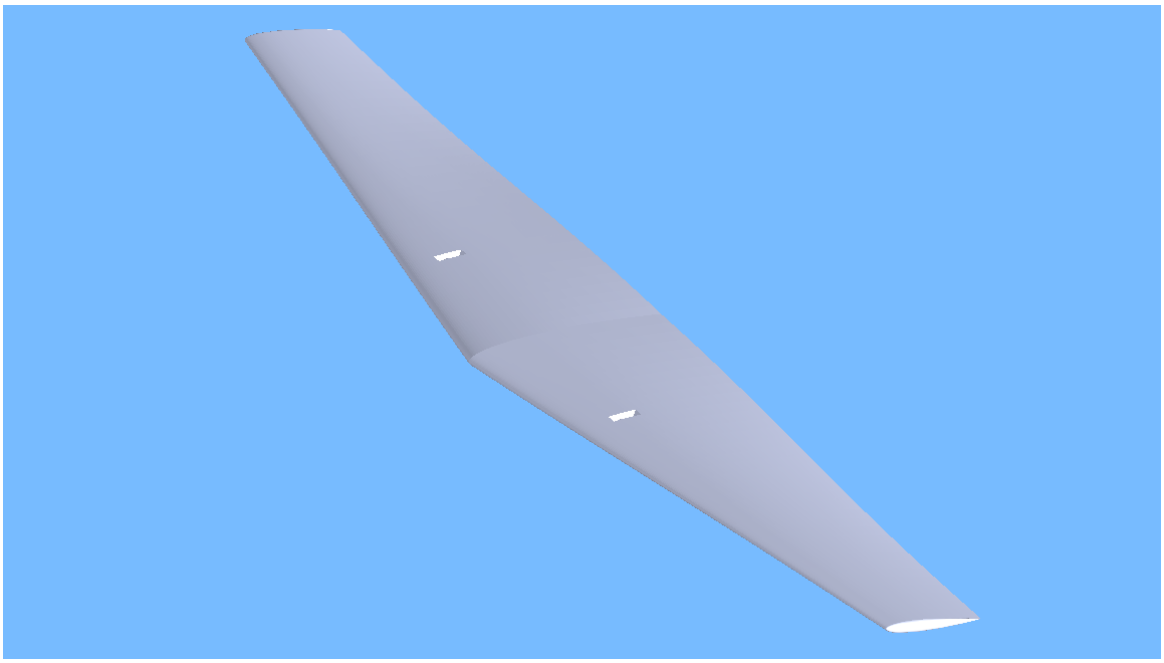

Figure 2.19: Entire *Solidworks* wing

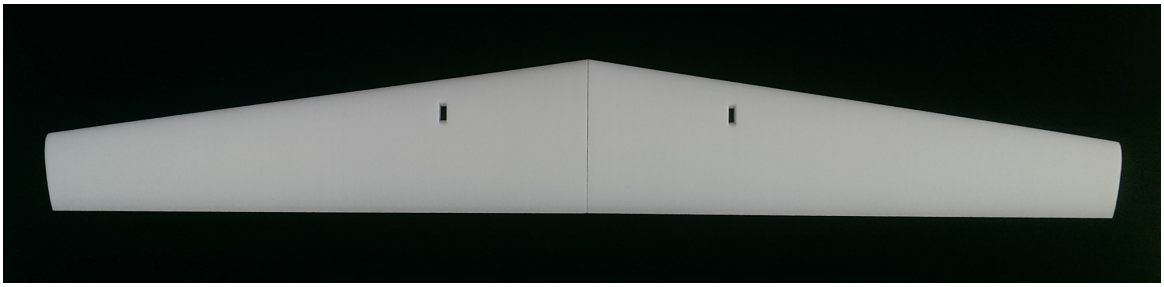

Figure 2.20: Entire real wing

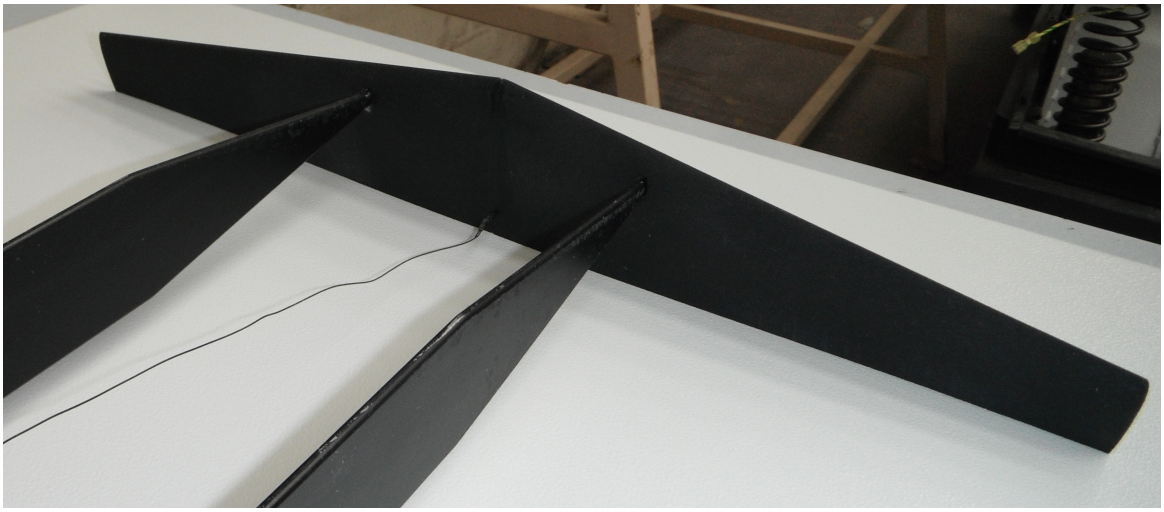

Figure 2.21: Wing painted in black assembled with its support arms

Figure 2.22: Twist visualisation on wing's trailing edge

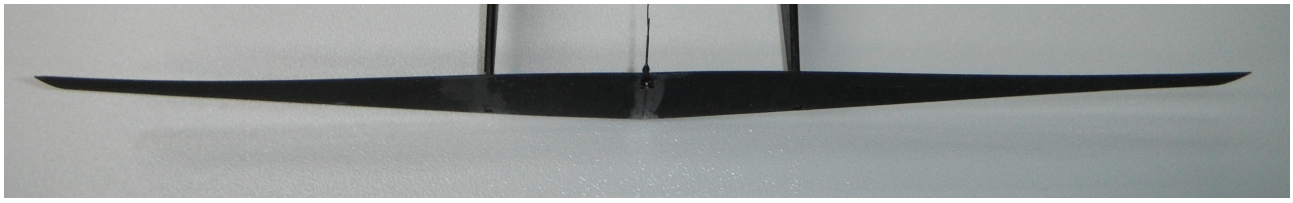

Figure 2.23: Twist visualisation on wing's trailing edge

2.3 Wind tunnel and aerodynamic balance

Wind tunnel

The wind tunnel in which we conducted our experimental campaign is an open circuit wind tunnel. Its convergent section has dimensions of 0.56 x 0.42 $[m]$. The distance between the air inlet and the convergent part is 2.10 $[m]$.

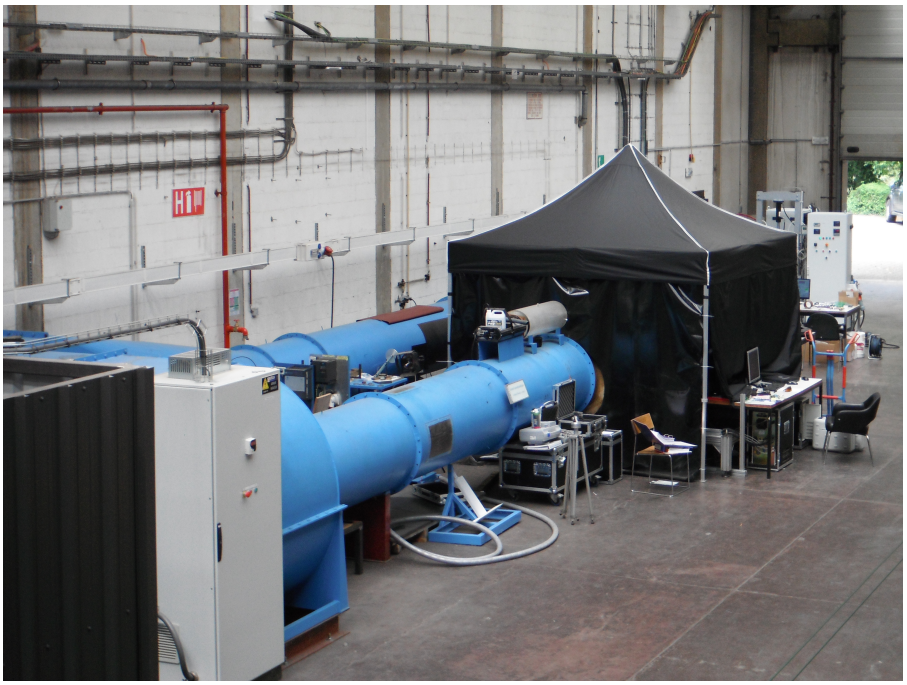

Figure 2.24: An overview of the wind tunnel. The convergent part and the air inlet are in the black tent

(a) Convergent part

(b) Air inlet

Figure 2.25: Convergent part and air inlet of the wind tunnel

Aerodynamic balance

The very first part of our experimental campaign consisted in measuring, with the aerodynamic balance [10], the different forces acting on the wing : lift, drag and aerodynamic moment. As

sketched in Figure 2.26, the wing was connected to the balance with the fixing arms previously mentioned (**B**).

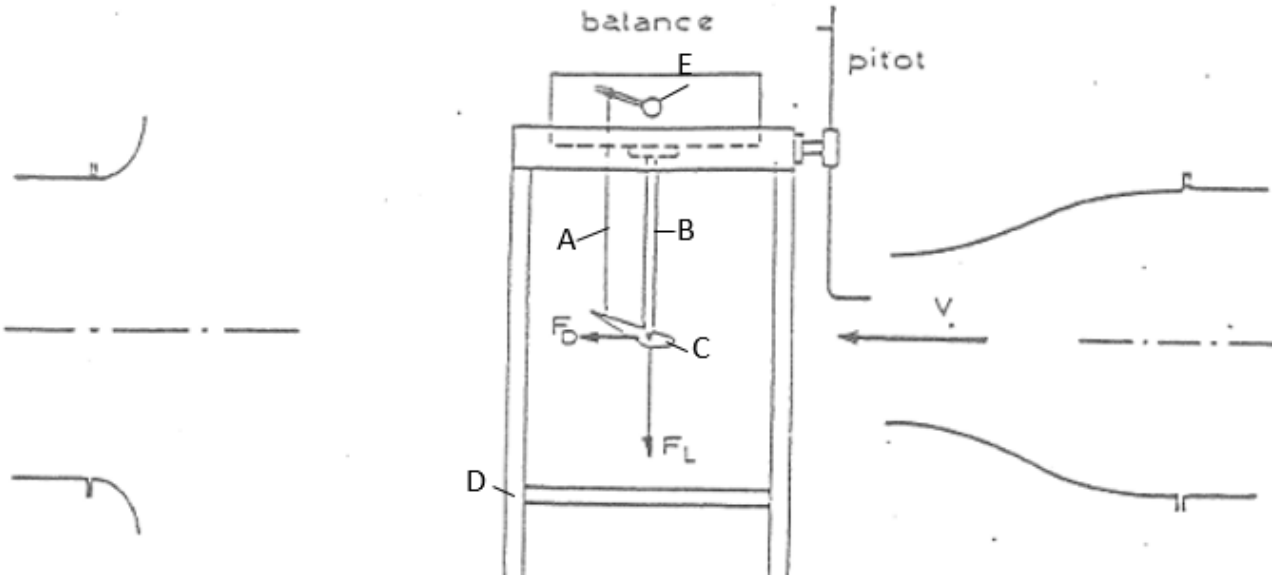

Figure 2.26: Diagram of the aerodynamic balance. **A** : Cable for angle of attack adjustment, **B** : Fixing arms, **C** : Wing, **D** : Balance support, **E** : Protractor for angle of attack adjustment

The balance measures aerodynamic forces exerted on the wing by means of small electrical inductive sensors. Their output signals are directly proportional to the displacement of the mobile parts. Therefore, a calibration of the device had to be done regularly to determine the proportionality coefficients, which vary slightly with the ambient conditions. In our case, in order to keep precise measurements, this calibration was done each week.
Unlike those coefficients, the "zero load values" (i.e. when the wing is not subject to any force except its own weight) had to be noted between each test.

The upstream flow velocity is calculated via a pressure manometer, working with water. This provides information to determine the dynamic pressure, from where we can derive the upstream velocity :

$$P_{dyn} - P_0 = \rho_{water} g h = \frac{1}{2}\rho_0 U_\infty^2 - P_0 \ ,$$

with P_0 the atmospheric pressure, h the height of the water column and ρ_0 the upstream air density, which requires the ambient temperature and pressure values.

2.3.1 Experiment procedure

The lift and drag values were recorded eleven times, from -8 ° to 22 °. As we will see on the polars, the step between two consecutive angles was not equal to 1 °. This was due to the fact that the wing's pitch was adjusted with the balance's protractor, which did not correspond to the actual wing's geometric angle of attack. Therefore, some trigonometrical calculations had to be made in order to obtain our real angles of attack.

The measurements were made 15 minutes after the wind tunnel was turned on. This insured that the flow was stabilised.
Every three polars measurements, the wind tunnel was turned off in order to check or update the zero load values of the balance, before beginning a new test. This insured an optimal precision in measurements.

2.4 PIV setup

The PIV (*Particle Image Velocimetry*) setup is the key of this Masters' thesis, as it is expected to provide very useful information about the wake behaviour. We will here detail all the different equipments and procedures necessary to conduct PIV tests [15].
PIV experiments consist in providing instantaneous velocity vector fields in a cross-section of a flow. To this end, the studied flow is seeded with small particles (typically a few μm of diameter), which we assume do not alter the flow (non-intrusive technique). The displacement of those particles is computed by taking two pictures of the flow (with the help of a strong laser sheet) within a very short time period (a few μs). The pictures are taken by high-speed cameras, capable of stocking large size images very quickly. The velocity (its amplitude and direction) of the particles is then deduced by a specific software. It is important to mention that the use of two cameras allows the software to compute the flow velocity in three dimensions (u, v, w), where only two dimensions velocities (v, w) could be calculated with one camera.

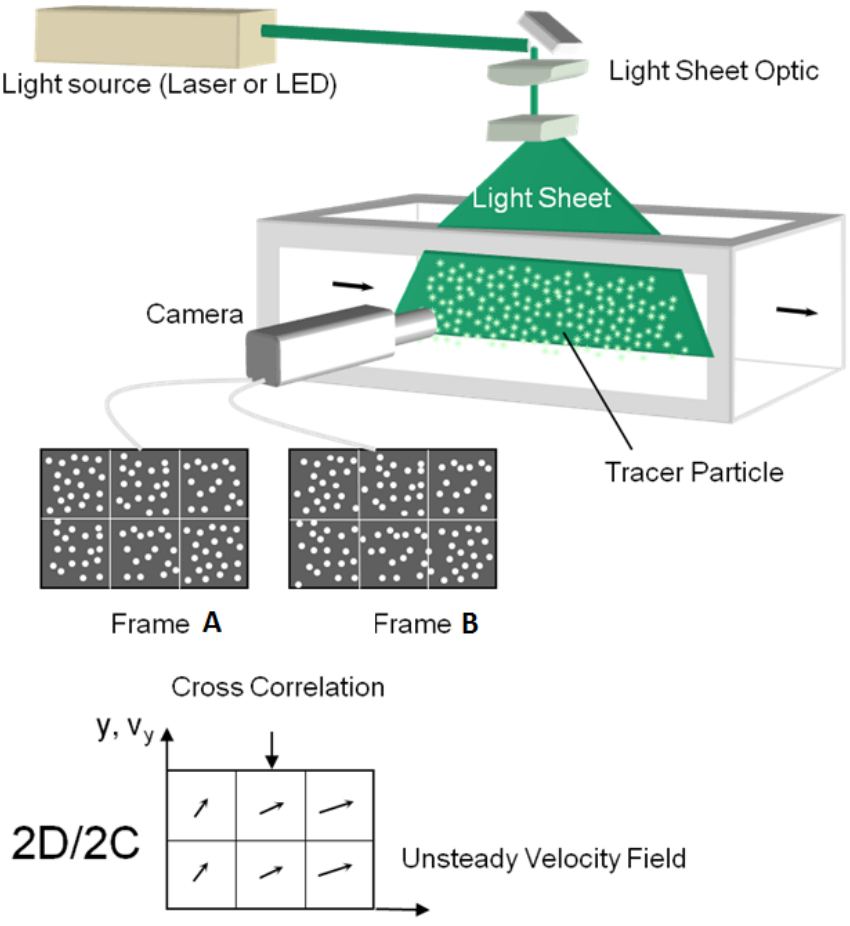

Figure 2.27: Sketch of a PIV setup. *Source : https://www.ila.de*

In order to compute precise vector fields, the software needs workable pictures. Therefore, several essential criteria are to be met :

- High contrast between the particles and the background : as the software recognizes a

particle by the brightness of a group of pixels, a low contrast picture could lead to the omission of particles by the software, resulting in incorrect or incomplete results.

- Good seeding density : the more particles present on the pictures, the more data available across the analysed section.

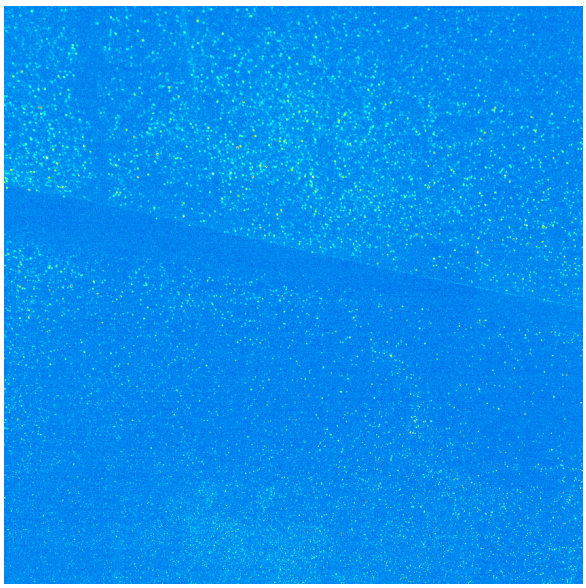

(a) Low seeding density

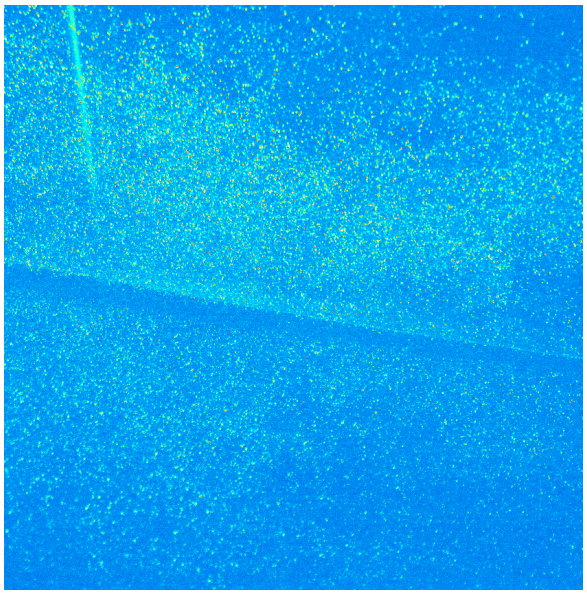

(b) High seeding density

- Good sharpness of pictures : to avoid parasite results, the particles need to be well defined and delimited. Any blurriness could result in incorrect results.
- Correct interval of time (dt) between two pictures capture (see Figure 2.30) : a good dt choice allows particles to move several pixels between two pictures. If the amount of pixels shift is too small, the analysed motion of the particles could be inaccurate. Conversely, if the dt is too large, the motion of some particles could be averaged, resulting in potential distorted results (some curvature of the flow could be missed, for example).
- Correct particle size : a particle is recognized by the software as a small group of bright pixels. If the seeding size is too small (less than a pixel), the software will be incapable of distinguishing the particles, resulting in incorrect or incomplete results.

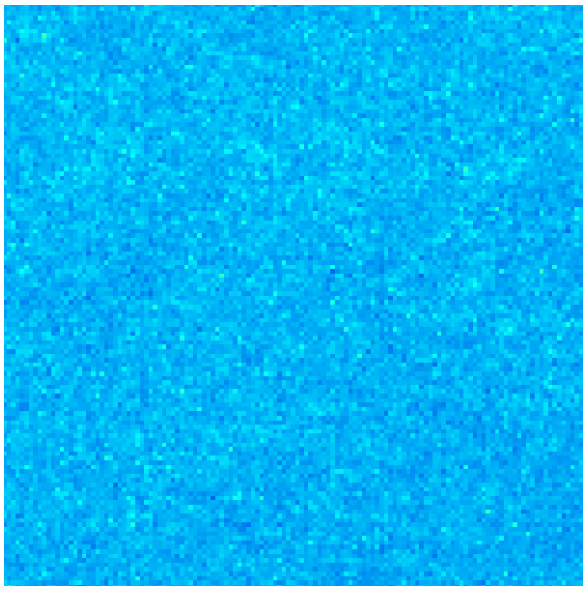

(a) Particles too small (fog particles)

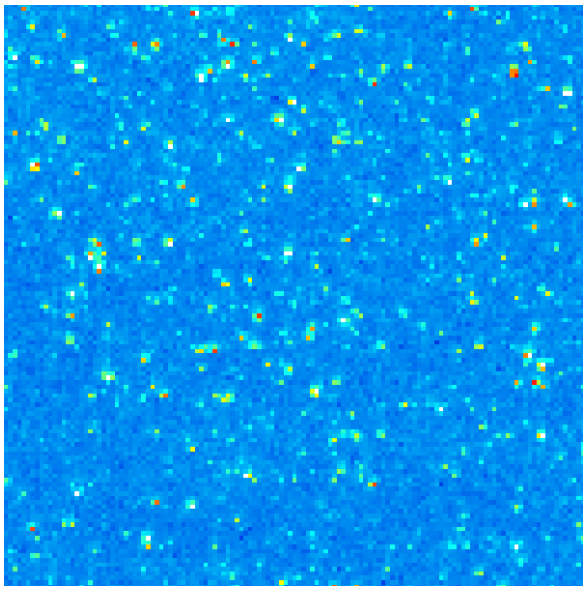

(b) Correct particles size (water droplets)

The n repetition of the two pictures capture forms n frames. The capture of those two pictures is repeated n times (which we then call n *frames*) (see Figure 2.30). Each frame is then processed (creation of vectors from particles displacement), post-processed (elimination of noise, irrelevant vectors, ...) and finally averaged. Obviously, the more frames captured, the more accurate the average will be.

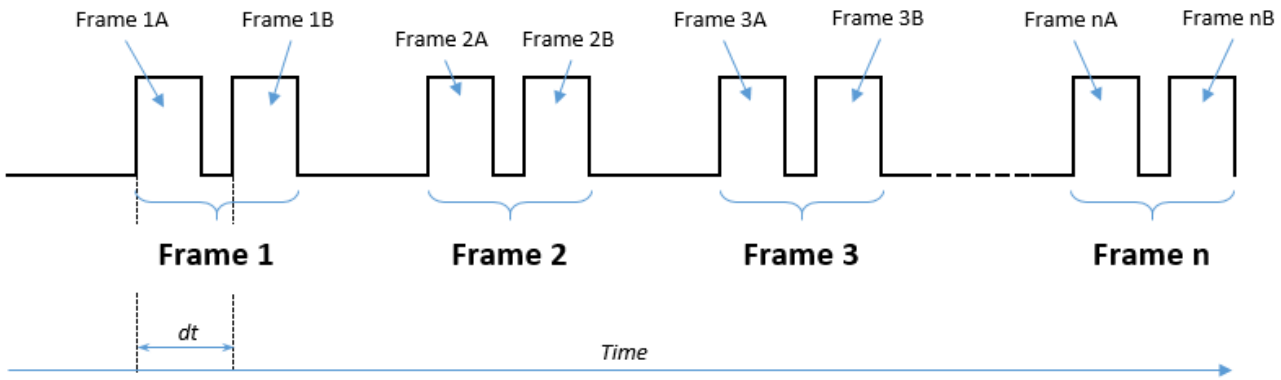

Figure 2.30: Sketch of how the frames capture works

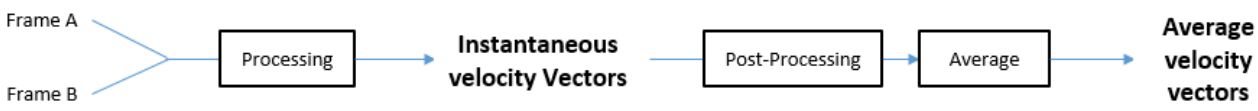

Figure 2.31: PIV processing

2.4.1 PIV equipment

In addition to the equipment listed below, we installed a dark tent to overshadow as much as possible the analysed region (see Figure 2.24). Also, in order to maximise the highlight of the

particles, the wing was painted in black. In fact, the laser beam was too much reflected on the initial color (white) of the wing and therefore altered the results. This goes hand in hand with the different criteria explained in the previous section.

Laser

The laser system is a twin head device, meaning that the main laser head is composed of two independent lasers. Each one is individually controllable.
The laser generator can either be manually controlled or triggered by the computer, so that it lights up at the same time as the cameras.
The output beam needs to be directed to a precise location and in the shape of a sheet. This is possible thanks to an articulated arm (6 degrees of freedom) which redirects the laser beam with a series of mirrors to the desired position.

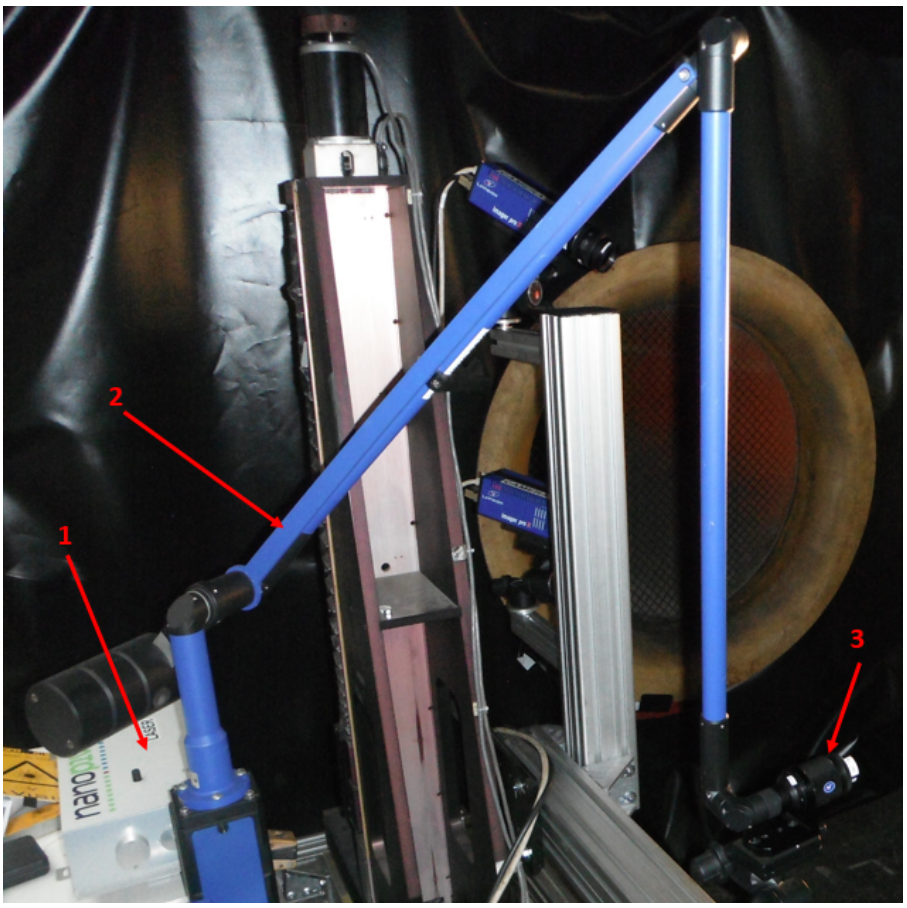

Figure 2.32: Laser system. **1** : Laser generator, **2** : Articulated arm, **3** : Laser optics

At the exit of the articulated arm, an optic device spreads the laser beam into a laser sheet.

Cameras

The cameras we used are high sensitivity and high resolution (1600 x 1200 pixels) digital devices. The minimum interframing time (dt) is equal to 110 $[ns]$, and the frame rate at the maximum resolution is 29 $[frames/s]$.
The cameras could not be directly positioned behind the wing, as they would be in the main

flow and could vibrate. They were therefore placed outside of the main stream, as seen in Figure 2.33. Since, as the objectives of the cameras were not parallel to the analysed flow section, a part of the images would be blurred.

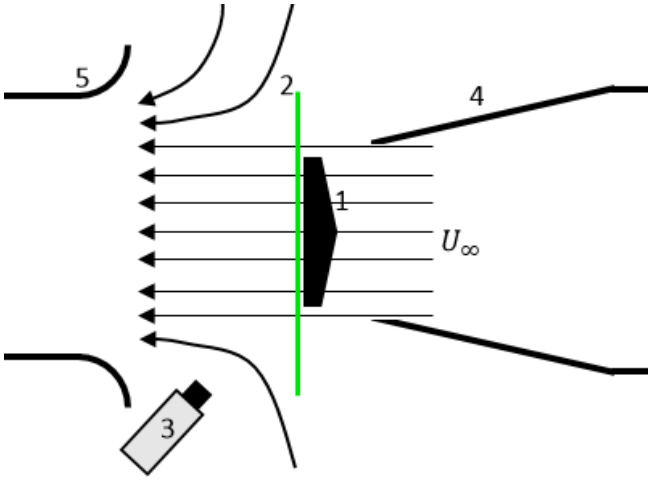

Figure 2.33: Position of the cameras in the working area. **1** : Mounted wing, **2** : Laser sheet, **3** : Camera, **4** : Convergent part of the wind tunnel, **5** : Air inlet

To counteract this problem, a device called *Scheimpflug* (named after the *Scheimpflug principle*) was mounted between the body of camera and its objective (Figure 2.34). This equipment ensures that the whole picture remains clear by putting the camera and its objective out of alignment.

(a) Camera mounted on its Scheimpflug device

(b) Camera body and objective misaligned

Figure 2.34: Scheimpflug device

Seeding device

The seeder is one of the most important devices to set correctly in order to obtain good results. As already explained, the size and the density of particles are crucial. Also, as we are working with an open wind tunnel, some of the main flow (containing the seeding) will exit the tunnel. We therefore need a **non toxic** seeding device capable of producing an important flow

rate of particles.

- **Olive oil**

For most of the PIV experiments, an olive oil atomizer is suggested as the oil is blasted in tiny particles (diameter of 3 [μm]) that do not evaporate quickly. Unfortunately, the *iMMC* does not own such a device. We therefore had to borrow one (Figure 2.35) from the **LaVision** company.

Figure 2.35: Olive oil seeding device

Unfortunately, it turned out that this seeder was ineffective. In fact, its flow rate was way too low for our experiments and the captured frames showed far too few particles.

- **Fog**

The iMMC does however own a fog generator which generates enough flow rate of particles. Unfortunately, this time, the diameter of the particles turned out to be too small (around $30 - 40$ [μm]). As each pixel of the captured frames represents an area of 135 [μm] x 135 [μm], the particles were smaller than the pixels. No result could then be drawn.

- **Gasoline**

We contacted the aerodynamic department of the ULg in the quest to find a seeding device that suited our experiments. They replied that they built their own particle generator, but that it was working with gasoline. For obvious safety reasons (gasoline vapour is highly inflammable and toxic), we could not use such a generator.

- **Water vapour**

Our last solution, which turned out to suit us the most, was to atomize liquid water. The water droplets (around 300 [μm] of diameter) were big enough to appear clearly on pictures. However, this solution had two main issues :

- Water vapour evaporates very quickly. We could then not inject it at the air inlet, as it would be totally evaporated by the time it got to the laser sheet. We had then to inject it straight before the convergent part of the wind tunnel. We thus had to bear in mind that this could create some parasite turbulences ahead of the wing, and potentially pollute the final results.
- As the size of the water droplets was quite important, their mass would be significant too, and the inertia associated to those particles could alter the results.

Note : we also tried this paint sprayer method with olive oil, but in addition to obtain the same results as with water, the wing was rapidly covered with a thick layer oil. We therefore rejected this solution as the most practical one was the paint sprayer fed with water.

2.4.2 Experiment procedure

We will here detail the procedure we followed to get our final results.

- 1. Calibration

The PIV software needs to know where the cameras are with respect to the laser sheet. To this end, we positioned a calibration plate (Figure 2.36) in the plane of the laser sheet. The cameras were then calibrated with the help of the little white dots painted on this plate. It is important during that phase to be the as precise and meticulous as possible, as all the results will depend on this calibration.

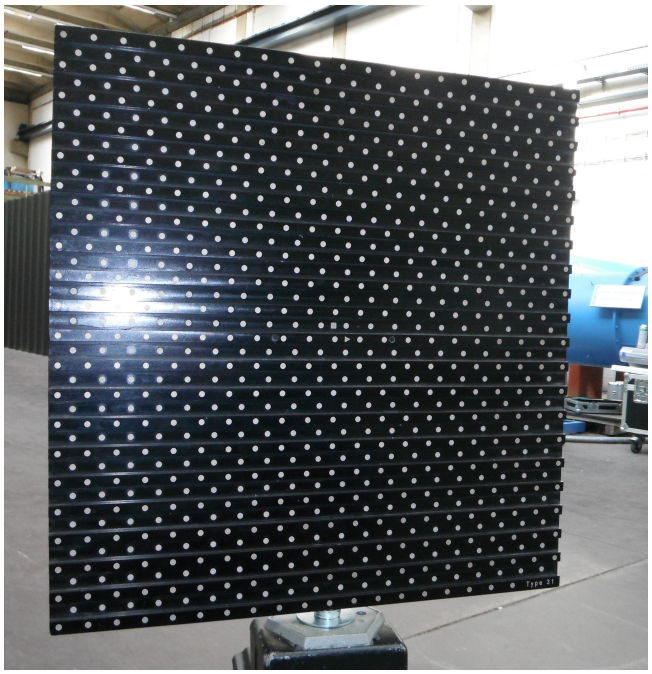

Figure 2.36: Calibration plate

The whole process takes quite a long time : around 30 minutes. As the intended goal of the PIV experiments was to analyse the wake at different distances behind the trailing edge of the wind, this calibration had to be repeated quite often, taking in total a significant time, with the risk of being inaccurate during those calibrations. We then came up with the solution to mount both the cameras and the laser optic on the same table. This table could translate into the x and z axis. Therefore, one and only one calibration had to be done, since all devices would move together (see Figure 2.37).

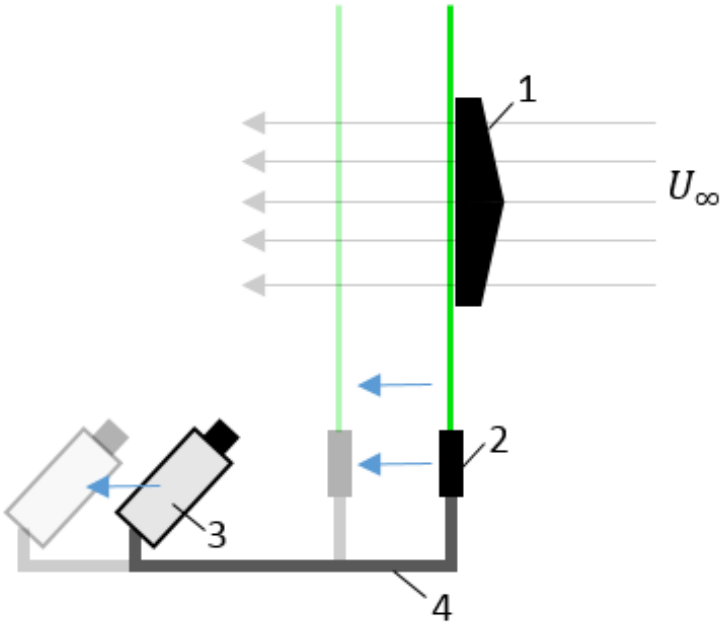

(a) Sketch of the translation table's functioning

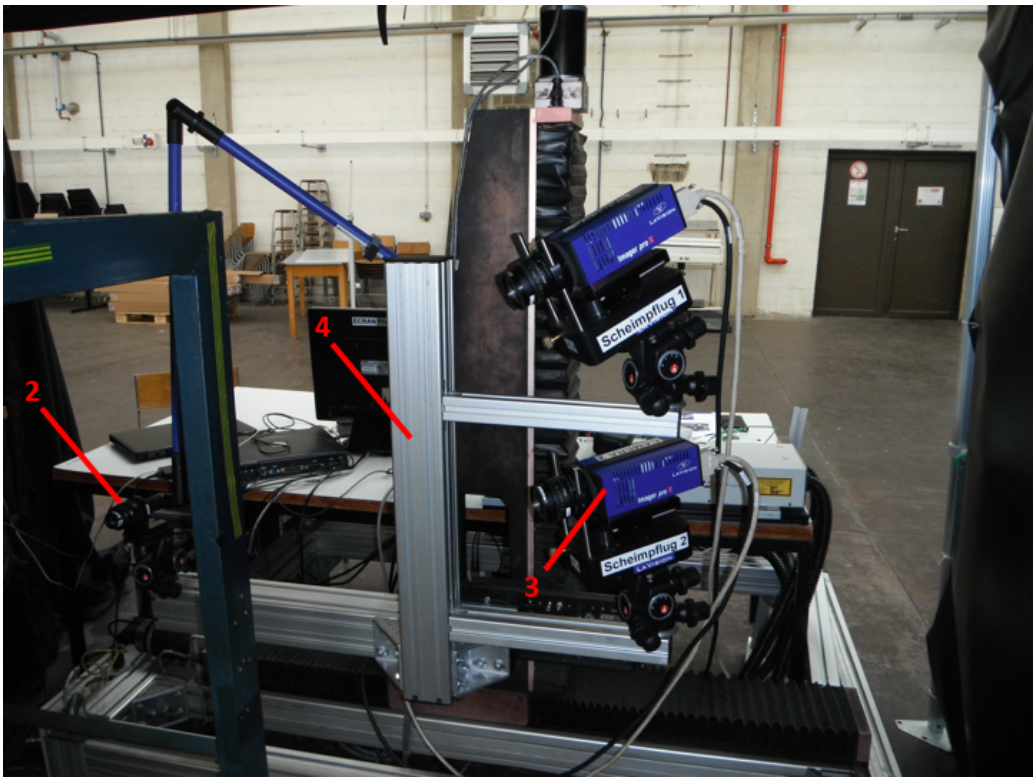

(b) Actual translation table

Figure 2.37: The cameras and the laser optic are mounted on the same moving support. In dark : position A, in bright : position B (initial position moved to the left). - **1** : Wing, **2** : Laser optic, **3** : Cameras, **4** : Moving support

- 2. Capture of images

Once the whole system was calibrated, the dark tent was closed as much as possible (any reflection of light on the ground had to be removed). The goal during the frames capture is to have the least light possible in the tent, so that the background of the images is the darkest possible, and the particles are therefore well highlighted.
The wind tunnel was then turned on. After around 15 minutes (the time for the flow to stabilize), the wing was positioned at the correct angle of attack (depending on the lift coefficient wanted), with the help of the aerodynamic balance.
Finally, the flow was seeded and the pictures taken. In order to have good results, at least 400 frames were taken per test.

- 3. Frames processing

Once the frames captured, the software processed them, converting the particles displacements into velocity vectors. This operation could take up to 36 hours.

- 4. Post-processing

Sometimes,the particles displacements are not correctly identified and the software interpolates their movements, resulting in incoherent results. The goal of the post-processing was to get rid of all those illogical results. The parameters for this operation were quite straightforward : any velocity vector out of a certain predefined range had to be eliminated.

- 5. Averaging of the velocity vector fields

Once all frames were post-processed, the PIV software averaged all the velocity vectors. Here, the number of frames taken makes sense : the more images, the better the average.

3 Experimental results and analysis

In this section, we will present all the results we obtained during the experimental campaign. They are divided into two distinct parts : the first one will concern the general aerodynamic characteristics (lift, drag, ...) of the wing, computed with the help of the aerodynamic balance. They will be compared to the theoretical polars derived from the Prandtl's lifting line theory. The second part of the results will be dedicated to the PIV results. Again, a parallel will be established between the Prandtl's wing theory (section (1.2.3)) and those results.
An important remark to make before presenting the results is that all the theories presented in the previous sections are just an attempt to explain the reality. The Prandtl's lifting line theory is an extraordinarily easy tool, but it should therefore be expected that the results somehow diverge from the theoretical curves. Our task will be to quantify and review this divergence.

3.1 Aerodynamic characteristics

As a quick reminder, we defined the lift and the drag coefficients as :

$$C_L = \frac{L}{qS} \ , \tag{3.1}$$

$$C_D = \frac{D}{qS} \ , \tag{3.2}$$

with $q = \frac{1}{2}\rho U_\infty^2$ the dynamic pressure and S the wing area.
For the following curves, each value corresponding to a specific angle was recorded eleven times, on three different days. The ambient temperature and pressure were thus different at each test, as well as the zero load values of the balance. This insured a good diversity in ambient conditions, resulting in more reliable results.
No data was recorded for the aerodynamic moment, as the friction between the wing and its support arms altered the values. However, for small angles of attack (low tension in the angle of attack adjusting wire), the aerodynamic moment value remained constant. This made sense since the support arms were placed at one quarter of the airfoil chord. This location is the theoretical aerodynamic centre, where the aerodynamic moment value remains constant, regardless of the angle of attack [4].
All our experiments were made at a Reynolds number relative to the root of the wing so that $Re_r \approx 10^5$.

3.1.1 Lift

If we recall the compatibility equation, the B_n coefficients are defined as $B_n = b_n\alpha + d_n$. In order to compute our theoretical lift curve, we must calculate those b_n and d_n coefficients (see Appendix (B) for detailed resolution). We can then use the Eq. (1.32) and determine our lift curve :

$$\begin{aligned} C_L &= \frac{\pi}{2} A_R \ B_1 \ , \\ &= \frac{\pi}{2} A_R \ (b_1\alpha + d_1) \ , \\ \rightarrow \alpha &= \frac{\left(\frac{2C_L}{\pi A_R} - d_1\right)}{b_1} \ . \end{aligned} \tag{3.3}$$

With the relation 3.3, we can deduce the lift slope for the whole wing, (for moderate angles of attack) : $A_0 = 4.74$.
Another method to determine A_0 is to use *Helmbold*'s equation [4] (valid for wings with moderate aspect ratio) :

$$A_0 = \frac{dC_L}{d\alpha} = \frac{A_R}{\left(\sqrt{A_R^2 + 4} + 2\right)} a_0 \ . \tag{3.4}$$

Therefore, with an aspect ratio equal to $A_R = 9.0$ and $a_0 = 0.92 * (2\pi)$ (see section (2.1.6)), the *Helmbold*'s equation gives $A_0 = 4.63$.
Here below are the experimental lift curves :

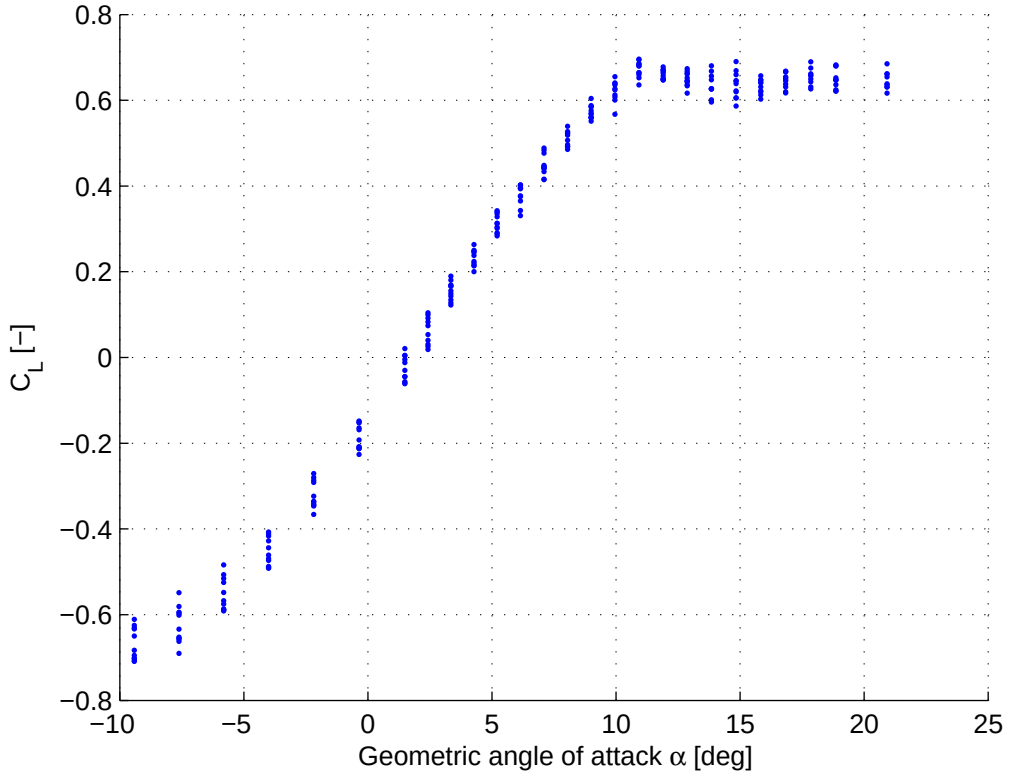

Figure 3.1: Lift coefficients C_L against geometric angle of attack α, $Re_r \approx 10^5$

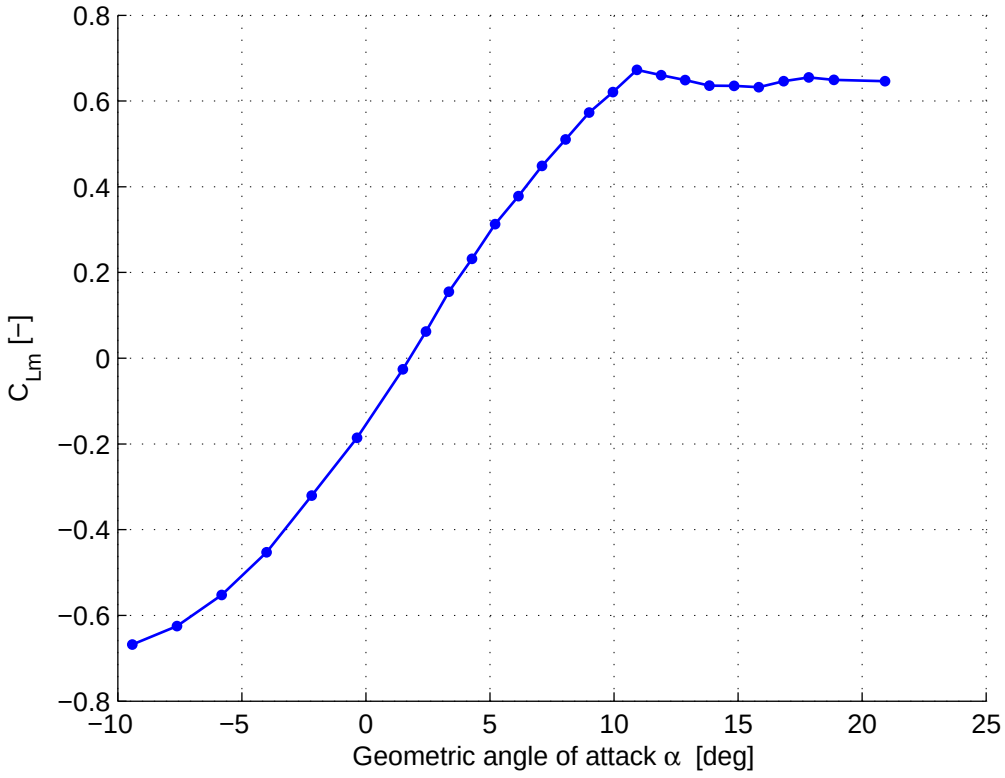

Figure 3.2: Mean lift coefficients C_{L_m} against geometric angle of attack α, $Re_r \approx 10^5$

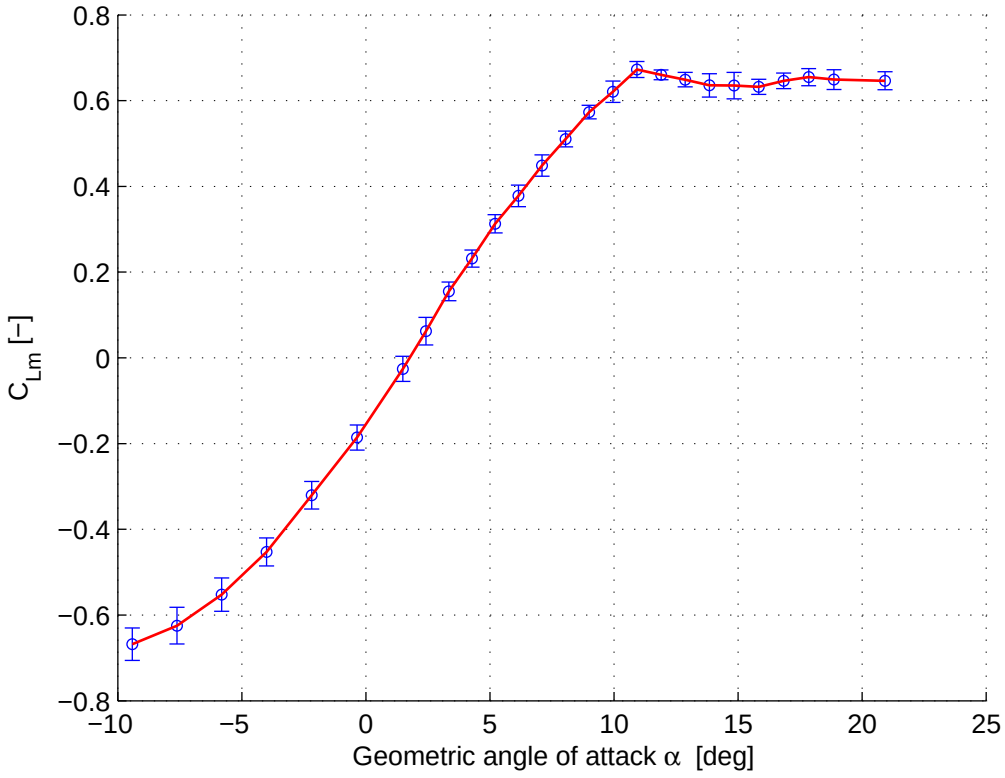

Figure 3.3: Standard deviation associated to the mean lift coefficients against angle of attack α, $Re_r \approx 10^5$

Some remarks about the above graphs :

- The maximum mean lift coefficient is $C_{L_{m,max}} = 0.672$, which is quite high, considering the low Reynolds number at which the experiment is taking place.

- We see in Figure 3.3 that our measurements are quite reliable, as the standard deviation does not exceed 0.025 for most of the angles, which corresponds to an error of approximately 4% for $C_L = 0.6$.

- The experimental lift slope A_0, for a lift coefficient range $C_L = [-0.4 \ : \ 0.4]$ is $A_0 = 4.78$. This result is extremely encouraging, if we recall the theoretical values :

Method	$\frac{dC_L}{d\alpha}$ $[-]$
C_L definition (Eq. 3.3)	4.74
Helmbold	4.63
Experimental	**4.78**

Table 4: Lift slope values summary

The following graph shows the experimental lift curve along with the theoretical one computed with $a_0 = 0.92 * (2\pi)$ (in blue) and $a_0 = 2\pi$ (in green).

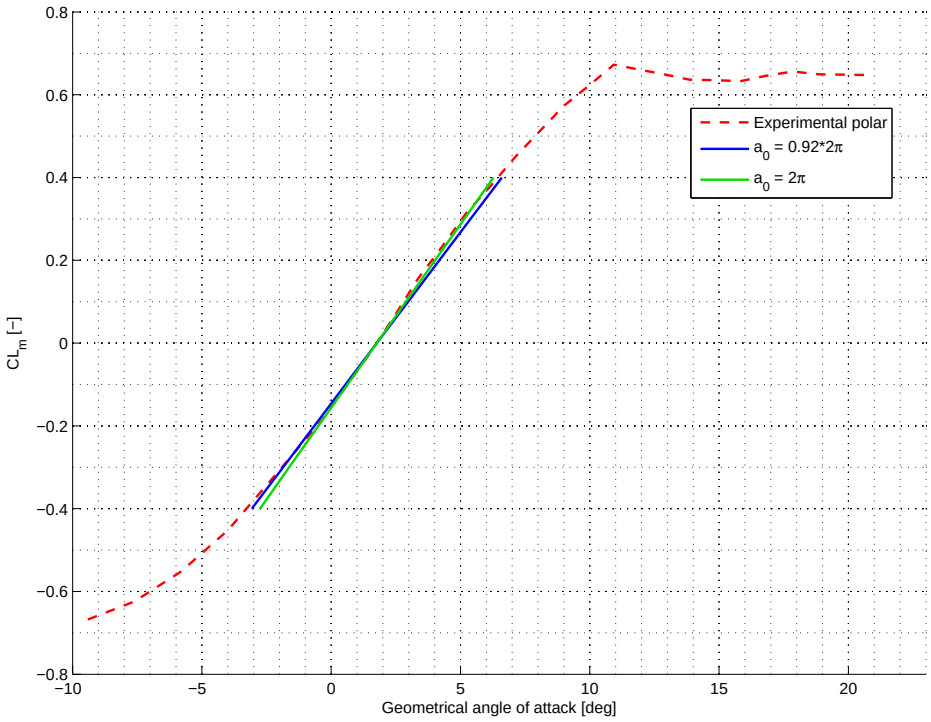

Figure 3.4: Experimental and theoretical lift polars, with different values of a_0

We can also see that for a range of lift coefficients ($C_L = [-0.4 \ : \ 0.4]$), the polar with $a_0 = 0.92 * (2\pi)$ is the closest to the experimental one. However, if we look at the zero lift value

($C_L = 0$), it appears that the lift slope is greater than the theoretical one with $a_0 = 2\pi$ (see Figure 3.5 for a zoom of the zone).

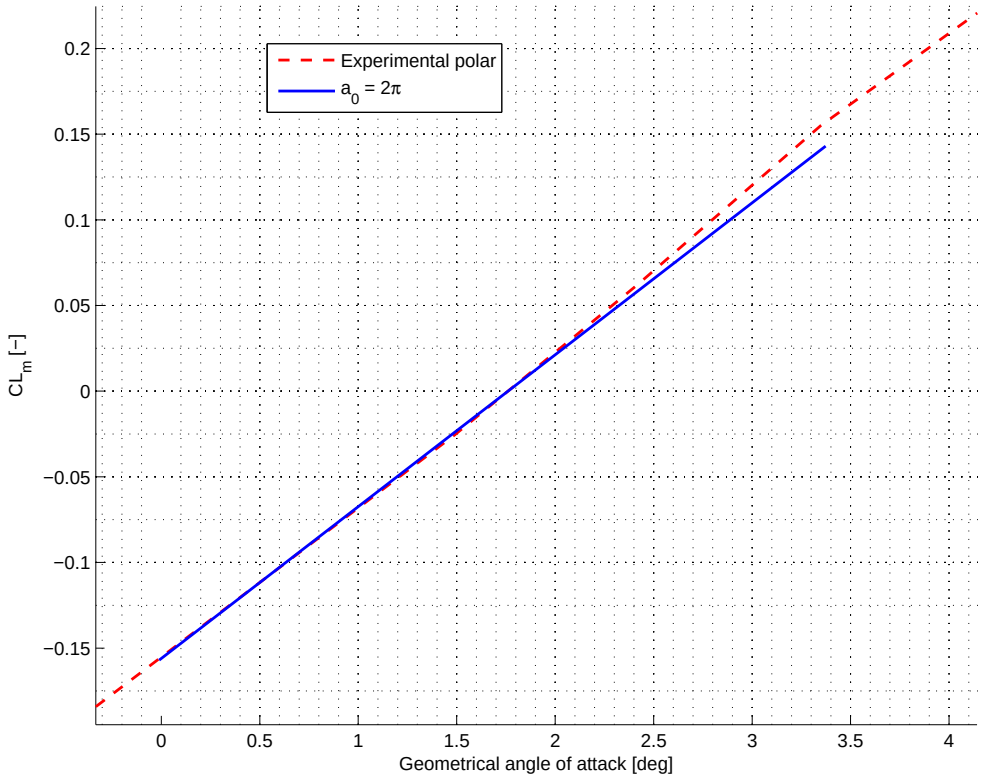

Figure 3.5: Zoom of Figure 3.4.

Actually, if we go back to the conformal transformations theory [16], we see that the *NACA 0012* profile is obtained using the Joukowski's transformation [6]. Furthermore, the analysis of this profile shows that the lift slope value at a zero angle of attack benefits from the thickness of the profile. Mathematically, this is expressed as :

$$\left.\frac{\partial C_l}{\partial \alpha}\right|_{\alpha=0} = \left(1 + \frac{\epsilon}{a}\right) 2\pi \ , \tag{3.5}$$

with ratio $\frac{\epsilon}{a}$ representing the thickness/chord ratio. On our graph, at $\alpha = 0$, the two curves are almost parallel. Thus, the benefits from the thickness of the profile are probably cancelled out by the viscous effects, as the Reynolds number is quite low.

3.1.2 Drag

The following figures show respectively the drag coefficients in function of the angle of attack, the mean drag coefficients in function of the angle of attack, and finally the standard deviation associated to those mean drag coefficients. All the values displayed here only refer to the wing's drag. The drag coefficient associated to the support arms ($C_{D,arms} = 0.077$ on average, computed with respect to the wing's area) is already subtracted.

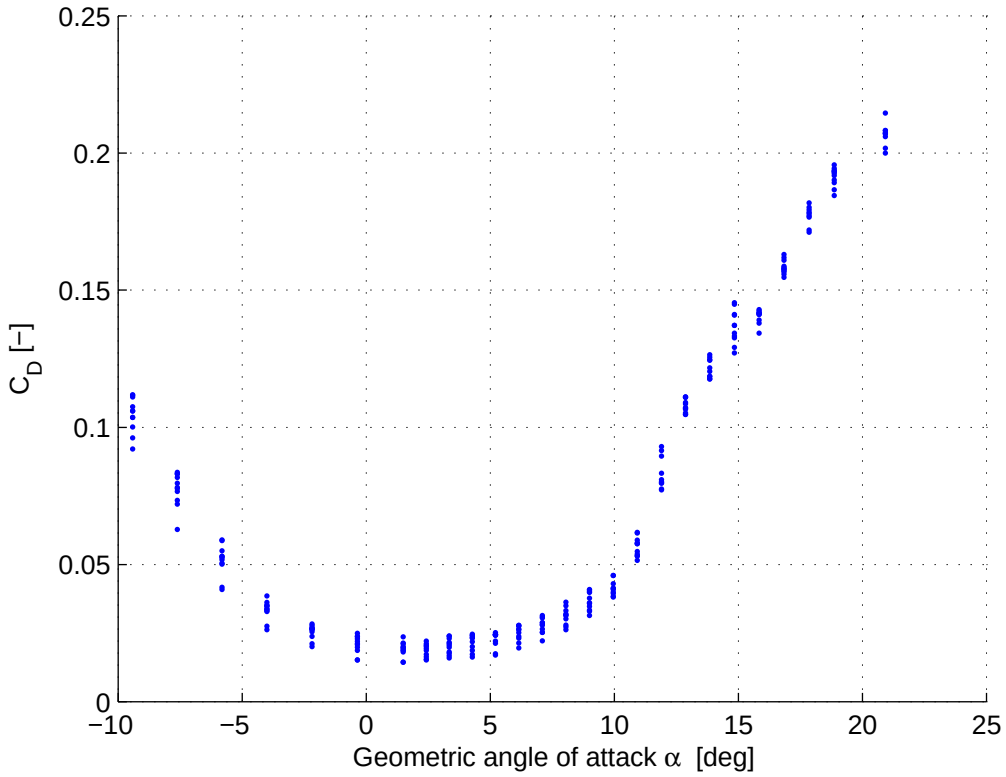

Figure 3.6: Drag coefficients C_D against angle of attack α, $Re_r \approx 10^5$

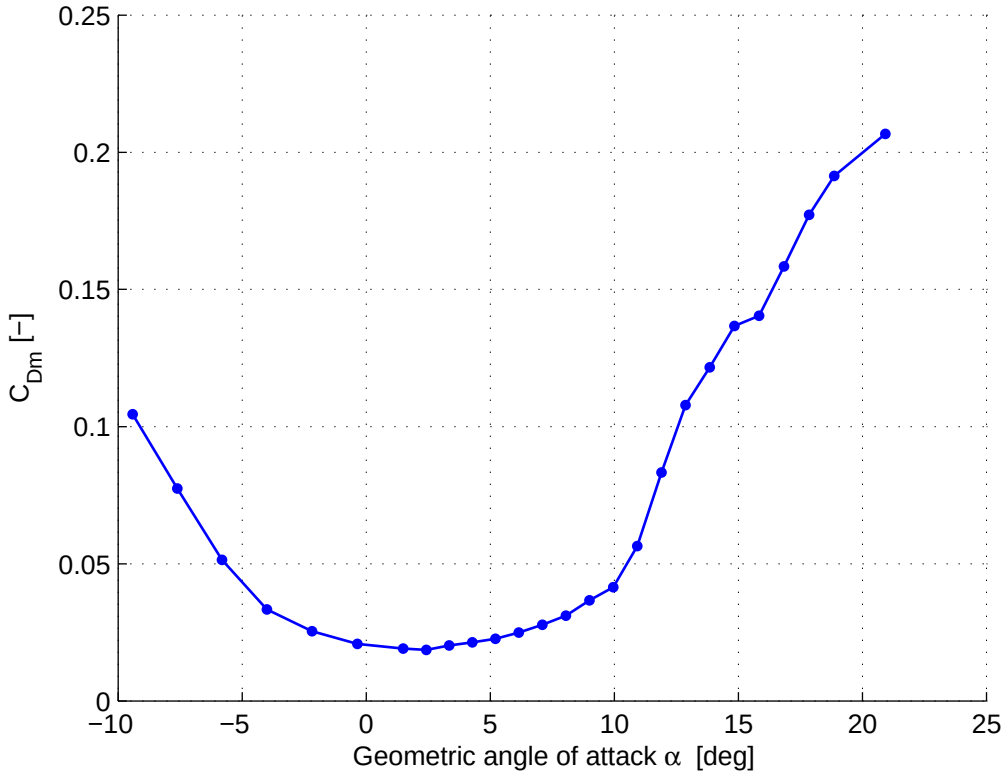

Figure 3.7: Mean drag coefficients C_{D_m} against angle of attack α, $Re_r \approx 10^5$

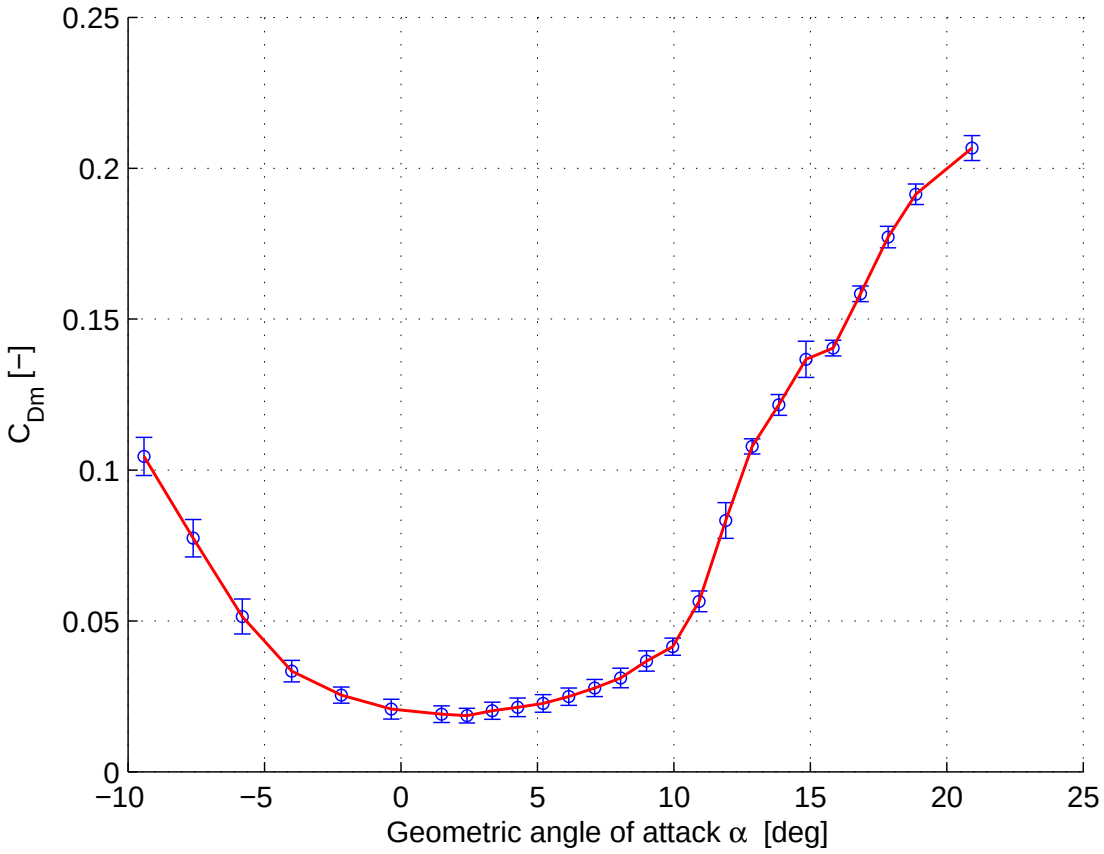

Figure 3.8: Standard deviation associated to the mean drag coefficients against angle of attack α, $Re_r \approx 10^5$

Figure 3.7 shows a minimum drag coefficient $C_{D_0} = 0.019$ with an associated standard deviation of 0.0025.

3.1.3 Wing's polars

Having separately analysed the lift and drag characteristics, we could now take a closer look at the wing's polar. We remind that this one is defined by the equation

$$\begin{aligned} C_D &= C_{D_0} + C_{D_i} \ , \\ &= C_{D_0} + \frac{1}{\pi A_R e} C_L^2 \ , \\ &= C_{D_0} + k C_L^2 \ , \end{aligned} \tag{3.6}$$

with e representing *Oswald*'s efficiency.
We must here clarify that in the Eq. 3.6, the coefficient k has a different meaning depending on whether it is theoretical or experimental. In the theory, it defines, as already explained, the induced drag coefficient. However for experiments, it can be decomposed into two parts : one for the induced drag produced by the wing ($\triangleq k_i$) and the other one for the form drag created by the wing's profiles ($\triangleq \beta$). In fact, we have, for each profile :

$$C_d = C_{d_0} + \beta C_l^2 \ . \tag{3.7}$$

The sum of k_i and β forms k_{eff} which can be measured experimentally :

$$k_{eff} \triangleq k_i + \beta \ . \tag{3.8}$$

The analysis of the *NACA0012* polars (see Figure 2.8) made it possible to determine the value of β, even if the available data for such a low Reynolds number is quite limited :

$$\beta \approx 7.1\ 10^{-3} \ .$$

We then had to deduce this value to the measured k_{eff} in order to find our experimental k_i. So, by plotting $C_{L_m}^2$ in function of C_{D_m}, we were be able to determine the value of k_{eff} (for moderate angles of attack) and in turn, deduce the induced drag coefficient. Before doing so, we must remember from the Prandtl's theory that the *bell* wing is supposed to produce 11% less induced drag than the elliptic wing ($k_{i,bell} \approx 0.89\ k_{i,elliptic}$).

Polars computed in [7] (Figure 3.10) were used to determine those characteristics for the elliptic wing.

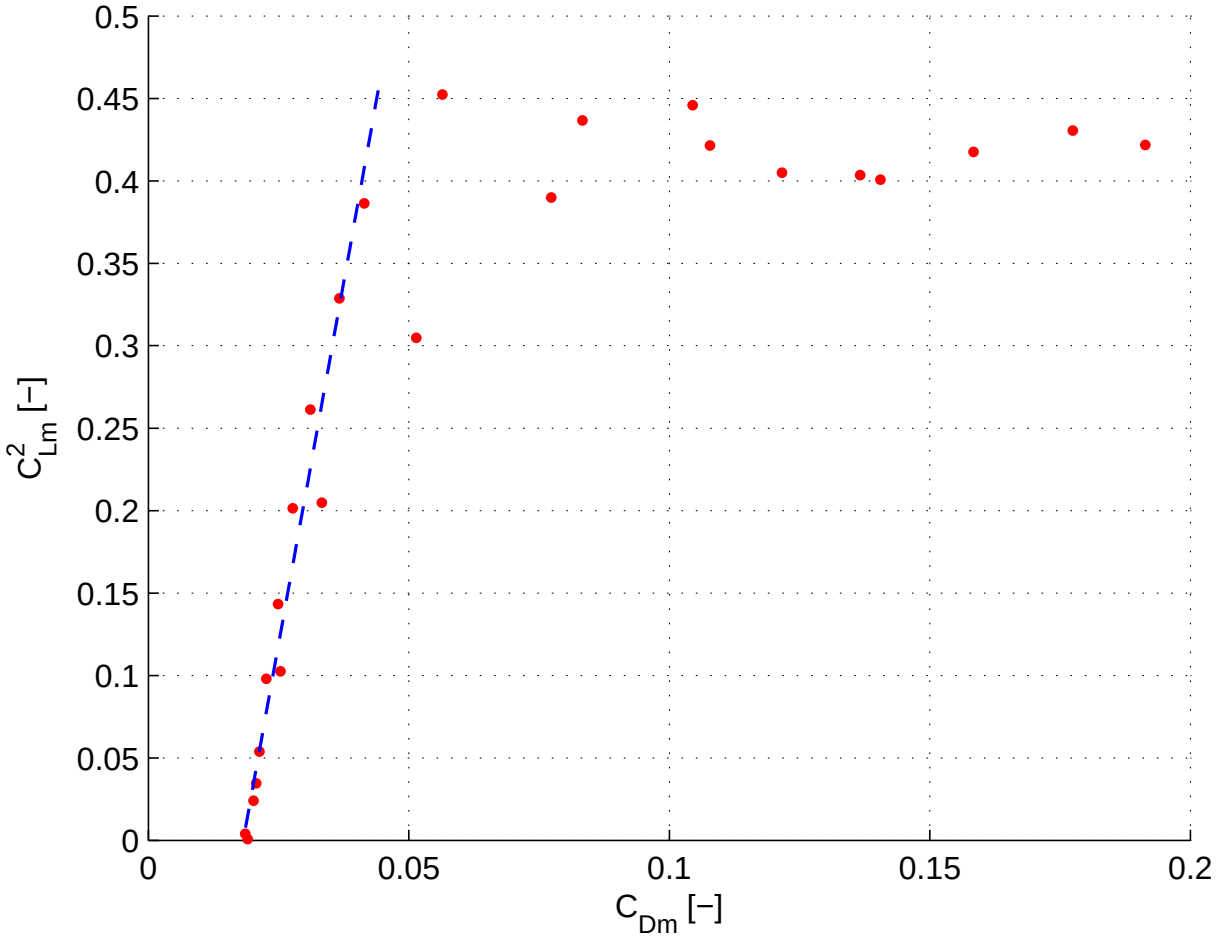

Figure 3.9: Plot of $C_{L_m}^2$ against C_{D_m} for the *bell* wing. The dashed line has a slope coefficient equal to k, $Re_r \approx 10^5$

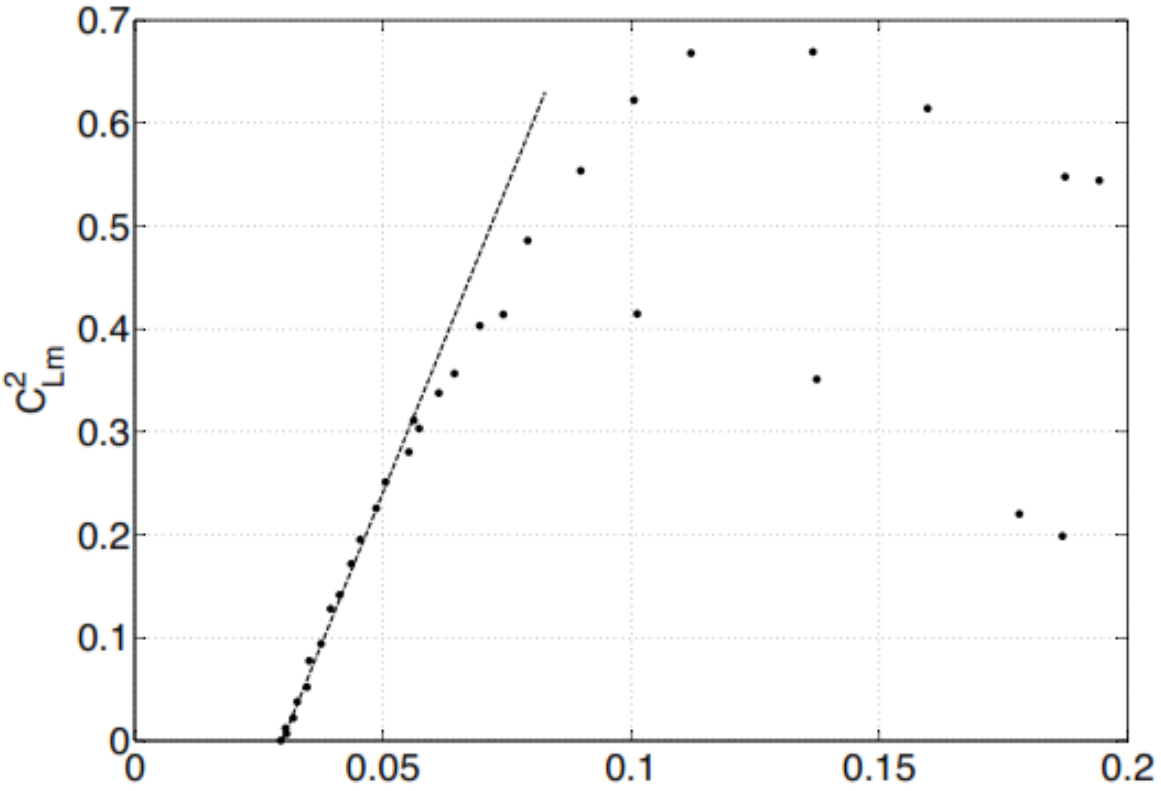

Figure 3.10: Plot of $C^2_{L_m}$ against C_{D_m} for the elliptic wing, $Re_r \approx 10^5$.

The analysis of Figures 3.9 and 3.10 is shown in Table 5. The theoretical induced drag coefficients were computed for a lift coefficient $C_L = 0.4$. The values of k_i and the Oswald's efficiencies e were calculated for both wings with their respective aspect ratio ($A_{R,bell} = 9.0$, $A_{R,elliptic} = 6.0$) and with the polar equation.

		C_{D_i} $(C_L = 0.4)$	k_{eff}	k_i	e
Bell	Theoretical	$7.54\ 10^{-3}$	/	$4.71\ 10^{-2}$	0.750
	Experimental	$7.84\ 10^{-3}$	$5.61\ 10^{-2}$	$4.90\ 10^{-2}$	0.722
	Error from theory	4.0%	/	4.0%	−3.7%
Elliptic	Theoretical	$8.48\ 10^{-3}$	/	$5.30\ 10^{-2}$	1.000
	Experimental	$9.57\ 10^{-3}$	$6.69\ 10^{-2}$	$5.98\ 10^{-2}$	0.887
	Error from theory	12.8%	/	12.8%	−11.3%

Table 5: Theoretical and experimental results for the induced drag coefficients C_{D_i}, k and the Oswald's efficiency for the *bell* wing and the elliptic wing.

The difference in induced drag between the *bell* and elliptic wings is close to 22%, almost twice the expected value of 11%. But we also see that the results for the *bell* wing are more precise than for the elliptic wing.
Therefore, we can almost certainly state that the *bell* wing has better performance than the elliptic wing, but because of the inaccuracies in the elliptic wing measurements, we cannot

precisely quantify the actual reduction of induced drag produced by the *bell* wing. Finally, Figure 3.12 helps to determine the maximum lift/drag ratio :

$$f_{max} = 16.41 \ . \tag{3.9}$$

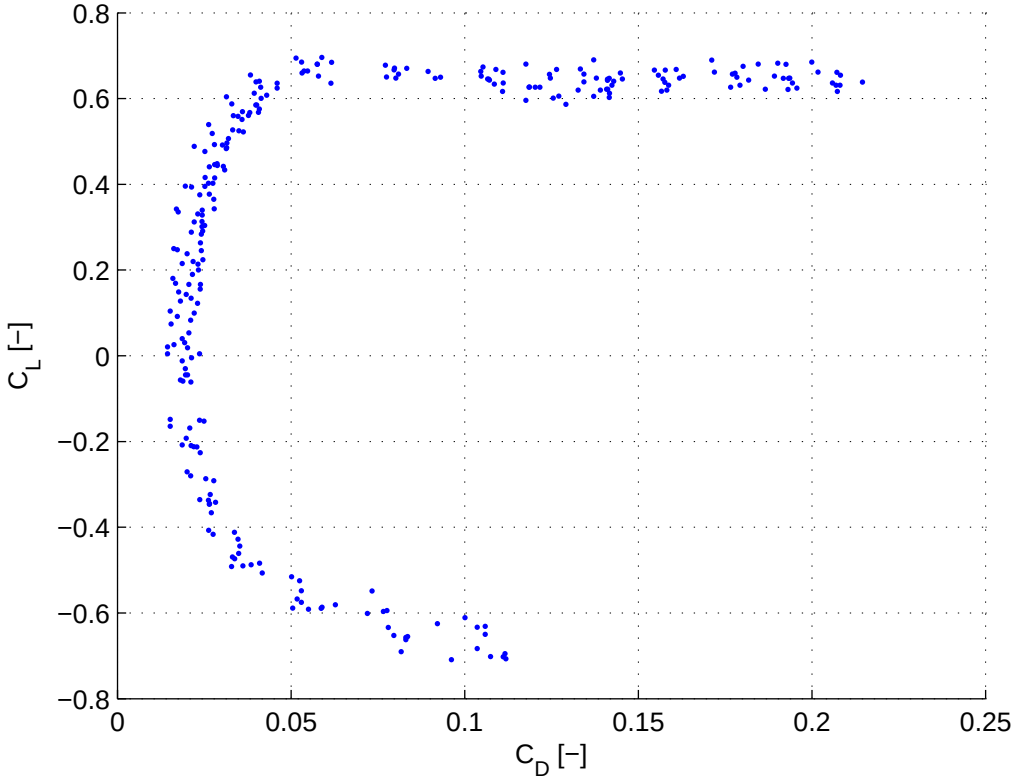

Figure 3.11: Lift coefficients C_L against drag coefficients C_D, $Re_r \approx 10^5$

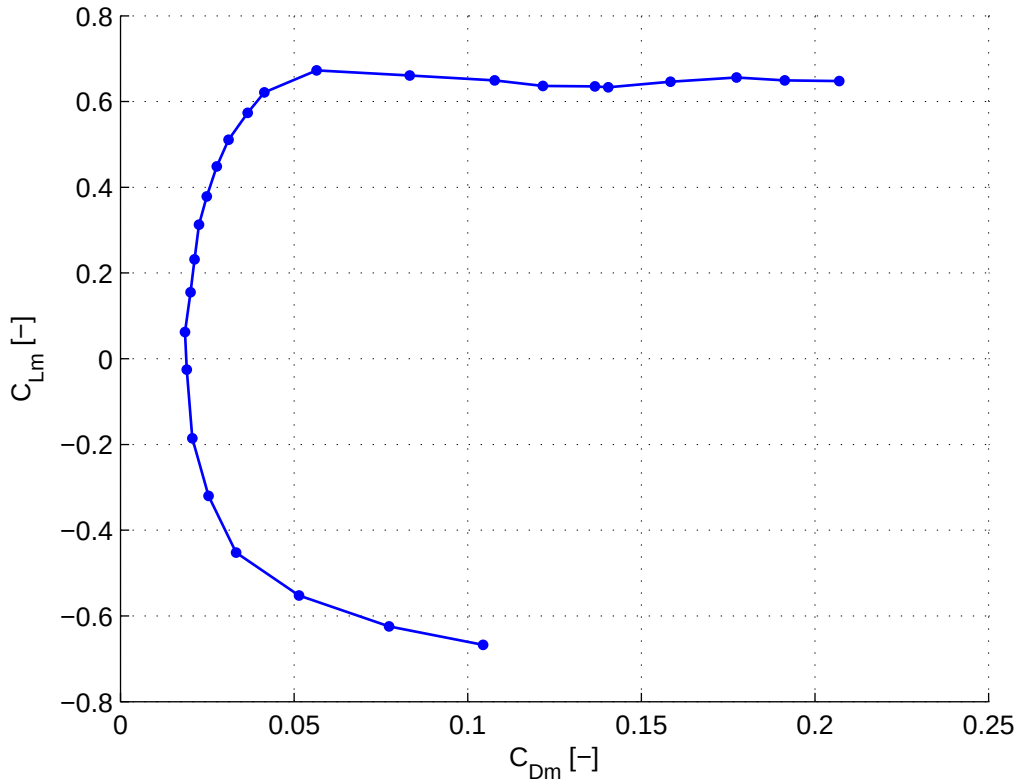

Figure 3.12: Mean lift coefficients C_L against mean drag coefficients C_D, $Re_r \approx 10^5$

The last graph shows the standard deviation for the $C_{Lm}(C_{Dm})$ curve.

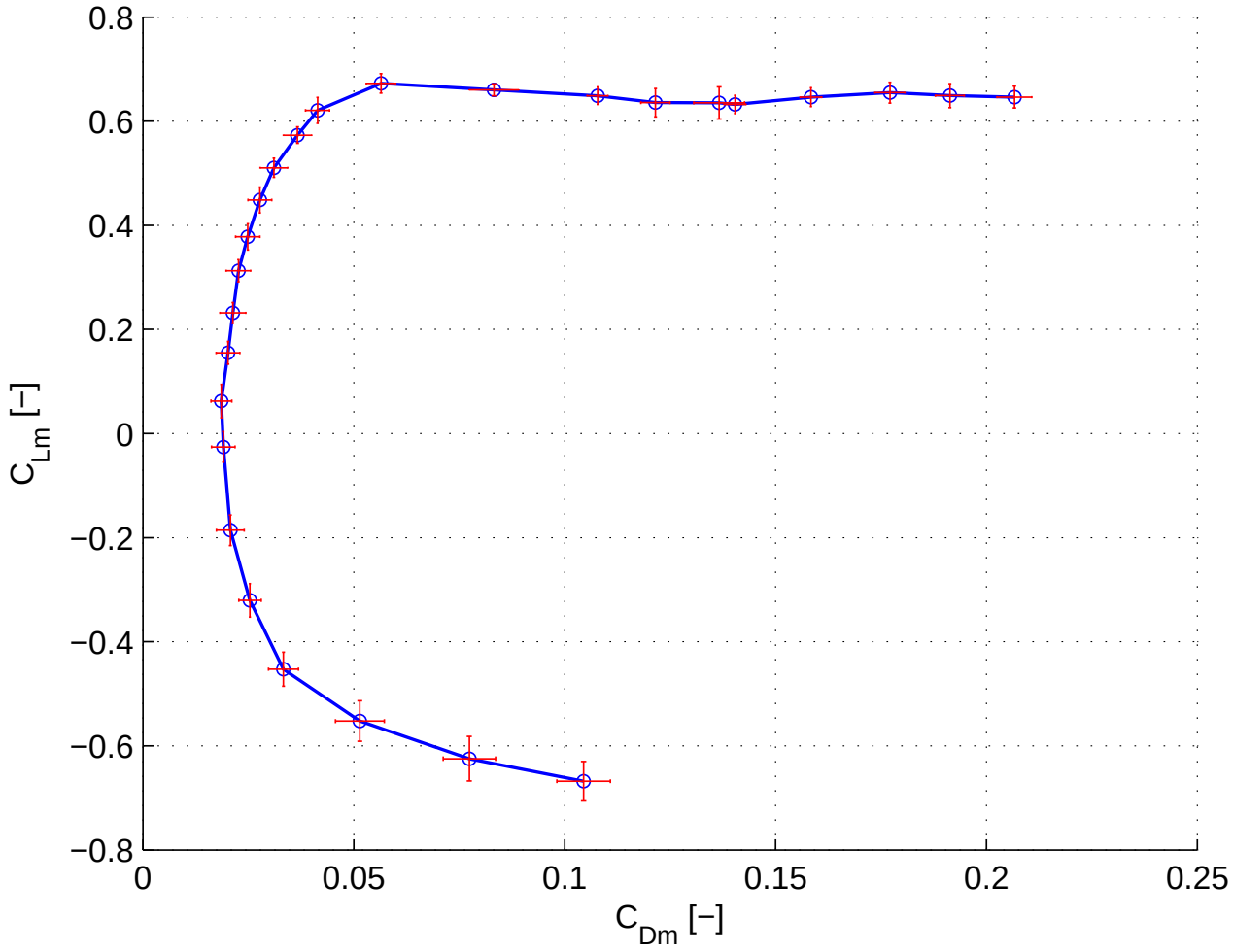

Figure 3.13: Standard deviations for the $C_{Lm}(C_{Dm})$ curve, $Re_r \approx 10^5$

Finally, Table 6 summarises all the aerodynamic characteristics for the elliptic wing [7] and the *bell-shaped* wing.

Characteristic	Elliptic wing	Bell wing	Departure
A_0	4.49	4.78	+6.4%
C_{D_0}	0.028	0.019	−32.2%
$C_{L_{max}}$	0.810	0.672	−17.0%
f_{max}	10.00	16.41	+64.1%
k_i	0.059	0.049	−17.0%
e	0.887	0.722	−18.6%
$C_{D_i}(C_L = 0.4)$	$9.57\ 10^{-3}$	$7.84\ 10^{-3}$	−18.1%

Table 6: Aerodynamic characteristics for elliptical and bell wings with departures from the elliptical wing values.

3.2 PIV results and analysis

The primary goal of the PIV experiments was to investigate some of the wing's characteristics that the aerodynamic balance could not, as the spanwise distributions, for example. However, not all of those distributions could be validated using the PIV equipment. In fact, we recall that the Prandtl's theory is only a model. We therefore do not expect the results to be as the theory predicts, but we will examine how close they approach it.
Also, only integrated values will be examined, as the local ones depend on too many experimental factors. For example, the downwash velocity distribution $\epsilon(y)$ predicted by the Prandtl's theory is, as we recall the first chapter of this document, only based on the velocity induced by the vortex filaments, but do not take into account the local experimental conditions, such as the acceleration of the flow when passing the airfoil or the turbulence in the upstream flow, for examples. Also, the theory do not precise where the measurements should be taken. Integrated values are therefore more suited to experiments as, by definition, they are calculated on a region and not a single point or line.
Furthermore, as the wing is symmetrical, only its right part was examined, providing therefore better accuracy in the measurements. Nonetheless, we must pay attention that the seeding is made with quite big water droplets (around 10^{-9} $[kg/droplet_{water}]$ against 10^{-15} $[kg/droplet_{oilve\ oil}]$), which, in addition to their large inertia, condense on the wing's surfaces after a short period of time, resulting in potential disturbance in the flow.
Finally, we can point out several factors that may alter the results:

- The difference in particles density across the laser sheet: the droplets spray is denser at its centre. The results may then be less precise close to the edges of the images.
- The flow will be disturbed behind the support arms and the angle of attack adjustment wire.

3.2.1 Circulation distribution $\Gamma(y)$ validation

The main parameter investigated during PIV tests is the circulation distribution $\Gamma(y)$. In fact, the circulation Γ is defined by a contour integration (3.10) or a surface integration (3.11)

$$\Gamma \triangleq \oint_C \underline{v} \cdot \underline{dl} \ , \tag{3.10}$$

$$\Gamma \triangleq \int_S \underline{\omega} \cdot \underline{n}\, ds \ . \tag{3.11}$$

As the PIV software allows to calculate both the velocity components (in 3D) and vorticity (in the x-direction) vectors, the circulation distribution $\Gamma(y)$ could be validated in two different ways.

Surface integral

Here below is an example of how the wake vorticity is represented after the processing and averaging of hundreds of frames. This image is the representation of a 1904-by-1296 matrix (those dimensions may vary depending on the calibration made before the tests) containing all the vorticity values across the wake, at a distance $x = 10^{-3}$ $[m]$ behind the trailing edge.

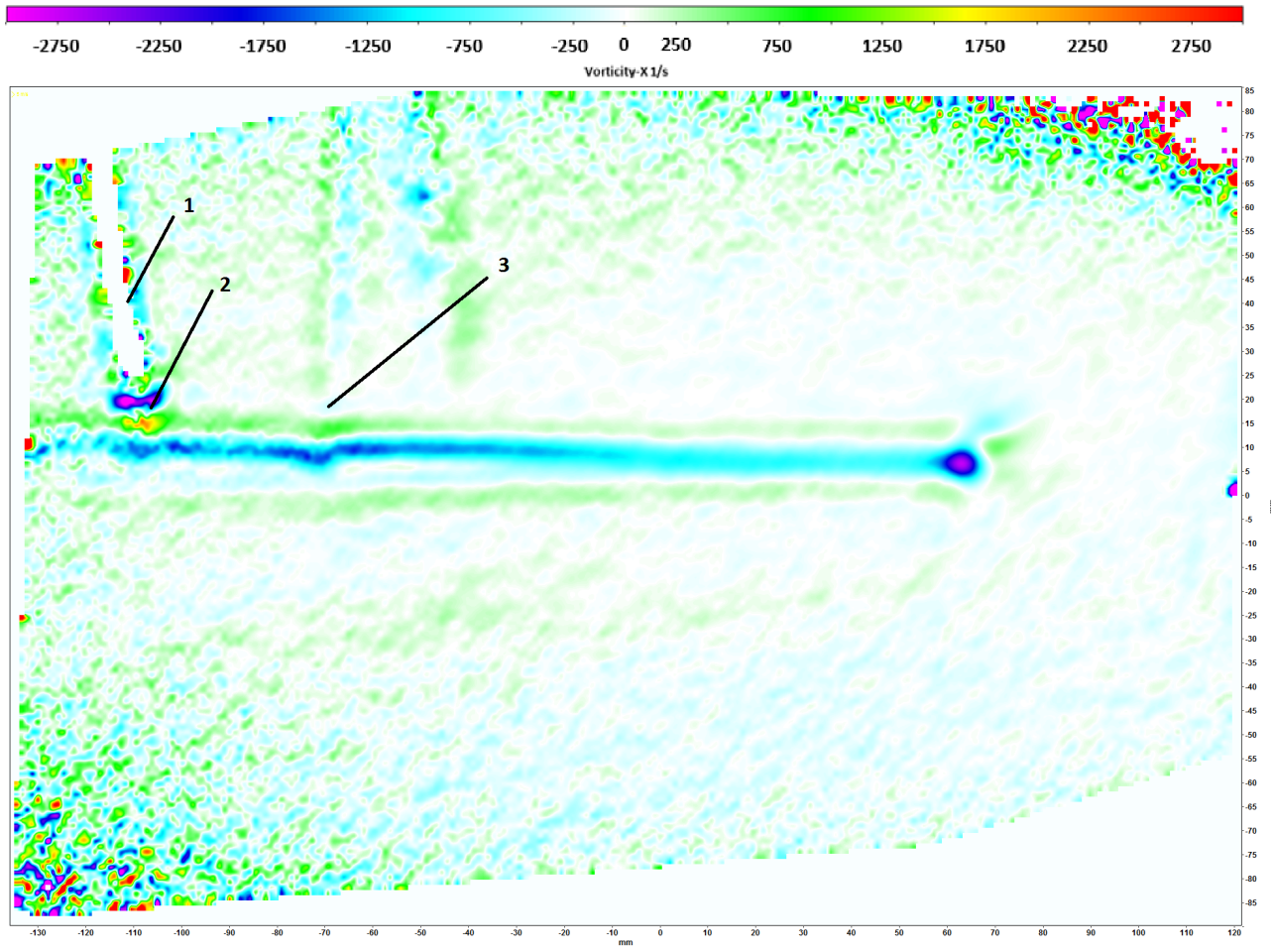

Figure 3.14: Vorticity values ω_x $[1/s]$ at $x = 10^{-3}$ $[m]$ behind the trailing edge, $C_L = 0.6$, $Re_r \approx 10^5$. **1**: Pitch adjusting wire sighted in the laser sheet, **2**: Connecting bit between pitch adjusting wire and wing, **3**: Wake of the support arms.

As we see, the values are well defined in the centre of the image while they tend to be inconsistent on its sides, where the seeding density is lower.
The theoretical formula to compute the value of Γ along the *y-axis* is (considering a wake in a still air mass)

$$\Gamma(y) = \int_{-\infty}^{\infty} \int_{-\infty}^{y} \underline{\omega_x}(y', z')\, dy'\, dz' \ . \tag{3.12}$$

In our case however, the vorticity values do not tend to zero as we approach the bottom and top edges of the image. $z' \to -\infty$ and $z' \to \infty$ cannot thus be taken as correct z' boundaries. Each image had thus to be examined to determine its best z' boundaries. Concerning the y' boundaries, they were taken from $y' = b/2$ to $y' = y$:

$$\Gamma(y) = \int_{z_{inf}}^{z_{sup}} \int_{b/2}^{y} \underline{\omega_x}(y', z')\, dy'\, dz' \ . \tag{3.13}$$

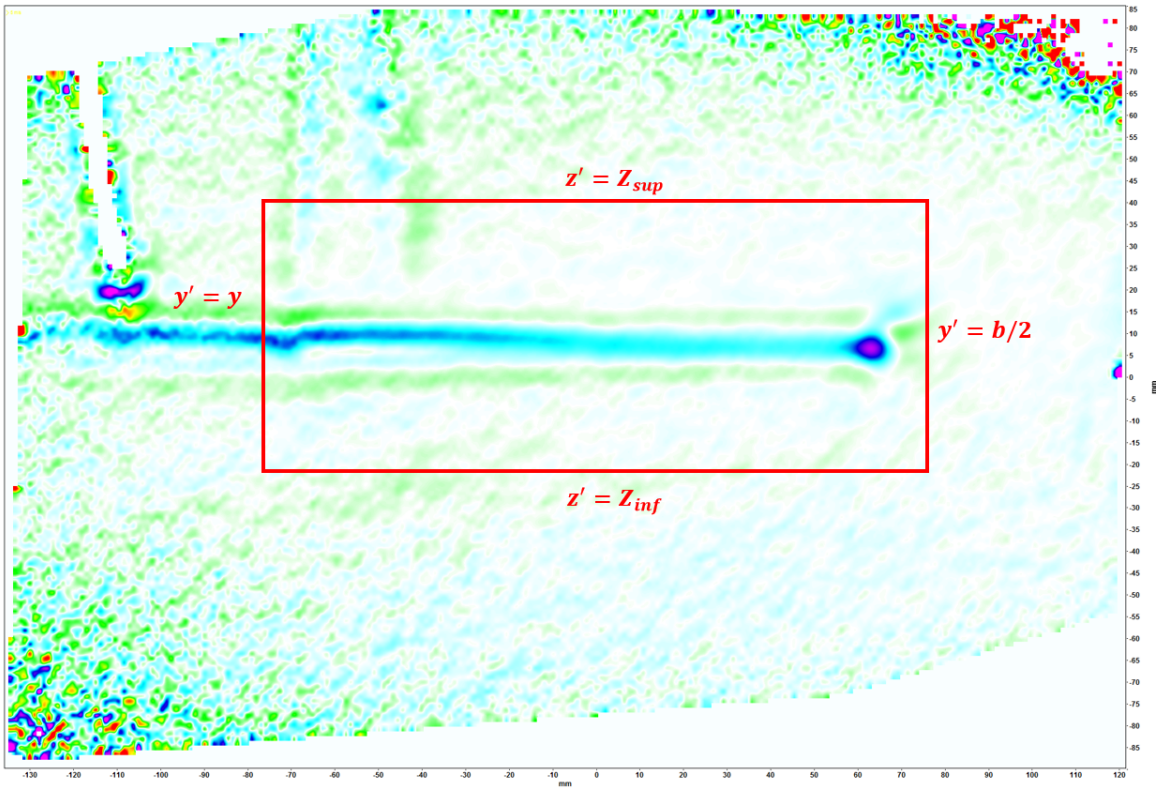

Figure 3.15: Example of boundaries for the vorticity surface integral.

The graphs below show the experimental curves compared to the theoretical ones given by the Prantdl's theory, for the lift coefficients $C_L = [-0.1, 0.1, 0.4, 0.6]$, at a distance $x = 10^{-3}$ $[m]$ from the *bell wing*'s trailing edge. The case of the elliptic wing at $C_L = 0.4$ is also given. Each graph is associated with its wake's vorticity image as calculated by the PIV software (more detailed in [17]).

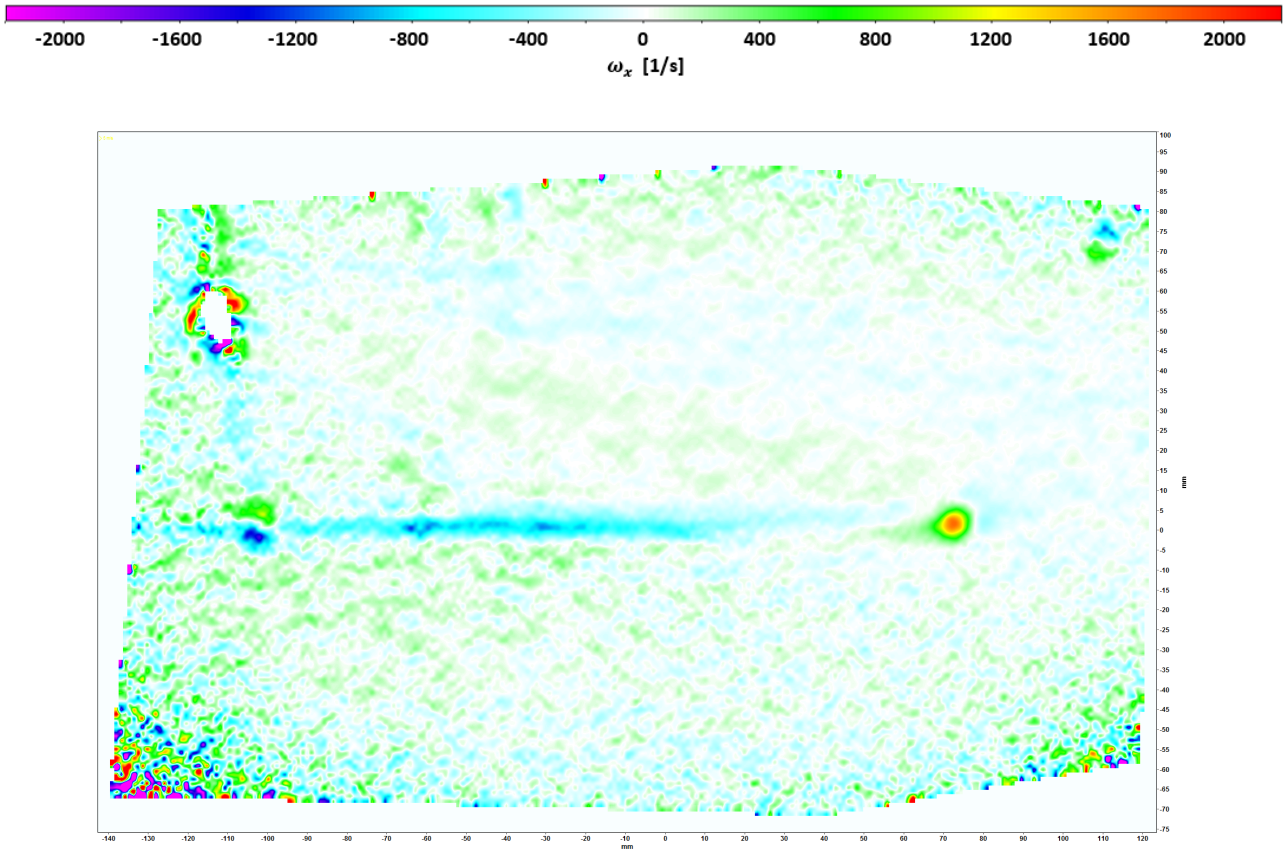

(a) ω_x $[1/s]$

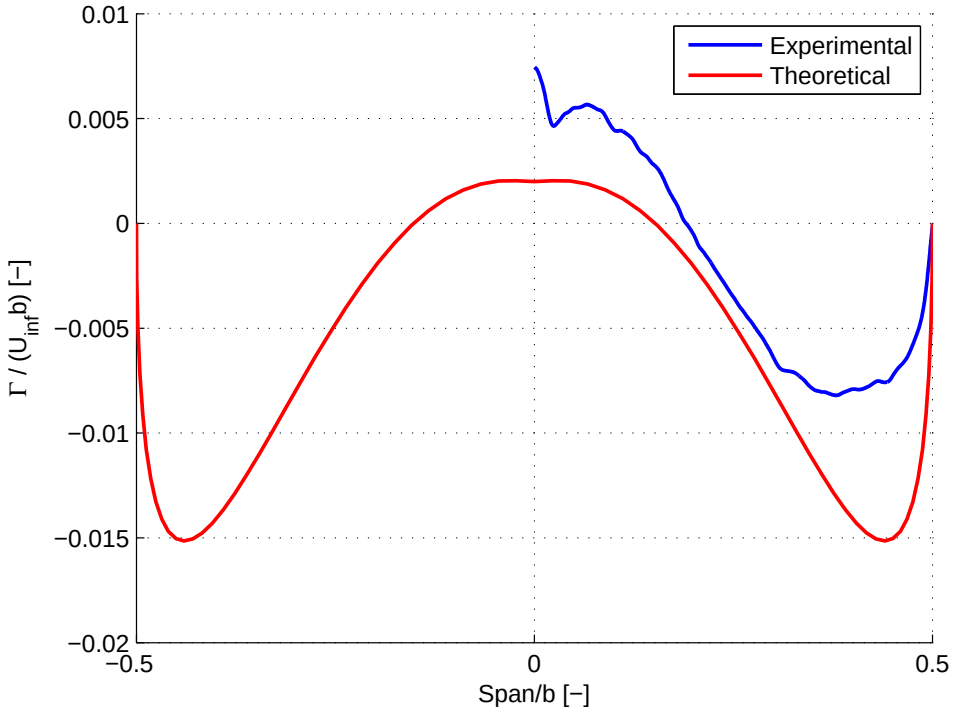

(b) Experimental circulation distribution $\Gamma(y)$ (surface integral method) against theoretical curve (Prandtl's theory).

Figure 3.16: Test at $C_L = -0.1$, $x = 10^{-3}$ behind trailing edge, $Re_r \approx 10^5$

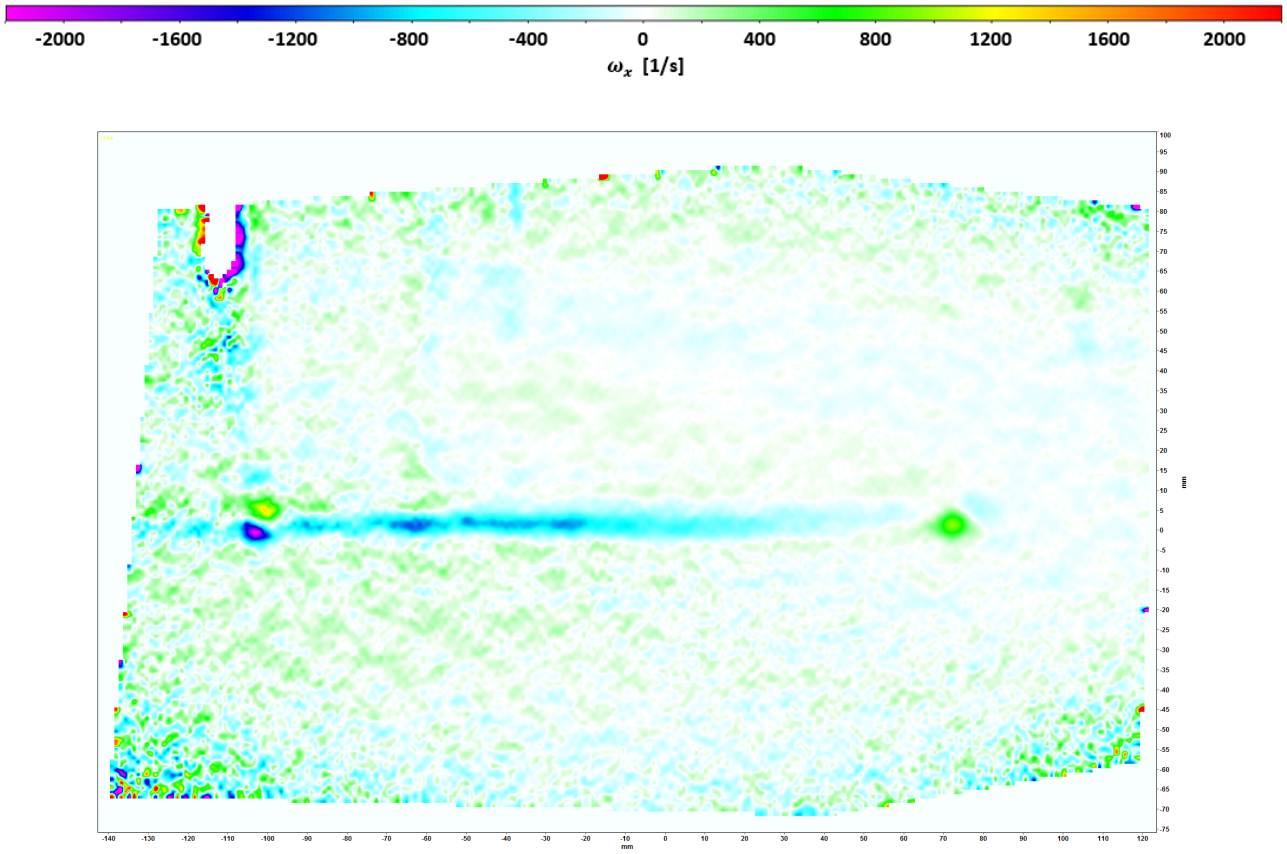

(a) ω_x $[1/s]$

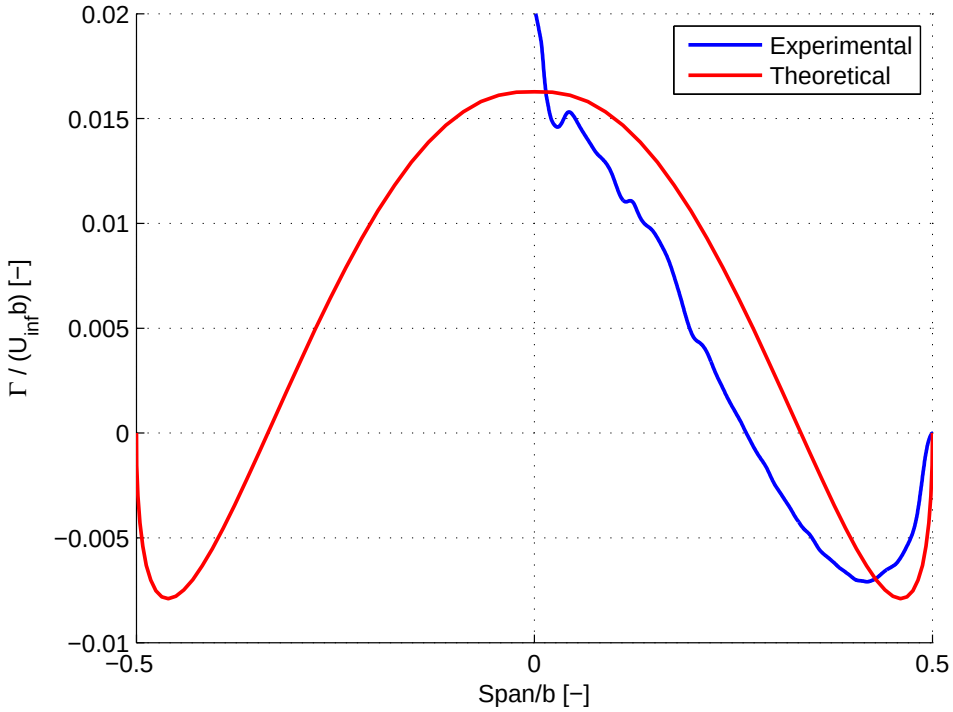

(b) Experimental circulation distribution $\Gamma(y)$ (surface integral method) against theoretical curve (Prandtl's theory).

Figure 3.17: Test at $C_L = 0.1$, $x = 10^{-3}$ behind trailing edge, $Re_r \approx 10^5$

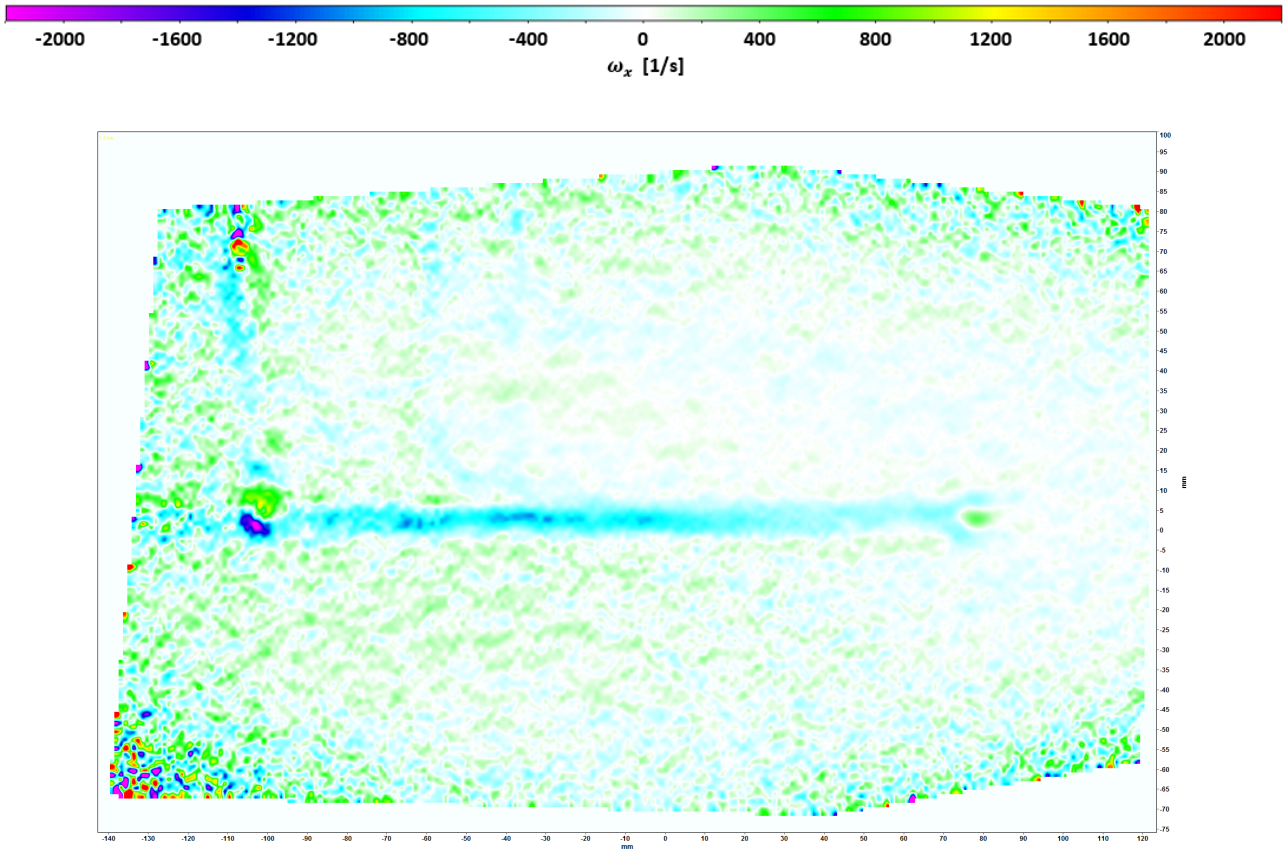

(a) ω_x $[1/s]$

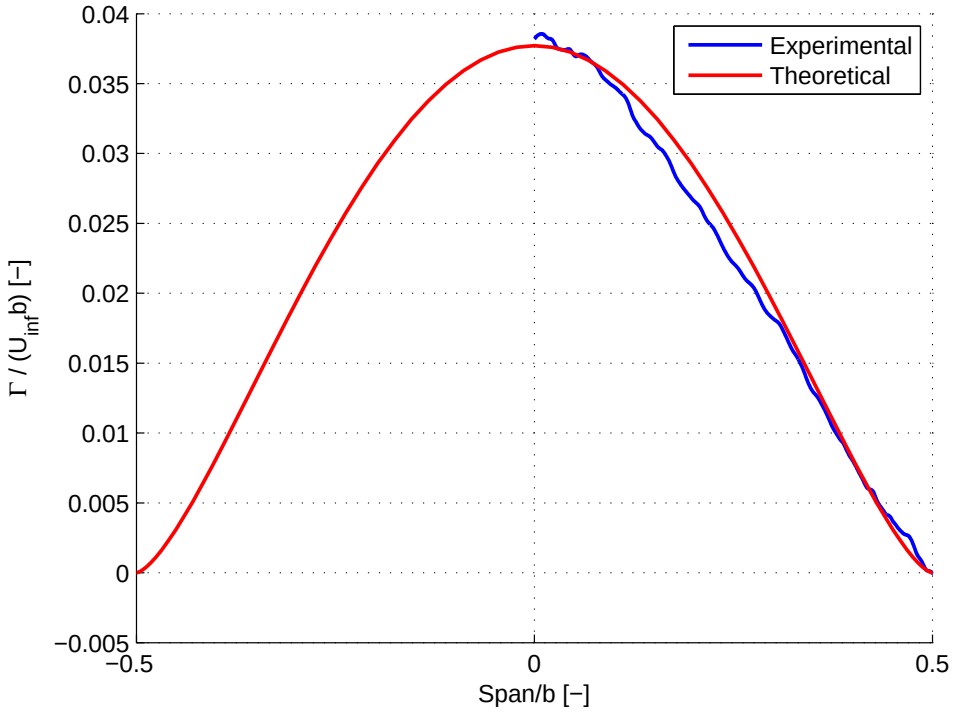

(b) Experimental circulation distribution $\Gamma(y)$ (surface integral method) against theoretical curve (Prandtl's theory).

Figure 3.18: Test at $C_L = 0.4$, $x = 10^{-3}$ behind trailing edge, $Re_r \approx 10^5$

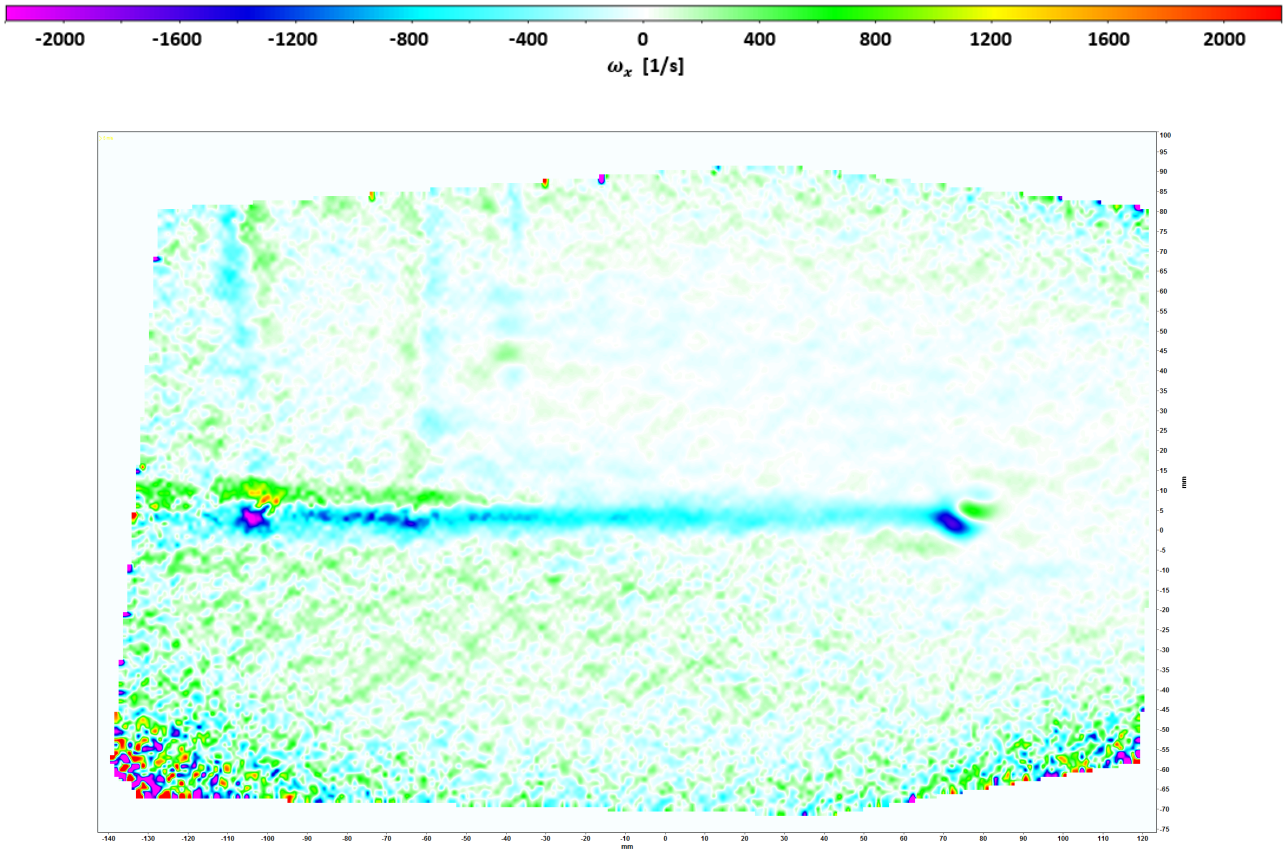

(a) ω_x $[1/s]$

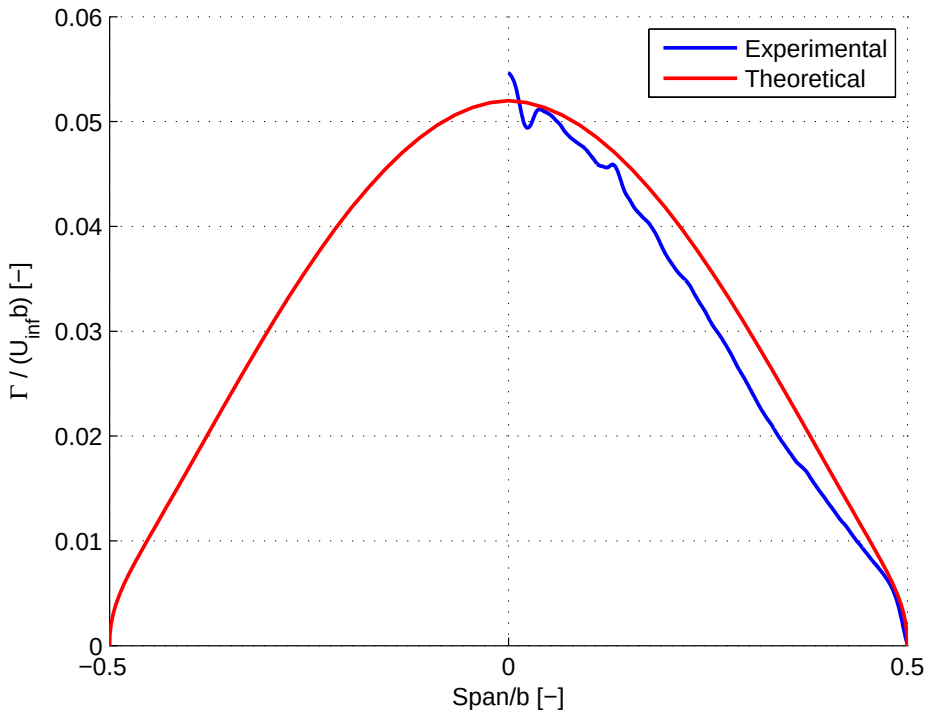

(b) Experimental circulation distribution $\Gamma(y)$ (surface integral method) against theoretical curve (Prandtl's theory).

Figure 3.19: Test at $C_L = 0.6$, $x = 10^{-3}$ behind trailing edge, $Re_r \approx 10^5$

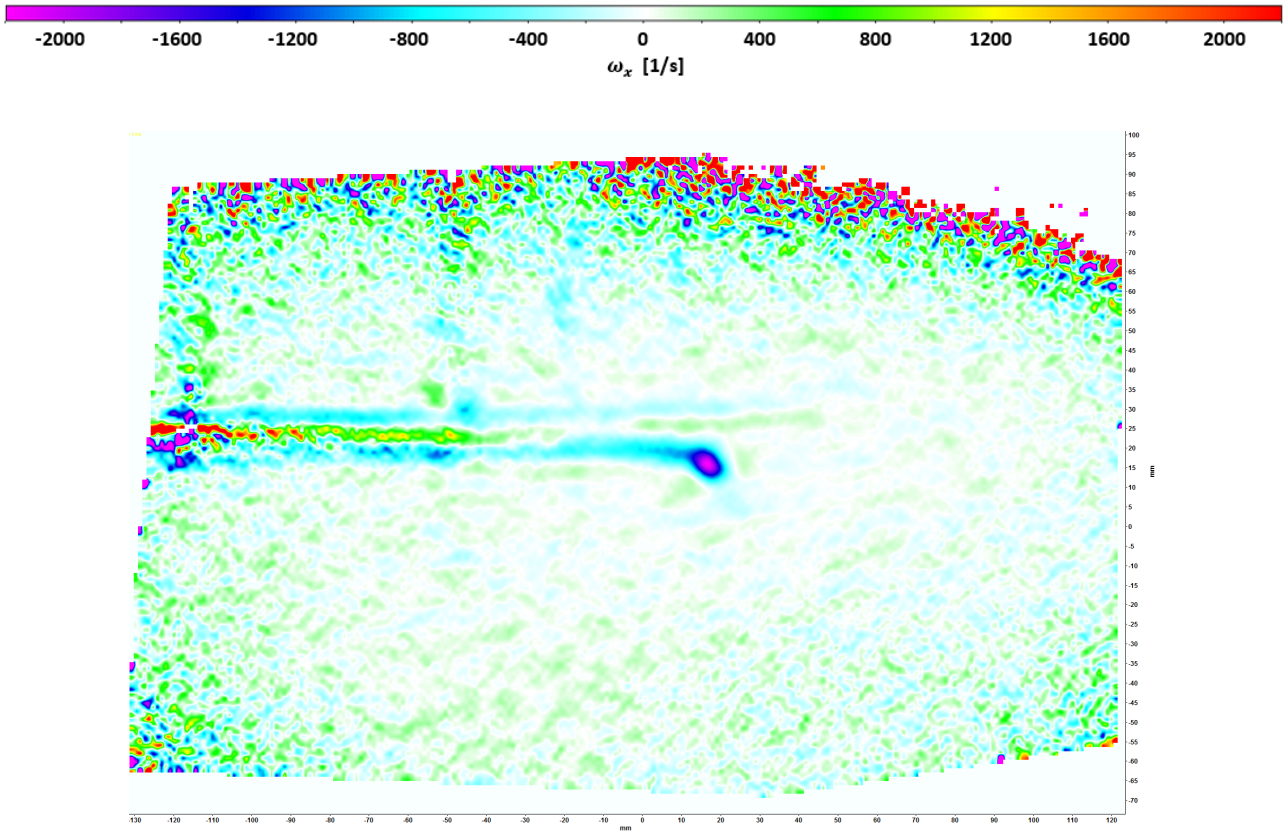

(a) ω_x $[1/s]$

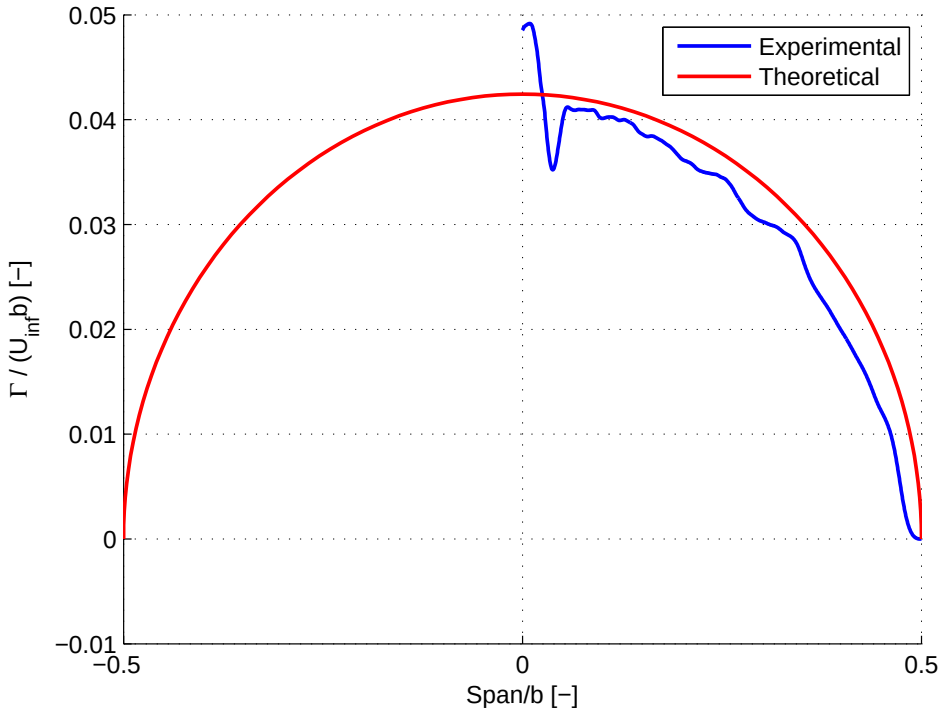

(b) Experimental circulation distribution $\Gamma(y)$ (surface integral method) against theoretical curve (Prandtl's theory).

Figure 3.20: Test at $C_L = 0.4$ with the elliptic wing, $x = 10^{-3}$ behind trailing edge, $Re_r \approx 10^5$

In a general way, the global shape of the experimental curves match largely the theoretical ones, except for the centre of the wing, where the connection bit between the wing and its pitch adjusting wire creates some turbulent air.
But we must bear in mind that for each experiment, the lift coefficient was calculated based on the lift value provided by the aerodynamic balance. A small departure between the measured and the target values could then partially explain the differences between the expected and computed curves, as those latter might therefore not represent the correct C_L case.
This might be the main reason why most anomalies are found on the graphs corresponding to $C_L = -0.1$ and $C_L = 0.1$.
Concerning the cases $C_L = 0.4$ and $C_L = 0.6$, the Prandtl's model seems to be quite exact for both wings as the curves almost match everywhere along the span.
The four different C_L cases are gathered on the next figure:

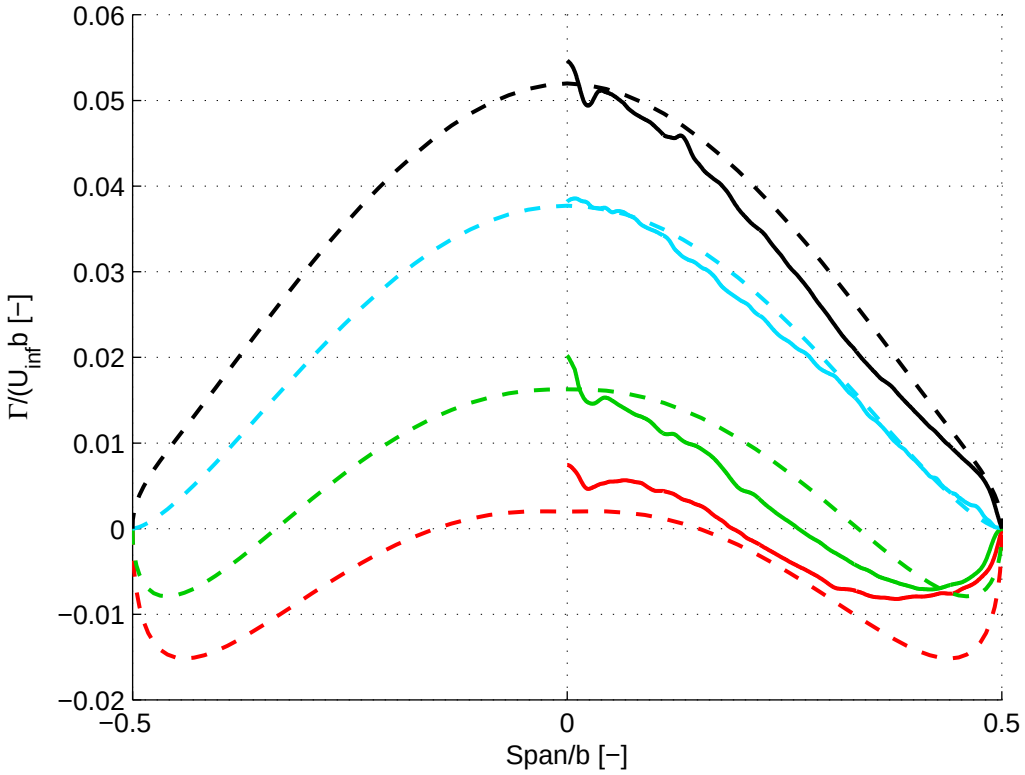

Figure 3.21: Experimental circulation distributions $\Gamma(y)$ (surface integral method)(solid lines) against theoretical curves (dashed lines) for different lift coefficients (red: $C_L = -0.1$, green: $C_L = 0.1$, cyan: $C_L = 0.4$, black: $C_L = 0.6$), $x = 10^{-3}$ $[m]$ from trailing edge, $Re_r \approx 10^5$

Contour integral

The contour integral requires to know the velocities in the y-z plane (v and w). As for the vorticity ω, the velocities are provided by the PIV software in the form of a matrix whose dimensions depend on the current test.
Here below are shown the velocities v and w, corresponding to the case displayed in Figure 3.14.

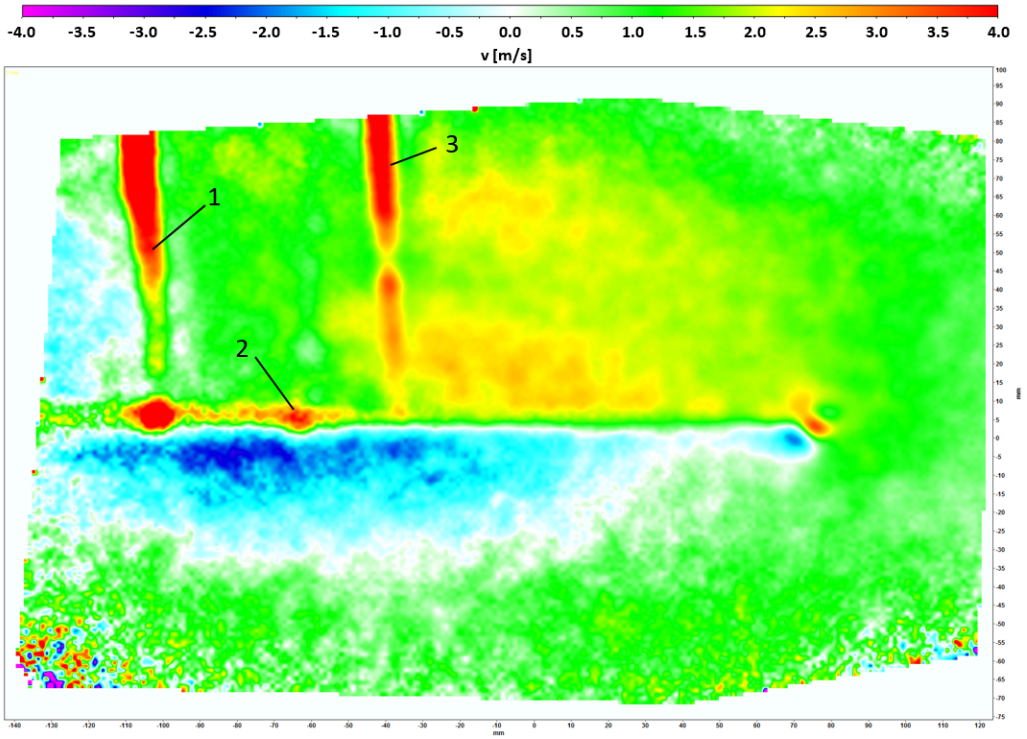

(a) *y-axis* velocity v $[m/s]$

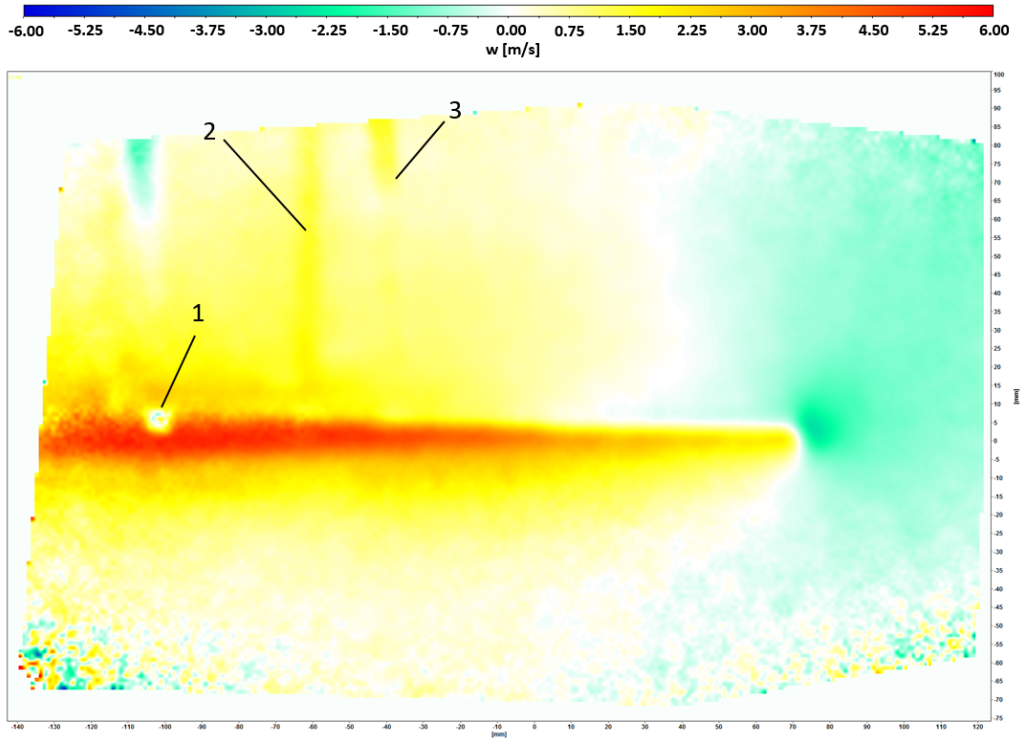

(b) *z-axis* velocity w $[m/s]$

Figure 3.22: *y-z plane* velocities at $x = 10^{-3}$ $[m]$ behind the trailing edge, $C_L = 0.6$, $Re_r \approx 10^5$. **1**: Pitch adjusting wire, **2**:Wake of the support arms, **3**: Reflection of the laser light on the support arms, interpreted as particles during processing.

Again, we see the influence of the pitch adjusting wire and the supporting arms. Also, the water droplets tend to scatter the laser light, which is then reflected on the support arms. This reflection is in turn interpreted as particles during the processing. We can thus discard those three regions during our analysis.
If half the wingspan is discretized in n points by the PIV software, n contours will have to be integrated in order to get our experimental curves. Those contours C are defined as shown on Fig. 3.23:

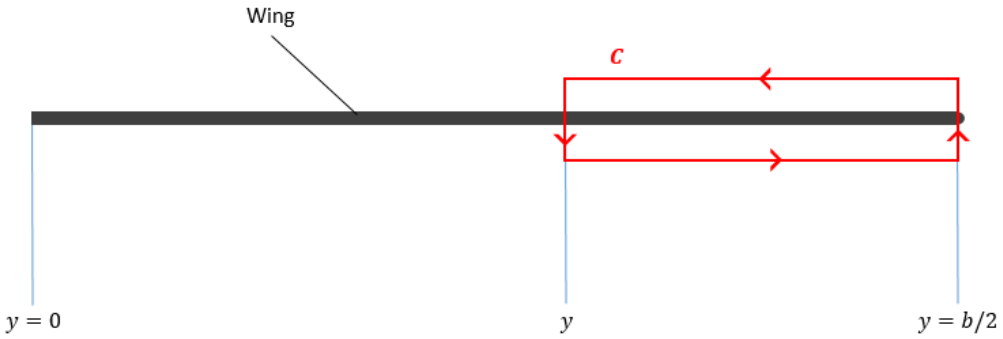

Figure 3.23: Example of a contour C around the wing.

The vertical leg at $y = b/2$ remains fixed, while the other one will progressively move towards $y = 0$ as the contours' size increases.
Here below are the comparison between the experimental curves, computed by the contour integral method, and the theoretical ones for $C_L = [-0.1, 0.1, 0.4, 0.6]$ (for the *bell wing*) and $C_L = 0.4$ for the elliptic wing. Each graph is associated with the corresponding v and w velocity components (images more detailed in [17]).

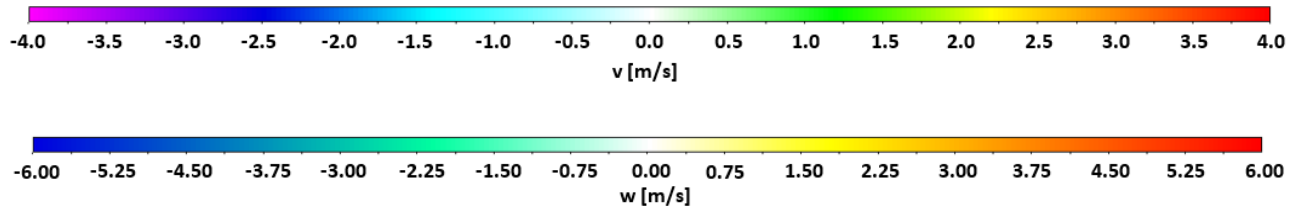

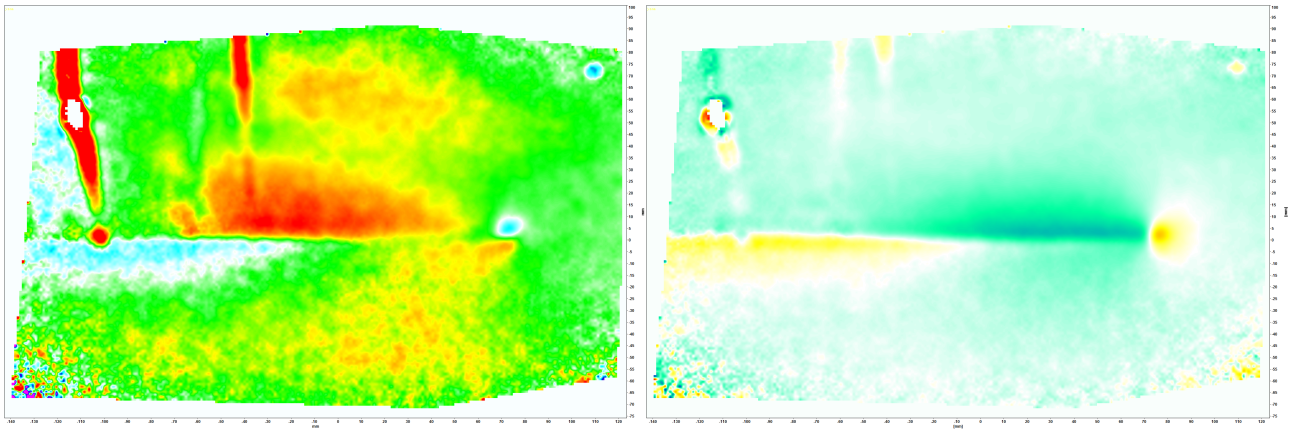

(a) v $[m/s]$ (b) w $[m/s]$

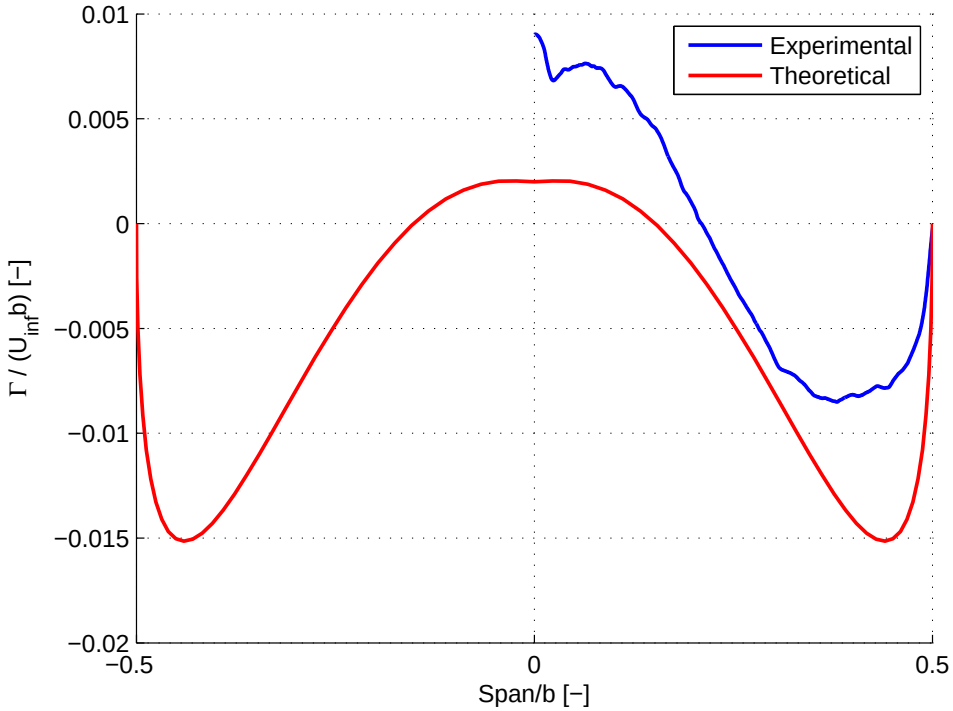

(c) Experimental circulation distribution $\Gamma(y)$ (contour integral method) against theoretical curve (Prandtl's theory).

Figure 3.24: Test at $C_L = -0.1$, $x = 10^{-3}$ behind trailing edge, $Re_r \approx 10^5$

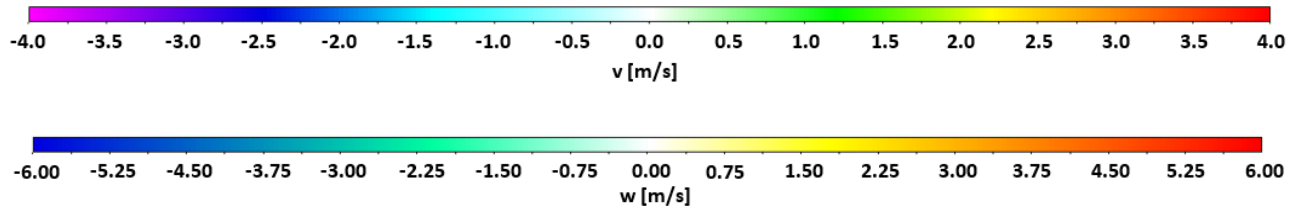

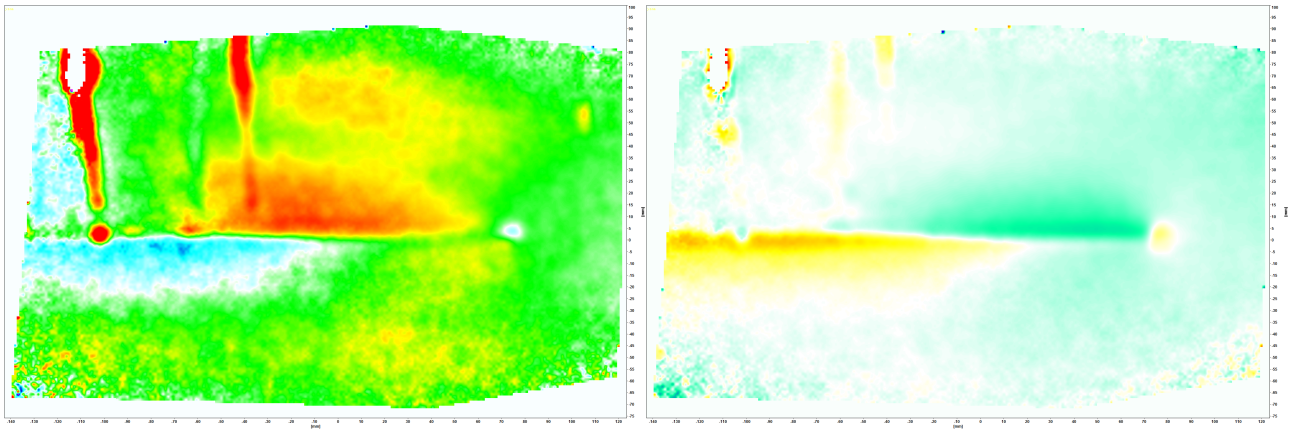

(a) v $[m/s]$ (b) w $[m/s]$

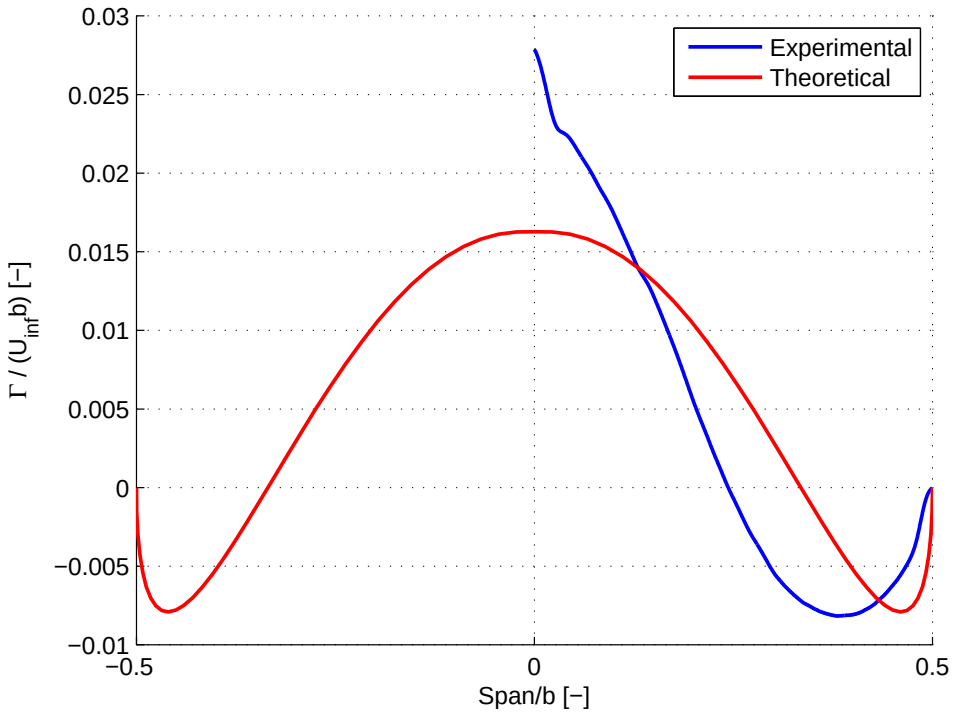

(c) Experimental circulation distribution $\Gamma(y)$ (contour integral method) against theoretical curve (Prandtl's theory).

Figure 3.25: Test at $C_L = 0.1$, $x = 10^{-3}$ behind trailing edge, $Re_r \approx 10^5$

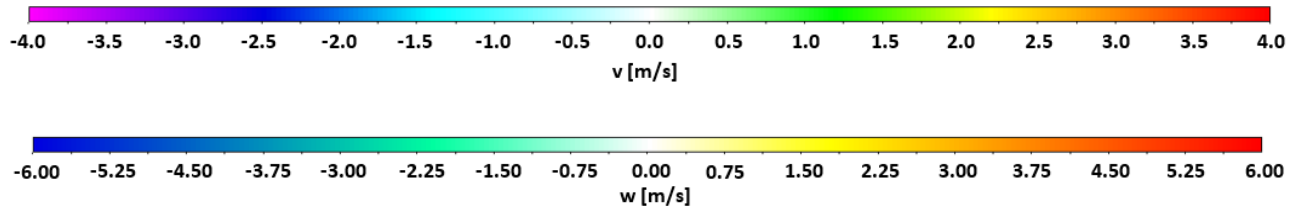

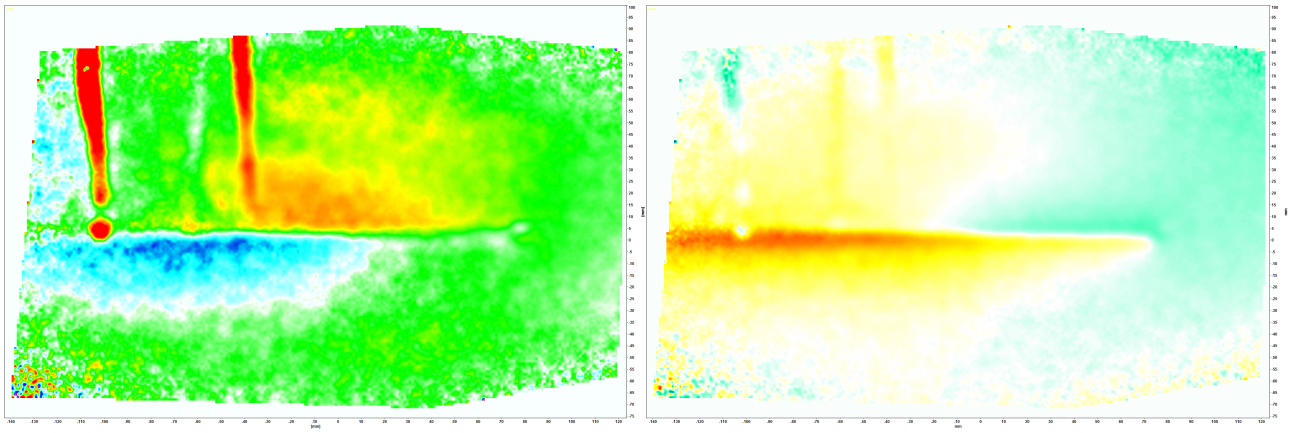

(a) v $[m/s]$ (b) w $[m/s]$

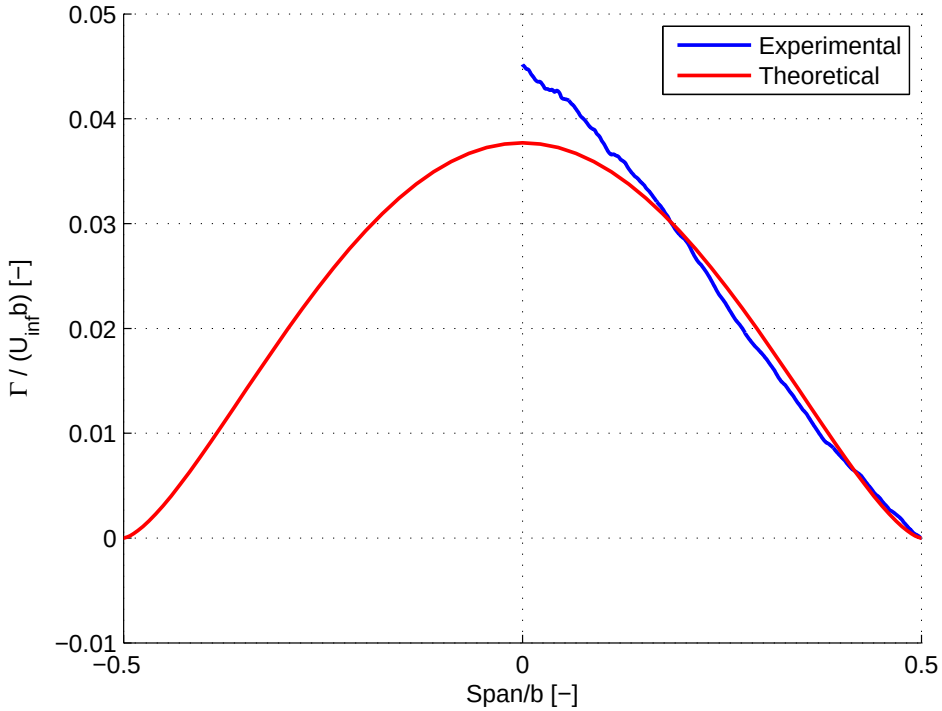

(c) Experimental circulation distribution $\Gamma(y)$ (contour integral method) against theoretical curve (Prandtl's theory).

Figure 3.26: Test at $C_L = 0.4$, $x = 10^{-3}$ behind trailing edge, $Re_r \approx 10^5$

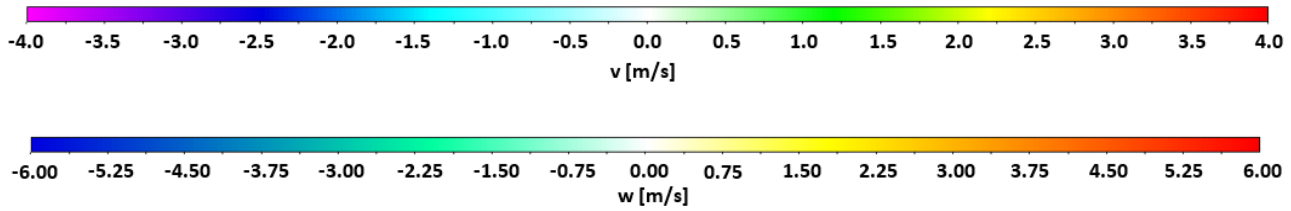

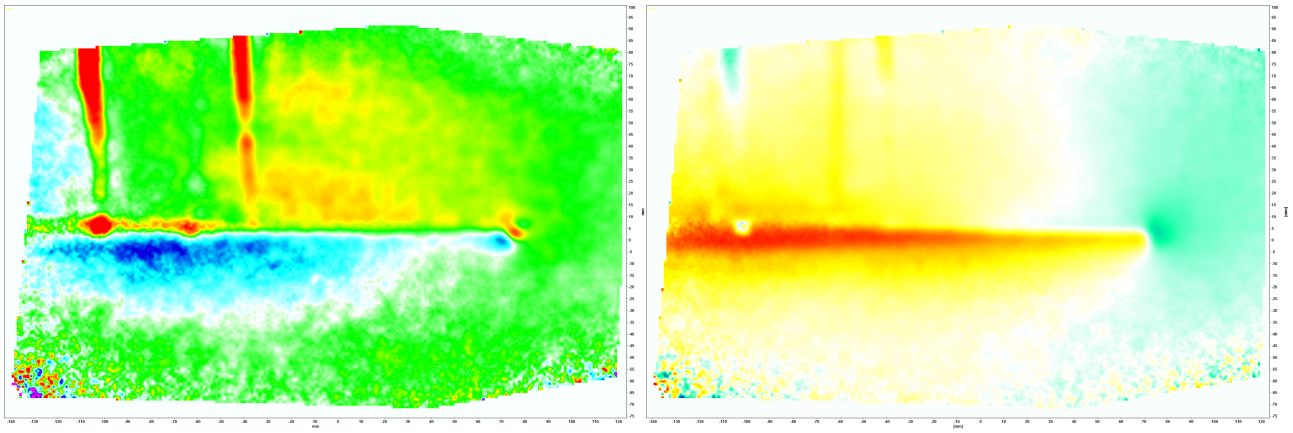

(a) v $[m/s]$ (b) w $[m/s]$

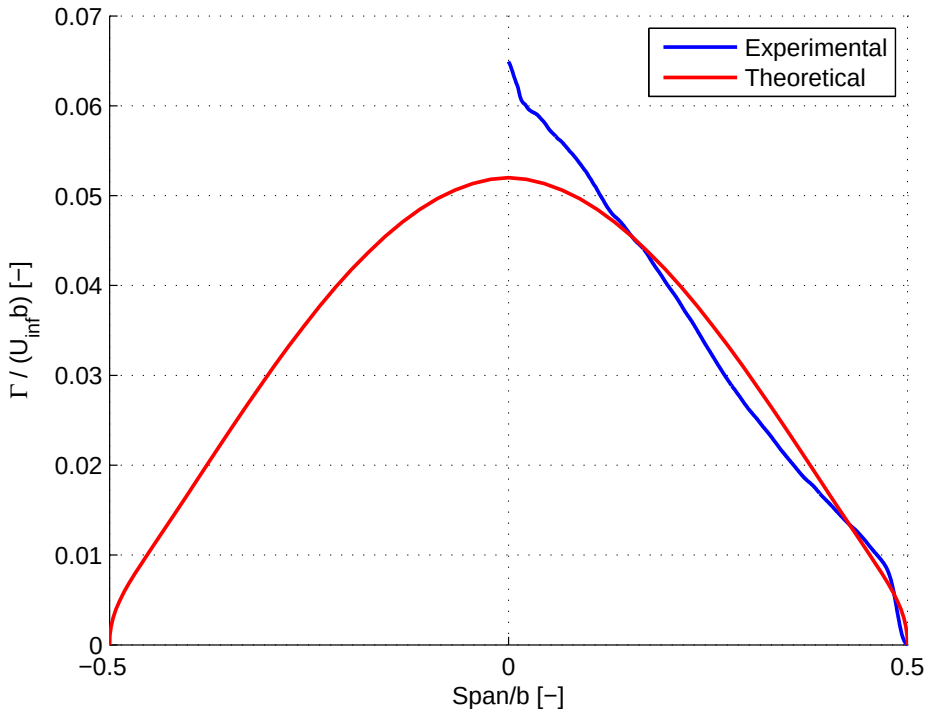

(c) Experimental circulation distribution $\Gamma(y)$ (contour integral method) against theoretical curve (Prandtl's theory).

Figure 3.27: Test at $C_L = 0.6$, $x = 10^{-3}$ behind trailing edge, $Re_r \approx 10^5$

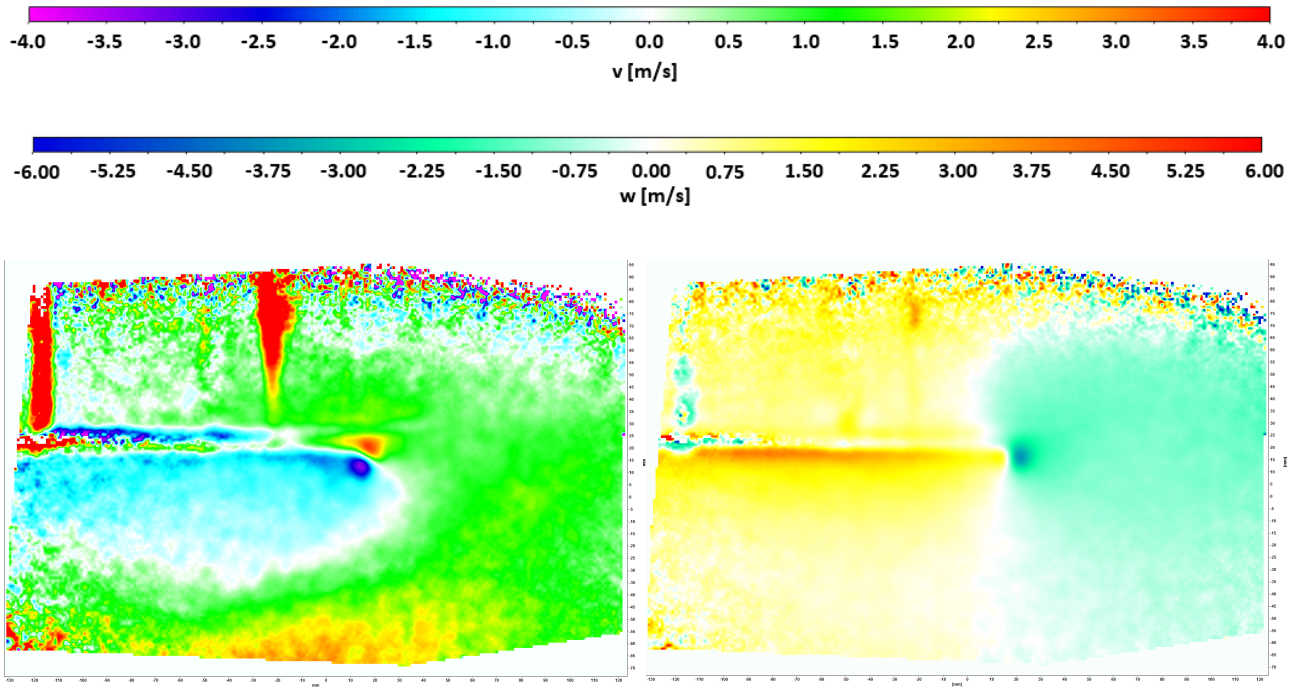

(a) v $[m/s]$ (b) w $[m/s]$

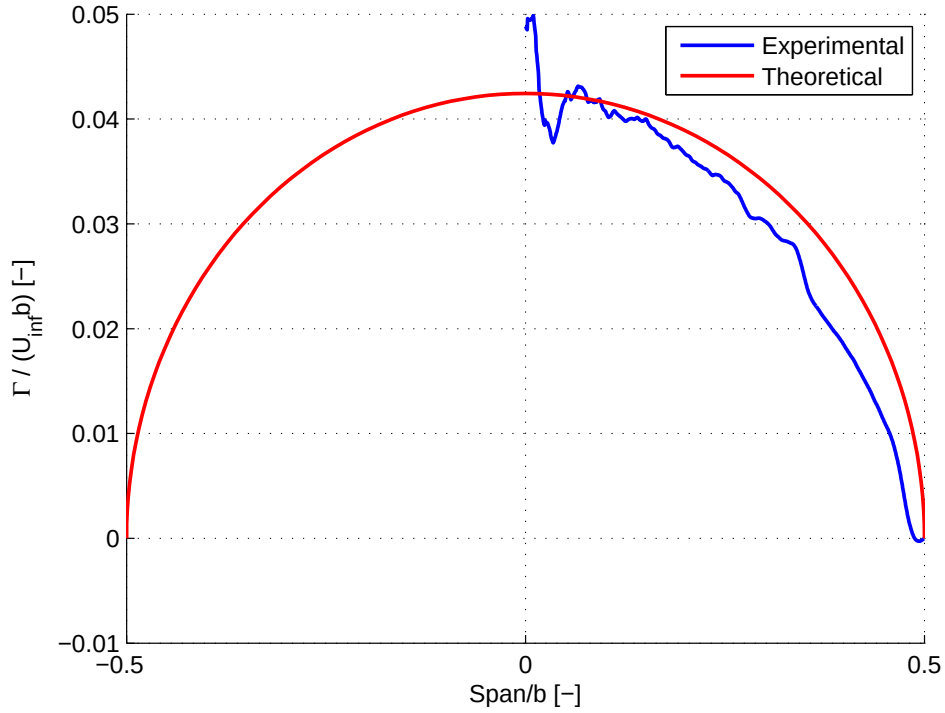

(c) Experimental circulation distribution $\Gamma(y)$ (contour integral method) against theoretical curve (Prandtl's theory).

Figure 3.28: Test at $C_L = 0.4$ with the elliptic wing, $x = 10^{-3}$ behind trailing edge, $Re_r \approx 10^5$

All the preceding graphs are summarized in Figure 3.29.
Again, the results for $C_L = -0.1$ and $C_L = 0.1$ differ slightly from the theory, while the curves for $C_L = 0.4$ and $C_L = 0.6$ tend to follow the theoretical ones, except when approaching the wing's root, where the values for all four cases are too large.

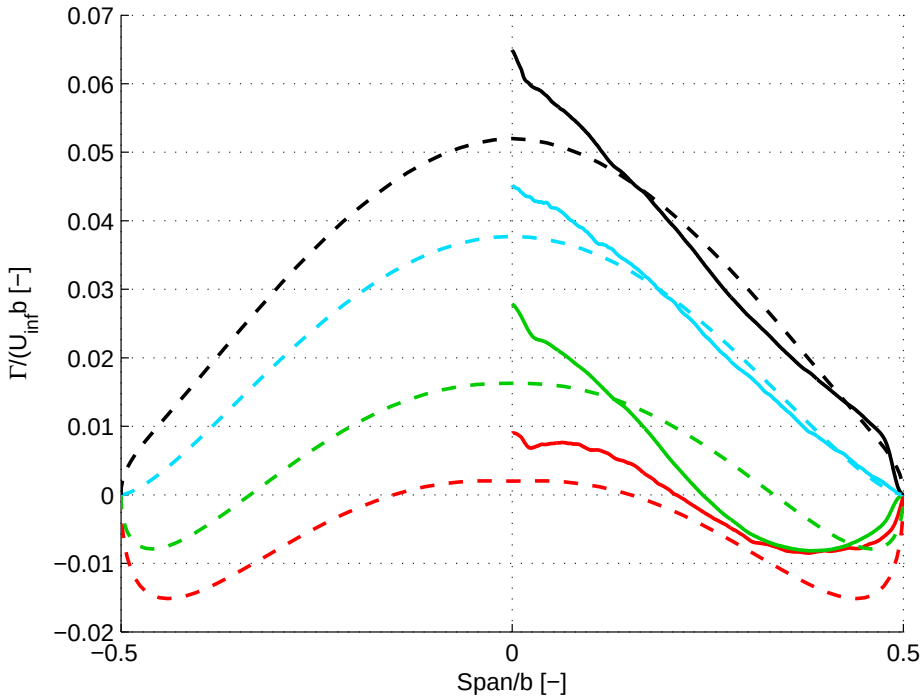

Figure 3.29: Experimental circulation distributions $\Gamma(y)$ (contour integral method)(solid lines) against theoretical curves (dashed lines) for different lift coefficients (red: $C_L = -0.1$, green: $C_L = 0.1$, cyan: $C_L = 0.4$, black: $C_L = 0.6$), $x = 10^{-3}$ $[m]$ from trailing edge, $Re_r \approx 10^5$

Finally, the Fig. 3.30 regroups the curves from the two different integral methods. Although some disparities are visible, both methods are suited for $C_L = 0.4$ and $C_L = 0.6$, while they diverge somewhat for the lowest lift coefficients. Also, the contour method results in much smoother curves than with the surface method. This is mostly due to the fact that the velocities are measured by means of the particles' displacement, and are therefore more precise, as this is a direct measurement. Conversely, the vorticity values are computed based on the measured velocities: any error in those values will directly induce a wrong vorticity result. So, even if some velocity vectors are wrongly calculated near the wing, the contour method will discard them as they are not included in the contour pattern. This is what explains the noisiness of the surface integration curves.
We can therefore conclude that the Prandtl's theory is a robust model, considering its simplicity and the few numerical resolutions needed to compute the theoretical curves.

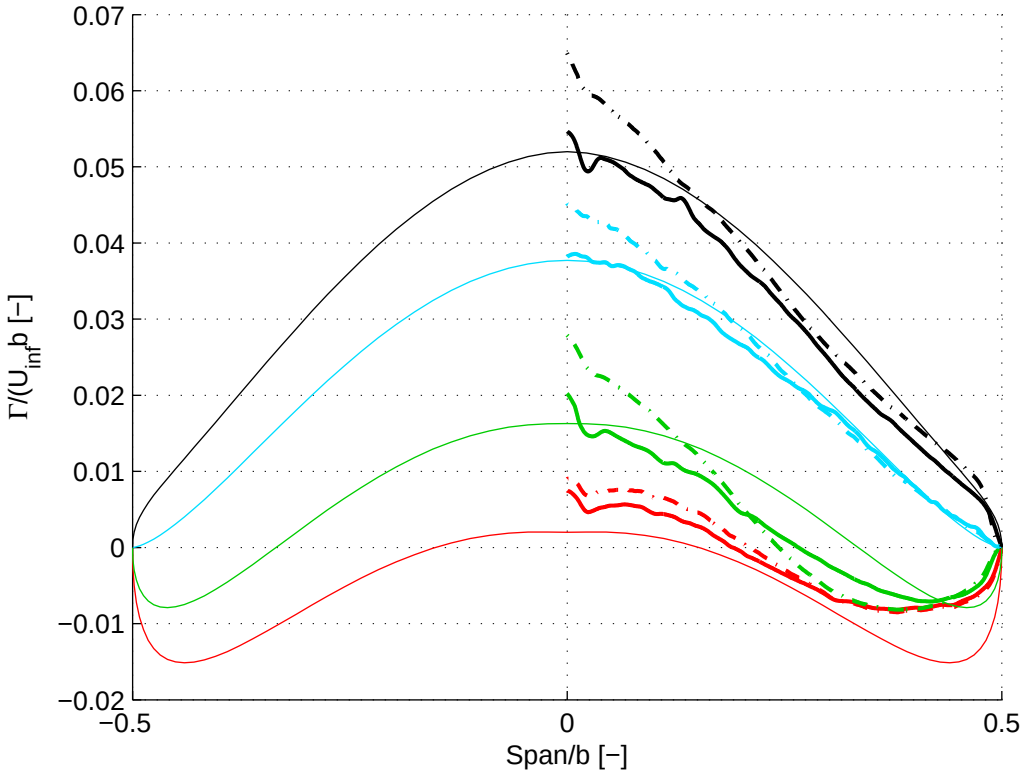

Figure 3.30: Experimental circulation distributions $\Gamma(y)$ curves (bold solid lines : surface integral method, dashed lines : contour integral method) against theoretical curves (thin solid lines) for different lift coefficients (red: $C_L = -0.1$, green: $C_L = 0.1$, cyan: $C_L = 0.4$, black: $C_L = 0.6$), $x = 10^{-3}$ $[m]$ from trailing edge, $Re_r \approx 10^5$

3.2.2 Validation of the drag coefficients

In addition to the 3D velocity and vorticity vectors, the PIV software was able to compute the average kinetic energy (AKE) and the turbulent kinetic energy (TKE) [18] of the flow. As a reminder, one can divide the velocity field in two part : the mean part and the fluctuating part (Eq. 3.14).

$$u = \overline{u} + u' \ . \tag{3.14}$$

The AKE and TKE are then defined as:

$$AKE = \frac{1}{2}\left(\overline{u}^2 + \overline{w}^2 + \overline{w}^2\right) \ , \tag{3.15}$$

$$TKE = \frac{1}{2}\left(\overline{u'^2} + \overline{w'^2} + \overline{w'^2}\right) \ . \tag{3.16}$$

As we know that the generation of lift (and drag) is related to a loss of momentum from the air, we should be able to observe a loss in the air kinetic energy when past the wing.
We therefore conducted three PIV tests at different lift coefficients ($C_L = [0.1, 0.4, 0.6]$) and one with no wing installed. This last test allowed us to determine the AKE of the undisturbed

flow plus the turbulences generated by the wind tunnel, depicted by its TKE.
The total drag of the wing plus its support arms could then be calculated with the following formula: The total drag (wing and support arms) was therefore equal to the loss of AKE from the air plus the creation of TKE by the wing multiplied by the air density:

$$Drag = \rho \int_A ((AKE_{before\ wing} - AKE_{after\ wing}) + (TKE_{after\ wing} - TKE_{before\ wing}))\ dA\ . \tag{3.17}$$

The drag coefficients were then computed with 3.2, taking into account that only half the wingspan was involved during the tests. The C_D values after deduction of the arms' drag coefficient ($C_{D_{arms}} = 0.077$) are compared to the C_D measured by the aerodynamic balance in Table 7:

C_L	$C_{D,polars}$	$C_{D,PIV}$	Error from polars
0.1	0.019	0.012	-36.8%
0.4	0.025	0.026	+4.0%
0.6	0.039	0.044	+12.8%

Table 7: Comparison between drag coefficients values measured by the balance and the PIV equipment

3.2.3 Observation of the wake's vortices

Fig. 3.31 to Fig. 3.34 show the evolution of the wing's wake at various distances behind its trailing edge (those images are more detailed in [17]).
The stage of development of a wing's vortices is characterised by a non-dimensional time τ [19] such that:

$$\tau = \frac{\frac{x}{b} C_L}{4\pi A_R \left(\frac{b_0}{b}\right)^3}\ . \tag{3.18}$$

This allows to compare the vortex pair development at a certain distance x/b behind the trailing edge of different wings. Following again [19], a non-dimensional time $\tau \approx 0.25$ depicts a complete roll-up of the wake's vortices. In our case, this time corresponds to a distance $x \approx 5.3\ [m]$ behind the trailing edge at $C_L = 0.4$. Bearing in mind the wind tunnel's dimensions (2.10 $[m]$ between the convergent part and the air inlet), nothing could be measured at that distance. Consequently, the length between the two vortices b_0 could not be assessed as they were not yet formed. Nevertheless, the very beginning of the roll-up can be observed on the following figures (detailed in [17]).

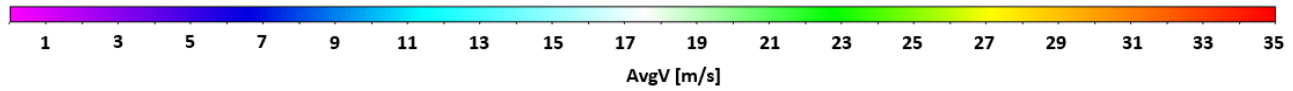

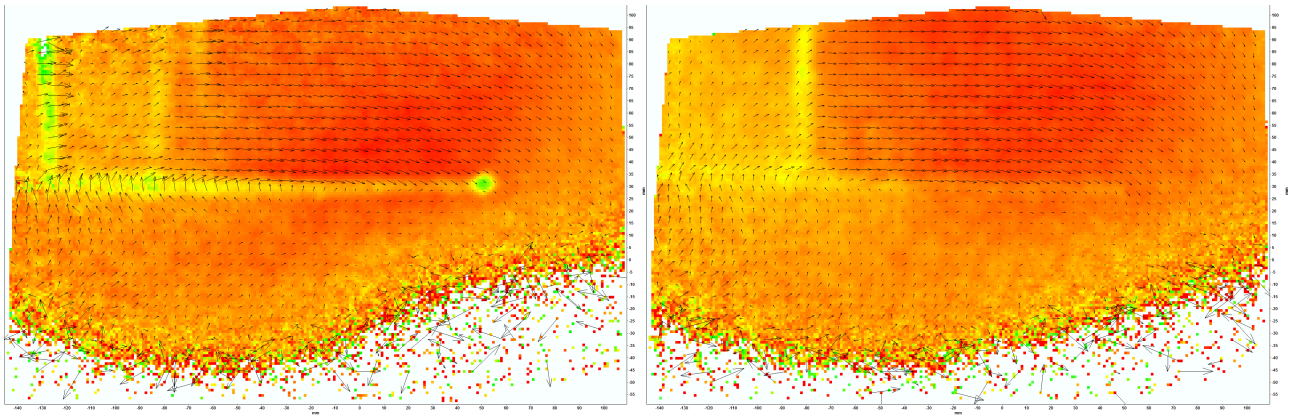

(a) $x = 10^{-3}$ $[m]$ behind trailing edge

(b) $x = 5\ 10^{-2}$ $[m]$ behind trailing edge

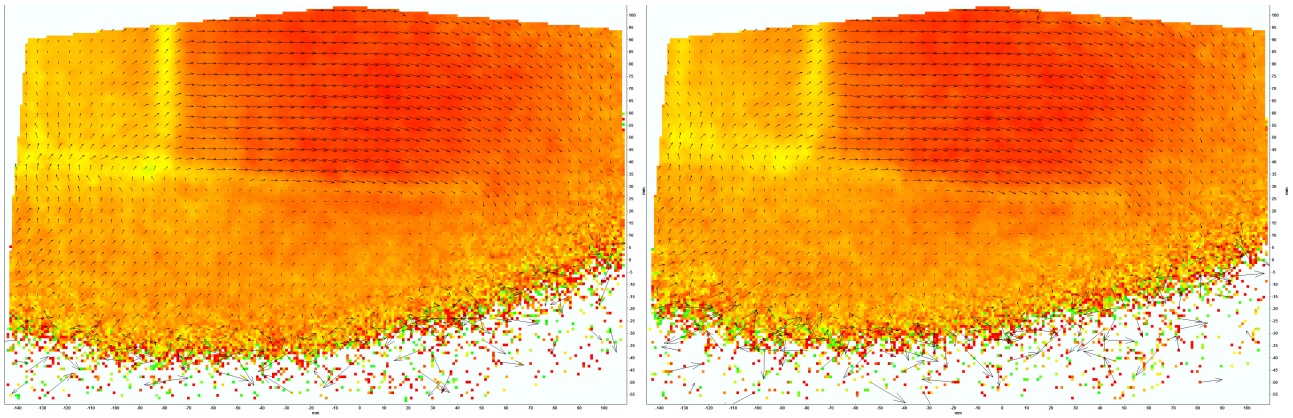

(c) $x = 10^{-1}$ $[m]$ behind trailing edge

(d) $x = 2\ 10^{-1}$ $[m]$ behind trailing edge

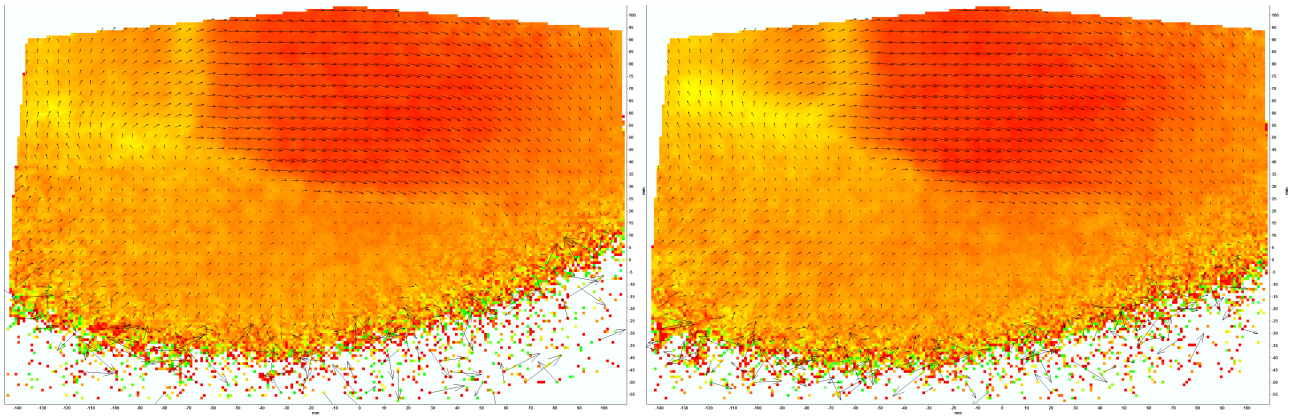

(e) $x = 3.5\ 10^{-1}$ $[m]$ behind trailing edge

(f) $x = 4.5\ 10^{-1}$ $[m]$ behind trailing edge

Figure 3.31: Evolution of the wake's average velocity (*bell wing*) at various distances behind the trailing edge, $C_L = 0.4$, $Re_r \approx 10^5$

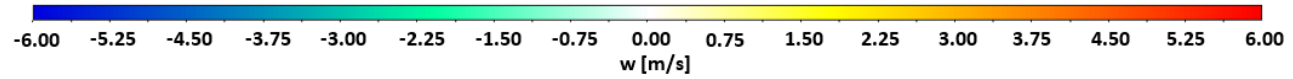

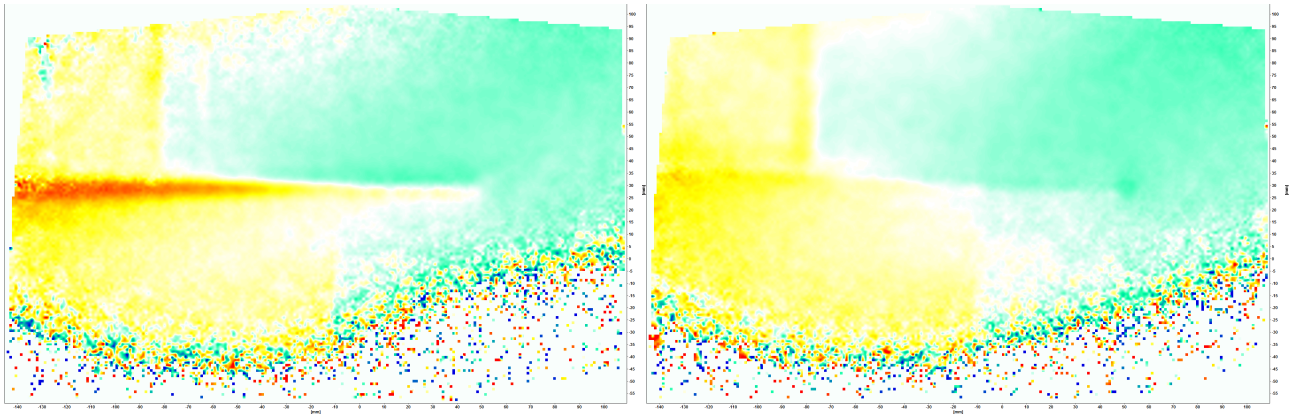

(a) $x = 10^{-3}$ $[m]$ behind trailing edge

(b) $x = 5\ 10^{-2}$ $[m]$ behind trailing edge

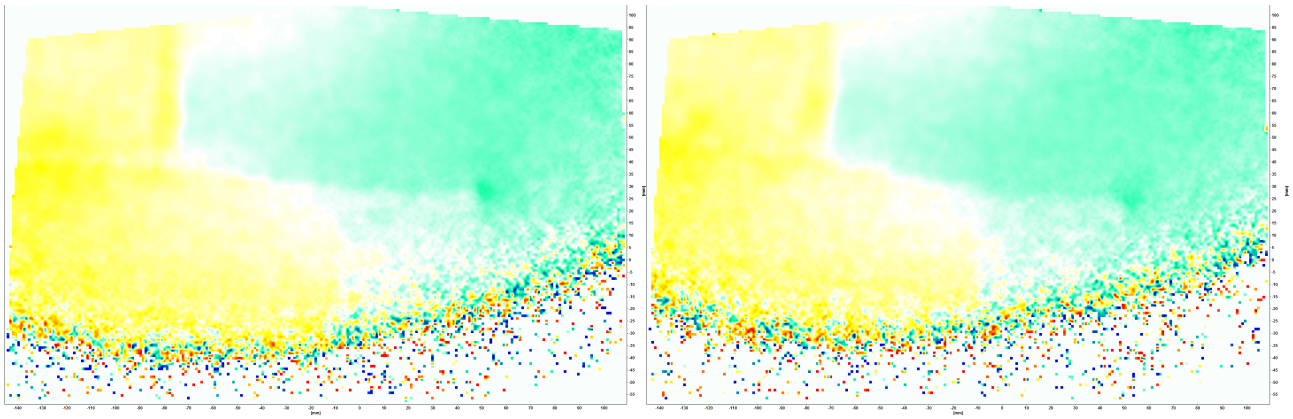

(c) $x = 10^{-1}$ $[m]$ behind trailing edge

(d) $x = 2\ 10^{-1}$ $[m]$ behind trailing edge

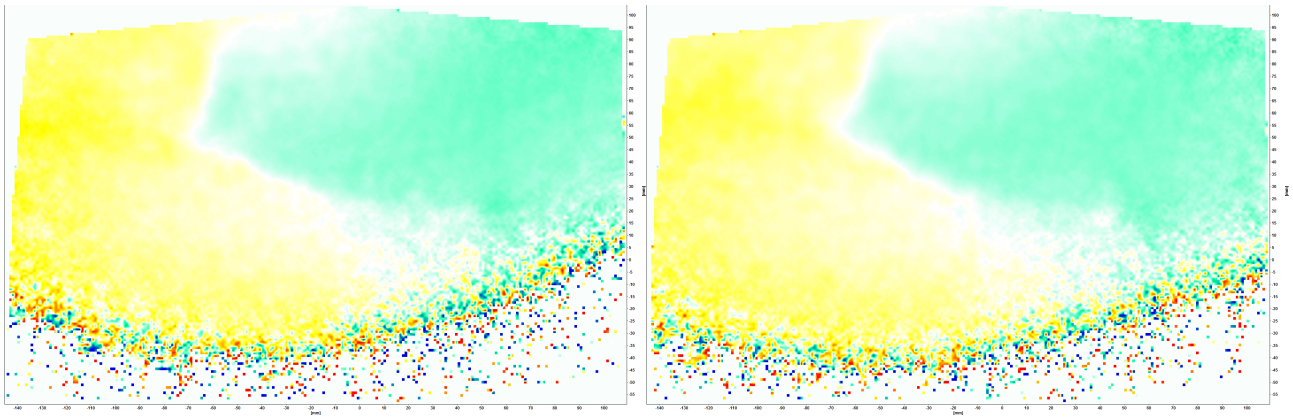

(e) $x = 3.5\ 10^{-1}$ $[m]$ behind trailing edge

(f) $x = 4.5\ 10^{-1}$ $[m]$ behind trailing edge

Figure 3.32: Evolution of the wake's velocity component w (*bell wing*) at various distances behind the trailing edge, $C_L = 0.4$, $Re_r \approx 10^5$

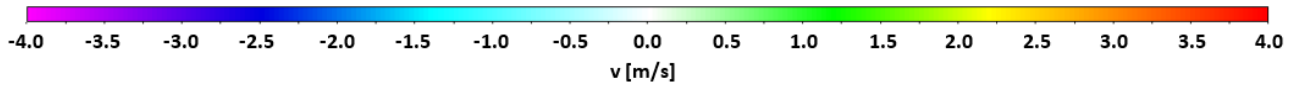

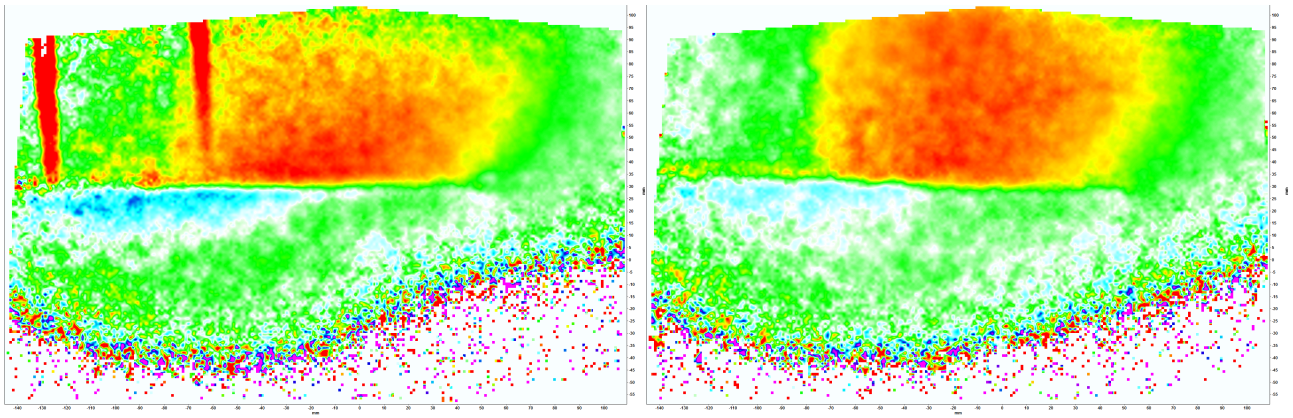

(a) $x = 10^{-3}$ $[m]$ behind trailing edge

(b) $x = 5\ 10^{-2}$ $[m]$ behind trailing edge

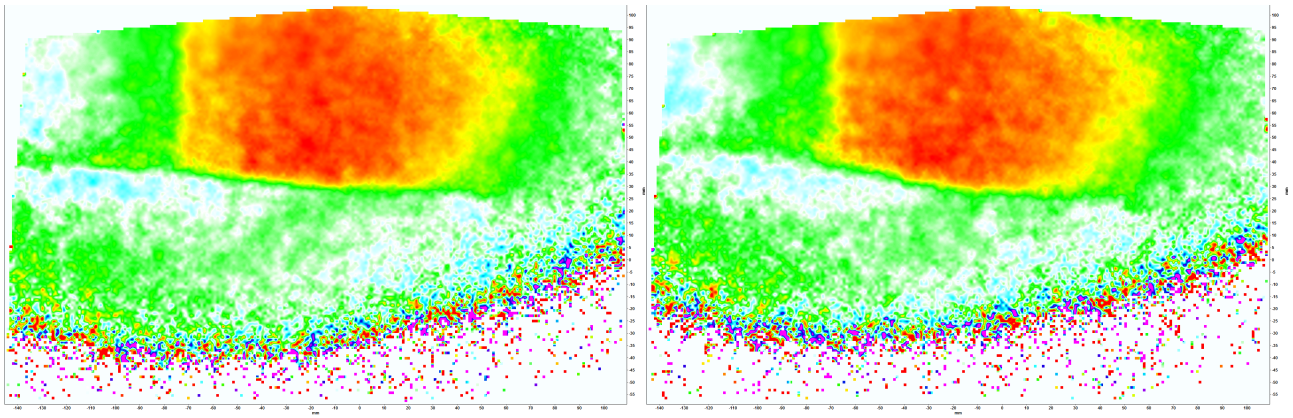

(c) $x = 10^{-1}$ $[m]$ behind trailing edge

(d) $x = 2\ 10^{-1}$ $[m]$ behind trailing edge

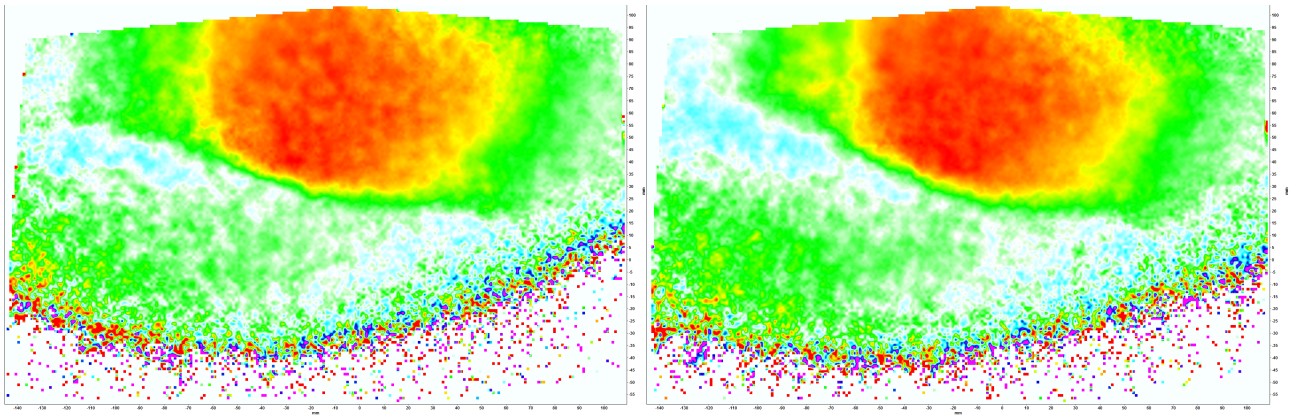

(e) $x = 3.5\ 10^{-1}$ $[m]$ behind trailing edge

(f) $x = 4.5\ 10^{-1}$ $[m]$ behind trailing edge

Figure 3.33: Evolution of the wake's velocity component v (*bell wing*) at various distances behind the trailing edge, $C_L = 0.4$, $Re_r \approx 10^5$

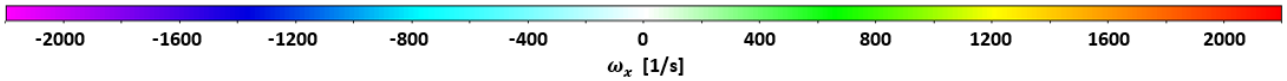

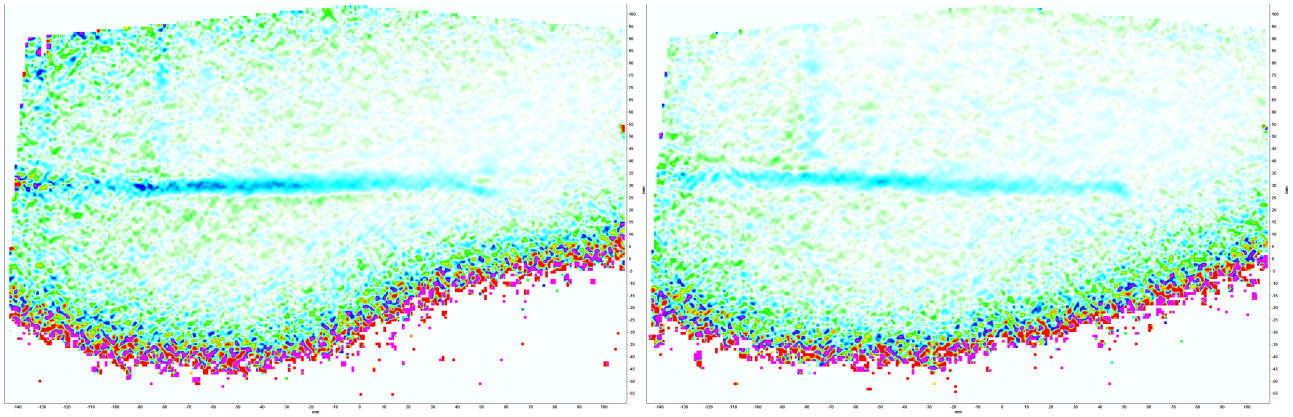

(a) $x = 10^{-3}$ $[m]$ behind trailing edge

(b) $x = 5\ 10^{-2}$ $[m]$ behind trailing edge

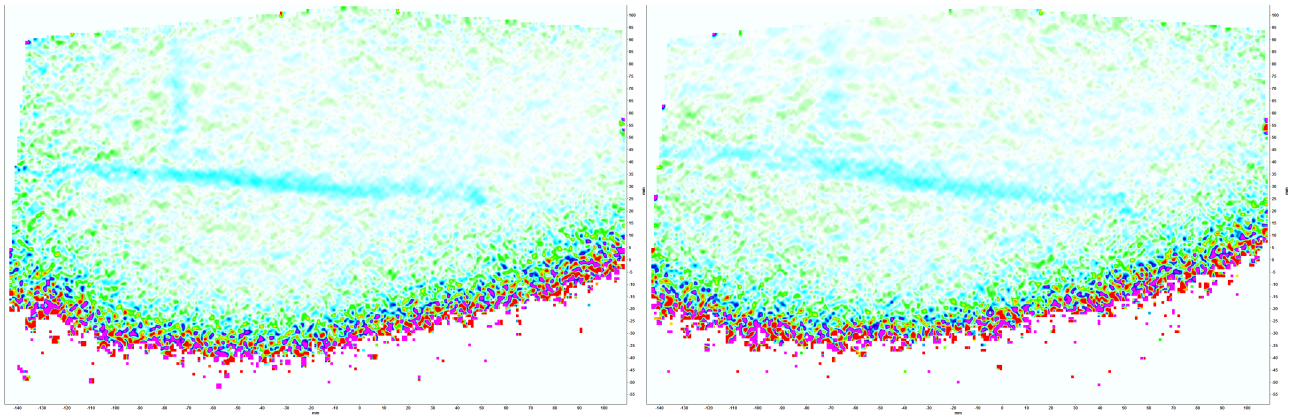

(c) $x = 10^{-1}$ $[m]$ behind trailing edge

(d) $x = 2\ 10^{-1}$ $[m]$ behind trailing edge

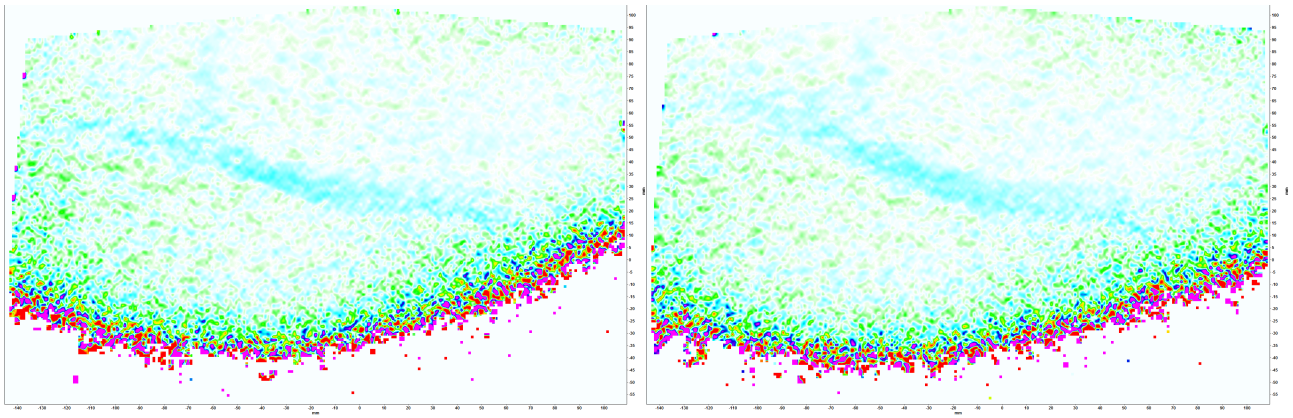

(e) $x = 3.5\ 10^{-1}$ $[m]$ behind trailing edge

(f) $x = 4.5\ 10^{-1}$ $[m]$ behind trailing edge

Figure 3.34: Evolution of the wake's vorticity ω_x (*bell wing*) at various distances behind the trailing edge, $C_L = 0.4$, $Re_r \approx 10^5$

Conclusion

The main goal of this thesis was to investigate the performances of a *bell-shaped* wing designed using the Prandtl's theory [2]. This wing has the particularity that its structural mass is taken into account in its calculation, while the elliptic wing is only characterised by a minimum ratio of lift to drag production.
The Prandtl's theory states that the *bell-shaped* wing, while 22 percent larger than the elliptical one, produces 11 percent less induced drag.

In order to investigate that latter statement, we manufactured our own bell wing. To do so, many parameters had to be determined.
First, its wing area had to equal to the one of the elliptic wing, so that both wings could be compared, but its span had to be 1.225 times larger. Then, a specific chord distribution had to be chosen, as the theoretical one was infinitely sharp at the wingtips, which is obviously impossible to fabricate. This change in geometry required to twist the wing, in order to keep the bell circulation distribution $\Gamma(y)$, which corresponds, we recall, to the case where this wing produces 11 percent less induced drag than the elliptic one. The geometry chosen was a tapered twisted wing, preferred to the rectangular chord distribution, as it offers a better effective angle of attack distribution along the span.
After choosing the right C_L of design and corrected the lift slope of the *NACA0012* profile, the wing was finally ready to be manufactured.

Once the wing created, the experimental campaign could begin.
Firstly, the polars of our wing were investigated. The results were quite encouraging, as low errors were observed between the values given by the lifting line theory and the experiment values, especially for the induced drag coefficient at the C_L of design, where this error was around 4.0%. Unfortunately, the measurements made in 2010 for the elliptic wing were less precise than ours, as they approached 13% of error from the theory for all the parameters of interest. This is partially due to experimental factors (thick supporting arms disturbing the flow, for example), but also to the fact that the aspect ratio of the elliptic wing is $A_R = 6.0$. Unfortunately, the lifting line theory is reliable for A_R values larger than that.
Therefore, the direct comparison between the two wings and the expected 11 percent in induced drag reduction could not be verified. However, the results show clearly that the bell wing is producing less induced drag than the elliptic wing, which is in line with the expectations.
In order to make the comparison between the two wings more reliable, both wings should be manufactured in the same way : same supporting arms (width and length), same connection bits between the wings and their pitch adjusting wires, same spacing between the two arms and so on. This would decrease the uncertainty due to the experimental setup.

Concerning the PIV results, those were more reliable than the ones with the aerodynamic balance. In fact, the circulation distribution $\Gamma(y)$ could be verified by two different methods and the drag coefficients could be confirmed, thanks to the kinetic energy balance of the flow before and after the wing.
Regarding the induced drag coefficients, they could not be verified with the theoretical definition. In fact, it requires the integration of the transversal velocities over an infinitely large region in the wing's near wake. During our experiments, those velocities were affected by tur-

bulence generated by the support arms and the wind tunnel, and were in turn not exploitable. Nevertheless, PIV investigations are rarely performed. Therefore, little help was provided and due to the complexity of the PIV software, we believe that all its potential has not been exploited. A complete and appropriate use of that software would require months of formations, which we could not afford as the experimental campaign was made in only one semester.
To conclude, in addition to the experimental factors that could have influenced our results (type of seeding, laser sheet non uniform, ...), the analysed cross section of the flow turned out to be too large considering the cameras' resolution and the particles' size. Investigations over smaller regions behind the wing should have been considered in order to obtain more precise results. However, despite those inaccuracies, we can be quite confident in our results as they approach relatively well the theory.

References

[1] L. Prandtl. *Theory of lifting surfaces*. Technical notes for the National Advisory Comittee for Aerodynamics, 1920.

[2] L. Prandtl. *Uber Tragflugel kleinsten induzierten Widerstandes*. Zeitschrift fur Flugtechnik und Motorluftschiffahrt, 1933.

[3] Albion H. Bowers, and Oscar J. Murillo *On Wings of the Minimum Induced Drag: Spanload Implications for Aircraft and Birds*. NASA, Armstrong Flight Research Center, Edwards, California, 2016.

[4] G. Winckelmans, P. Chatelain. *Aerodynamics of external flow, class notes MECA2323, G. Winckelmans part*. EPL-UCL, 2016.

[5] John D. Anderson, Jr. *Fundamentals of aerodynamics, fifth edition*. University of Maryland, 2011.

[6] G.K. Batchelor. *An introduction to fluid dynamics, 8th edition*. University of Cambridge, 2011.

[7] J. Jansen, A. Wiertz. *Investigation experimentale d'ailes avec differentes distributions de corde, TFE*. EPL-UCL, 2010.

[8] E. S. Souca, C. Ciupan *Airfoil selection for aerodynamic performance criterion on small wind turbines*. Technical University of CLUJ-NAPOCA, 2014.

[9] *Polaire et centre aerodynamique d'une aile, Laboratory notes*. UCL

[10] *La balance aerodynamique, Technical notes*. UCL

[11] J. McArthur. *Aerodynamics of wings at low Reynolds numbers*. University of Southern California, 2007.

[12] Dong-Ha Kim, Jo-Won Chang, Joon Chung. *Low-Reynolds-Number Effect on Aerodynamic Characteristics of a NACA 0012 Airfoil*. Korea Aerospace Research Institute, Korea Aerospace University, Ryerson University, 2011.

[13] E. N. Jacobs, A. Sherman. *Airfoil section characteristics as affected by variations of the Reynolds number, Report No. 586*. National Advisory Committee for aeronautics.

[14] P. Chatelain. *Aerospace dynamics, class notes MECA2830*. EPL-UCL, 2016.

[15] *Flow Master, PIV software manual*. LaVision, France.

[16] G. Winckelmans, J.-F. Remacle. *Mecanique des fluides et Transferts II, G. Winckelmans part*. EPL-UCL, 2015.

[17] J. Toussaint. *Design and experimental investigation with particle image velocimetry of a minimum induced drag wing*. Masters' thesis, Appendix : Images of PIV experiments. Location

[18] Frank M. White. *Viscous Fluid Flow, third edition*. University of Rhode Island, 2011.

[19] C. Cottin, G. Winckelmans, T. Lonfils and R. Cocle. *Roll-up of a temporally-evolving wing wake with velocity deficit*, research report TR-2.2.2-3 of FAR-Wake project. UCL, 2005.

Appendix A B_n coefficients resolution, without twist

For a wing without twist, $B_n = \alpha b_n$. The compatibility equation is then:

$$\sum_n b_n sin(n\theta) = \frac{1}{2} a_0 \frac{c(\theta)}{b} \left[1 - \frac{1}{2} \sum_n n \; b_n \frac{sin(n\theta)}{sin(\theta)} \right] \tag{A.1}$$

$$\leftrightarrow \sum_n b_n \left[sin(n\theta) + \frac{1}{4} a_0 \frac{c(\theta)}{b} n \frac{sin(n\theta)}{sin(\theta)} \right] = \frac{1}{2} a_0 \frac{c(\theta)}{b} \tag{A.2}$$

$$\leftrightarrow \sum_n b_n q_n(\theta) = r(\theta) \tag{A.3}$$

We fix N the number of b_n coefficients to compute, and minimise the error H of A.3 in the least squares sense :

$$H = \int_0^\pi \left(\sum_n b_n q_n(\theta) - r(\theta) \right)^2 d\theta \tag{A.4}$$

$$\frac{\partial H}{\partial b_m} = 2 \int_0^\pi \left(\sum_n b_n q_n(\theta) - r(\theta) \right) q_m(\theta) \, d\theta \tag{A.5}$$

$$= 0 \tag{A.6}$$

$$\leftrightarrow \sum_n \left(\int_0^\pi q_m(\theta) q_n(\theta) \, d\theta \right) b_n = \int_0^\pi q_m(\theta) r(\theta) d\theta \tag{A.7}$$

$$\leftrightarrow A_{mn} b_n = C_m \tag{A.8}$$

This linear system is to solve to obtain the best values for the b_n coefficients.

Appendix B B_n coefficients resolution, with twist

For a wing with twist, $B_n = b_n\alpha + d_n$. The compatibility equation is then:

$$\sum_n B_n sin(n\theta) = \frac{1}{2}a_0\frac{c(\theta)}{b}\left[(\alpha + \alpha_v(\theta)) - \frac{1}{2}\sum_n nB_n\frac{sin(n\theta)}{sin(\theta)}\right] \tag{B.1}$$

$$\leftrightarrow \sum_n B_n\left[sin(n\theta) + \frac{1}{4}a_0\frac{c(\theta)}{b}n\frac{sin(n\theta)}{sin(\theta)}\right] = \frac{1}{2}a_0\frac{c(\theta)}{b}(\alpha + \alpha_v(\theta)) \tag{B.2}$$

$$\leftrightarrow \sum_n B_n q_n(\theta) = r(\theta)(\alpha + \alpha_v(\theta)) \tag{B.3}$$

$$\leftrightarrow \sum_n (b_n\alpha + d_n)q_n(\theta) = r(\theta)(\alpha + \alpha_v(\theta)) \tag{B.4}$$

Two separate linear problems have then to be solved, following the same procedure as in Appendix A :

$$\sum_n b_n q_n(\theta) = r(\theta) \tag{B.5}$$

$$\sum_n d_n q_n(\theta) = r(\theta)\alpha_v(\theta) \tag{B.6}$$

With b_n in B.5 the same that for the wing without twist.

Appendix C Cameras data sheet

LaVision
FOCUS ON IMAGING

Imager *pro X* 2M

Imager *pro X* 2M is a high sensitivity, high resolution digital camera used in the LaVision **FlowMaster** PIV system. The camera is equipped with an interline transfer chip with progressive scan readout and up to 4 GB memory in the camera head to store more images faster than any interface to a PC can currently handle. The min. interframe time of 110 ns makes this camera ideal for high velocity PIV measurements.

General System Specifications

Double shutter	two images with 110 ns min. interframing time
Digital output	14 bit
Cooling	Peltier to +10 °C
Interface	CameraLink
Lens mount	F-mount, (optional c-mount)
Number of pixels	1600 x 1200 pixels (extended mode 1648x1214)
Pixel size	7.4 x 7.4 µm²
Sensor format	12.2 x 9.0 mm²
Spectral range	290 – 1100 nm
Max. QE	typ. 55 % @ 500 nm
Full well capacity	40,000 e-
Blooming suppression	> 300 x
Readout (scan) rate	40 MHz
Frame rate	29 frames/s
Binning	horizontal 1, 2 ; vertical 1, 2, 4, 8
Partial scan	frame rate higher at reduced region of interest
Operating temp.	5 – 40 °C
Size of camera head	84 x 66 x 175 mm³

optional: DaVis Software / PC / timing unit

Operation system	Windows 7 (64 bit)
Data acquisition	user programmable
Command language	‚C' syntax for system and user functions
Device control	laser, stepping motor, Autofocus, Scheimpflug

Ordering information

Part number	Description
1101360	Imager pro X 2M camera with 1 GB memory, CamLink
1101320	Imager pro X 2M camera with 2 GB memory, CamLink
1101380	Imager pro X 2M camera with 4 GB memory, CamLink
1108217	CamLink framegrabber for Imager pro X cameras

Oct-13

LaVisionUK Ltd
2 Minton Place / Victoria Road
Bicester, Oxon / OX26 6QB / United Kingdom
E-Mail: sales@lavision.com / www.lavisionuk.com
Phone: +44-(0)-870-997-6532 / Fax: +44-(0)-870-762-6252

LaVision GmbH
Anna-Vandenhoeck-Ring 19
D-37081 Göttingen / Germany
E-Mail: info@lavision.com / www.lavision.com
Tel. +49-(0)551-9004-0 / Fax +49-(0)551-9004-100

LaVision Inc.
211 W. Michigan Ave. / Suite 100
Ypsilanti, MI 48197 / USA
E-mail: sales@lavisioninc.com / www.lavisioninc.com
Phone: (734) 485 - 0913 / Fax: (240) 465 - 4306

Appendix D 3D Side documentation

Our wing has been manufactured by *3D Side*, a company based in Louvain-la-Neuve. The data sheets of the operated machine and the used material are listed below.

Plastic laser sintering system **FORMIGA P 110**
for the direct manufacture of series,
spare parts and functional prototypes

e-Manufacturing Solutions

The Technology:
Laser Sintering - the Key to e-Manufacturing

Laser sintering is well known as the technology of choice for ensuring the quickest route from product idea to market launch. Innovative companies from a broad range of industries are using this technology for e-Manufacturing — the fast, flexible and cost-effective production directly from electronic data for every phase of the product life cycle.

The system: e-Manufacturing in the compact class

"FORMIGA quality" has become a quality label for the additive manufacturing of plastics. The FORMIGA P 110 is the successor to the FORMIGA P 100 and continues to be the laser sintering system of choice in the compact class that gives you an ideal access to the world of laser sintering.

With a build envelope of 7.9 in x 9.8 in x 13 in, the FORMIGA P 110 produces plastic products from polyamide or polystyrene within a few hours directly from CAD data. The system is ideal for the economic production of small series and individualized products with complex geometries — requirements that apply e.g. to the medical device industry and to high-value consumer goods. Various EOS parameter sets enable a focus both on economic efficiency and on highest surface quality. With shortest throughput times and relatively low investment costs, the FORMIGA P 110 can be integrated perfectly into a production environment that requires highest levels of flexibility.

Innovation for use in production

The FORMIGA P 110 offers a number of technical innovations. Process stability and reproducibility of the system have been enhanced even further. Among other things, this is achieved by the new integrated 4-channel heating and a single-point pyrometer. An external nitrogen connection guarantees least-cost integration in factories that have a central nitrogen supply system. High product quality is ensured by the proved and tested dosing and coating system. The FORMIGA P 110 achieves maximal surface quality

Filling funnel: Made of polyamide using an EOSINT P system.

in particular at vertical walls. The extremely small focus diameter enables the production of walls that are only 0.016 in thick, making the system ideal for small, filigree components such as connectors. The FORMIGA P 110 is extremely user-friendly and requires just a minimum of accessories. This results in lower energy consumption and consequently in reduced costs of operation. It is a door-passing laser sintering system with low erection condition requirements. The system can be installed and set up in less than two days. Data preparation can conveniently take place at the workstation with makes it well suited also for decentralized production areas.

Automation and intelligent functionality

Its ergonomic peripheral equipment and the high degree of automation make the FORMIGA P 110 easy to handle, enable optimal use of machine capacity and materials and allow best possible integration of the system into industrial production environments. The newly developed Integrated Process Chain Management (IPCM+) solution features a powder mixing station and integrated powder recycling tailored to production requirements. The high level of automation makes for minimal downtimes and increased productivity. Moreover, the EOSPACE software allows the parts to be easily positioned in the build chamber to make optimal use of the available space. This means shorter production times and lower costs.

Technical Data	
Effective building volume	200 mm x 250 mm x 330 mm (7.9 x 9.8 x 13 in, excl. pyrometer measurement spot)
Building speed (depending on material)	up to 20 mm height/h (0.79 in/h)
Layer thickness (depending on material)	0.06 mm (0.0024 in), 0.1 mm (0.0039 in), 0.12 mm (0.0047 in)
Support structure	not required
Laser type	CO_2, 30 W
Precision optics	F-theta lens
Scan speed during building	up to 5 m/sec (16.4 ft/sec.)
Power supply	16 A
Power consumption	maximum 5 kW / typical 1,4 kW
Nitrogen generator incl. external nitrogen connection	integrated
Compressed air supply	min. 6,000 hPA (87 psi); 10 m3/h (13.08 m^3)
Dimensions (W x D x H)	
Machine with powder containers and touch screen	1,320 mm x 1,067 mm x 2,204 mm (51.97 x 42.01 x 86.77 in)
Recommended installation space	3.20 m x 3.50 m x 3.0 m (126 x 137.8 x 118.1 in)
Weight	approx. 600 kg (1,323 lb.)
Unpacking and sieving station (optional)	1,200 mm x 700 mm x 1,500 mm (47.24 x 27.56 x 59.06 in)
Powder mixing station (optional)	700 mm x 500 mm x 1,000 mm (27.56 x 19.69 x 39.37 in)
Data preparation	
Software	EOS RP Tools (optional); Desktop PSW
Data interface to CAD system	STL (optional: converter to all common formats)
Network	Ethernet

e-Manufacturing Solutions

PA 2200 Balance 1.0

PA12 EOS GmbH - Electro Optical Systems

Product Texts

Product Texts

This whitish fine powder PA 2200 on the basis of polyamide 12 serves with its very well-balanced property profile a wide variety of applications. Laser-sintered parts made from PA 2200 possess excellent material properties:

- high strength and stiffness
- good chemical resistance
- excellent long-term constant behaviour
- high selectivity and detail resolution
- various finishing possibilities (e.g. metallisation, stove enamelling, vibratory grinding, tub colouring, bonding, powder coating, flocking)
- bio compatible according to EN ISO 10993-1 and USP/level VI/121 °C
- approved for food contact in compliance with the EU Plastics Directive 2002/72/EC (exception: high alcoholic foodstuff)

Typical applications of the material are fully functional plastic parts of highest quality. Due to the excellent mechanical properties the material is often used to substitute typical injection moulding plastics. The biocompatibility allows its use e.g. for prostheses, the high abrasion resistance allows e.g. the realisation of movable part connections.

120 µm layer thickness
The advantage of the Balance parameter set is equilibrium. The layer thickness of 120 µm offers a perfect balance between production costs, mechanical properties, surface quality and accuracy. It is therefore suitable for parts with varying geometries, dimensions and requirements.

Mechanical properties	Value	Unit	Test Standard
Izod Impact notched (23°C)	**4.4**	kJ/m²	ISO 180/1A
Shore D hardness (15s)	**75**	-	ISO 7619-1

3D Data	Value	Unit	Test Standard
The properties of parts manufactured using additive manufacturing technology (e.g. laser sintering, stereolithography, Fused Deposition Modelling, 3D printing) are, due to their layer-by-layer production, to some extent direction dependent. This has to be considered when designing the part and defining the build orientation.			
Tensile Modulus			ISO 527-1/-2
X Direction	**1650**	MPa	
Y Direction	**1650**	MPa	
Z Direction	**1650**	MPa	
Tensile Strength			ISO 527-1/-2
X Direction	**48**	MPa	
Y Direction	**48**	MPa	
Z Direction	**42**	MPa	
Strain at break			ISO 527-1/-2
X Direction	**18**	%	
Y Direction	**18**	%	
Z Direction	**4**	%	
Charpy impact strength (+23°C, X Direction)	**53**	kJ/m²	ISO 179/1eU
Charpy notched impact strength (+23°C, X Direction)	**4.8**	kJ/m²	ISO 179/1eA
Flexural Modulus (23°C, X Direction)	**1500**	MPa	ISO 178

Thermal properties	Value	Unit	Test Standard
Melting temperature (20°C/min)	**176**	°C	ISO 11357-1/-3
Vicat softening temperature (50°C/h 50N)	**163**	°C	ISO 306
Burning behavior			UL 94
Test passed, HB	**0.5**	mm	
Test passed, HB	**1.6**	mm	
Test passed, HB	**3.2**	mm	

Other properties	Value	Unit	Test Standard
Density (lasersintered)	**930**	kg/m³	EOS Method
Powder colour (ac. to safety data sheet)	**White**	-	-

Characteristics

Processing
Laser Sintering, Rapid Prototyping

Chemical Resistance
General Chemical Resistance

Certifications
FDA approval acc. to USP Biological test (classification VI/121°C)

Rue Archimède, 1 bte L6.11.01, 1348 Louvain-la-Neuve **www.uclouvain.be/epl**